

Charged Particle Asymmetry in pp, pPb and PbPb Collision Systems at  
 $\sqrt{s_{NN}} = 5.02$  TeV.

By

Ravi Janjam

Dissertation

Submitted to the Faculty of the  
Graduate School of Vanderbilt University  
in partial fulfillment of the requirements  
for the degree of

DOCTOR OF PHILOSOPHY

in

Physics

September 30, 2018

Nashville, Tennessee

Approved:

Prof. Victoria Greene.

Prof. Shane Hutson.

Prof. Paul Sheldon.

Prof. Thomas Weiler.

Prof. Robert Weller.

Dedicated to the experimental physicists, whose probes explore natural phenomena unveiling the *deceptive application* or rather *violation* of rules within a rigid framework while simultaneously pushing the limits of technology; to the theoretical physicist, who explores the abstract rules of nature, and to the engineers, for building the system and handling the complexity of the system. Hopefully, this cycle will be in a state of perpetual non-equilibrium bringing in novelty to the realm of science and technology.

## ACKNOWLEDGMENTS

First and foremost, I would like to thank my advisor Prof. Charles Maguire, who has supervised my projects since the beginning of my graduate studies; his comments and suggestions helped me accelerate my understanding of the subject. I am also grateful to Prof. Victoria Greene, for her help and support and for being my advisor.

Thanks to Prof. Julia Velkovska, for suggesting me this project. This project helped me learn a lot about Pythia. I wouldn't have learnt about all the fine details if it was not for this project.

My research work at Vanderbilt started with assisting Dr. Monika Sharma's  $\pi^0$  analysis. The assignments I got from her and the challenges my advisor posed, helped me gain a good grasp of the subject. This work was largely built upon Dr. Eric Appelt's charged particle analysis and I couldn't have gotten started without the code base he built over the years. It would be unjustified if I didn't mention Dr. Austin Baty's and Dr. Krizstian Krajczar's help in this project. The informal conversations I had with Krizstian at CERN, gave a good grasp of the project and also many thanks to Austin as well, for sharing the data points to match with my simulations. My special thanks are also due to Dr. Alfredo Gurrolla making some really important suggestions, without which the data generated in Pythia simulations would have become unmanageable.

Many thanks to Dr. Andy Buckley, LHAPDF expert; for his timely help in generating nuclear PDFs for Pb nucleus.

I have benefited a lot from Dr. Andrew Melo's suggestions; during code development and any issue with job submission. I have also enjoyed discussions with Dr.

Alan Tackett, Dr. William French, Kevin Butterbaugh, and Matt during ACCRE meetings. Some of the challenges that emerged out of the routine problems gave me a great perspective on the complexity of the system and develop ideas to overcome them. Without ACCRE facility or the admin experts, my work would have taken a very long time to finish, cheers to the experts !

My special thanks are also due to the rest of my thesis committee, Prof. Paul Sheldon, Prof. Thomas Weiler, Prof. Shane Hutson and to Prof. Robert Weller, whose suggestions and more importantly the questions posed gave a fresh perspective on the problem at hand.

And finally my thanks are due to the CMS Heavy Ion colleagues, Dr. Monika Sharma, Dr. Ben Snook, Dr. Eric Appelt, Dr. Sourav Tarafdar, Dr. Shengquan Tuo, Dr. Qiao Xu, Dr. Hong Ni, and Weizhuang Peng.

# TABLE OF CONTENTS

	Page
DEDICATION . . . . .	ii
ACKNOWLEDGMENTS . . . . .	iii
LIST OF FIGURES . . . . .	viii
1 Quantum Chromodynamics and Quark Gluon Plasma . . . . .	1
1.1 Introduction . . . . .	1
1.2 Quantum Chromodynamics (QCD) . . . . .	2
1.2.1 Gell-Mann’s Hypothesis . . . . .	2
1.2.2 Asymptotic Freedom . . . . .	3
1.3 Quark Gluon Plasma (QGP) . . . . .	6
1.3.1 Jet Quenching . . . . .	8
1.4 Phase Space Diagram . . . . .	9
1.4.1 Different Phases of QGP formation . . . . .	11
1.4.2 Hot Nuclear Medium and Cold Nuclear Medium . . . . .	12
1.5 Centrality of a Heavy Ion Collision . . . . .	16
1.6 Glauber Model . . . . .	18
1.7 Motivation and Objective of this Thesis . . . . .	18
1.8 Summary . . . . .	21
2 Experiment . . . . .	22
2.1 CMS Detector at LHC . . . . .	22
2.1.1 Superconducting Magnet . . . . .	22
2.1.2 Electromagnetic Calorimeter (ECAL) . . . . .	23
2.1.3 Hadron Calorimeter(HCAL) . . . . .	25
2.1.4 The Muon System . . . . .	26

2.1.5	Forward Detectors . . . . .	26
2.1.6	Tracking Subsystem . . . . .	27
2.1.6.1	Track Reconstruction . . . . .	28
2.1.6.2	Vertex Reconstruction . . . . .	29
2.2	CMS Computing Model . . . . .	30
2.3	CMS Module Framework . . . . .	31
2.4	Data Formats : RAW, RECO and AOD . . . . .	32
2.5	CMS Data Acquisition Workflows . . . . .	33
2.6	Event Display . . . . .	36
2.7	Summary . . . . .	37
3	Measurement of Nuclear Modification Factor $R_{pPb}$ . . . . .	38
3.1	Method and Data Sets . . . . .	39
3.1.1	Spectra of All Charged Particles: 2013 pPb and 2015 pp data sets . . . . .	39
3.1.1.1	Combination of Spectra from different Data Sets . . . . .	41
3.2	Data Driven Analysis: Positive and Negative Charged Particles . . . . .	44
3.3	Summary . . . . .	45
4	Monte Carlo Simulations . . . . .	46
4.1	Event Generator: Pythia . . . . .	47
4.2	Hard Scattering Processes . . . . .	57
4.2.1	Tune Parameters . . . . .	57
4.2.2	Pythia 6 vs Pythia 8 . . . . .	60
4.3	Parton Distribution Functions (PDF) . . . . .	60
4.3.1	Experimental Measurement of PDFs . . . . .	61
4.3.2	Deep Inelastic Scattering (DIS) . . . . .	61
4.3.3	Drell-Yan Scattering (DY) . . . . .	62
4.3.4	Physics Phenomena based on PDFs . . . . .	63
4.3.5	PDFLIB and LHAPDF . . . . .	65

4.3.6	DGLAP Equation . . . . .	67
4.3.7	Free Proton PDF and Bound Proton PDF . . . . .	69
4.3.8	Nuclear PDFs: EPS09 and EPPS16 . . . . .	70
4.3.9	$\hat{p}_T$ Spectra Summation . . . . .	71
4.3.10	Momentum Fraction of the Parton vs $Q^2$ . . . . .	74
4.3.11	Mean Momentum Fraction of the Parton vs $p_T^{\text{hadron}}$ . . . . .	77
4.3.12	Data and MC Comparison : Ratio of Negative To Positively Charged Particle Spectra . . . . .	82
4.3.13	Initial State Effect vs Final State Effect . . . . .	85
4.4	Summary . . . . .	87
5	Summary and Future Outlook . . . . .	89
	References . . . . .	92

## LIST OF FIGURES

Figure	Page
1.1 <b>Left:</b> Coupling Constant $\alpha_s$ [1] as a function of $Q^2$ from various experiments over a wide range of $Q^2$ and at Leading Order (LO), Next to Leading Order (NLO) and Next to Next to Leading order (NNLO), <b>Right:</b> Coupling Constant $\alpha_s$ from different experimental groups with the world average shown along the vertical line. . . . .	4
1.2 Quark Gluon Plasma Phase Diagrams [2] . . . . .	9
1.3 Nucleon Nucleon/Heavy-Ion collision, showing the formation of a lenticular shaped QGP region. The outward pointing arrows refer to the emitted final state particles [3]. . . . .	11
1.4 Nuclear Modification Factor $R_{AA}$ from different several experiments and from different types of nucleon-nucleon collisions [4]. . . . .	13
1.5 Experimental measurements of the nuclear modification factor for both PbPb and pPb collisions. The green and yellow boxes show the systematic uncertainties for $R_{pA}$ and $R_{AA}$ , respectively, while the $T_{pA}$ , $T_{AA}$ , and pp luminosity uncertainties are shown as boxes at low pT around unity, where $T_{pA}$ and $T_{AA}$ are the overlap functions [4]. . . . .	15
1.6 Dividing events into different classes of centrality [5] . . . . .	17
1.7 <i>Nuclear Modification Factor</i> $R_{pPb}$ for positive, negative and all charged particles, measured at mid-rapidity $ \eta  < 1$ within a $p_T$ range of 120GeV/c with data sets from the CMS Detectors [6] . . . . .	19
1.8 A schematic plot of ratio of parton distribution functions $R_i^A(x, Q^2)$ as a function of the momentum fraction of the parton $x$ and at a fixed value of four momentum exchange $Q^2$ [7]. . . . .	20

2.1	Large Hadron Collider Detector Complex [8] . . . . .	23
2.2	CMS Detector Cross-Section [9] . . . . .	24
2.3	Electromagnetic Calorimeter [10] . . . . .	25
2.4	Hadron Forward Calorimeter [10]. . . . .	25
2.5	Zero Degree Calorimeter [11]. . . . .	27
2.6	Schematic for the CERN Grid Computing System. Moving radially outward, the storage capacity and the available number of cores for processing per Tier becomes smaller [12]. . . . .	31
2.7	Modules within the CMS Application Framework [13] . . . . .	32
2.8	Data flow from the CMS Detector online to the <i>Calibration Database</i> and to the Tier-0 for post processing [14] . . . . .	34
2.9	Event Display based on the data collected in November 2016 for pPb collisions [15, 16] . . . . .	37
3.1	Combined spectra of all charged particles for 2013 pPb data [6] . . . .	41
3.2	Combined spectra of all charged particles for 2015 pPb data [4] . . . .	42
4.1	Proton-Proton collision at a very large energy, where several hard-scatterings take place before the onset of hadronization [17] . . . . .	47
4.2	The relationship between the main classes in Pythia 8. The thick arrows show the flow of commands to carry out different physics tasks, whereas the thinner show the flow of information between the tasks. The bottom box contains common utilities that may be used anywhere [18]. . . . .	49
4.3	The lowest tree level diagrams contributing to $q_i\bar{q}_i \rightarrow q_j\bar{q}_j$ , $i \neq j$ [19] . . . .	53
4.4	The lowest tree level diagrams contributing to $q_iq_i \rightarrow q_iq_i$ [19] . . . . .	53
4.5	The lowest tree level diagrams contributing to $q_iq_j \rightarrow q_iq_j$ , $i \neq j$ [19] . . . .	54
4.6	The lowest tree level diagrams contributing to $q_i\bar{q}_i \rightarrow q_i\bar{q}_i$ [19] . . . . .	54

4.7	The lowest tree level diagrams contributing to $q_i\bar{q}_i \rightarrow gg$ [19] . . . . .	55
4.8	The lowest tree level diagrams contributing to $q_i g \rightarrow q_i g$ [19] . . . . .	55
4.9	The lowest tree level diagrams contributing to $gg \rightarrow q_i\bar{q}_i$ [19] . . . . .	55
4.10	The lowest tree level diagrams contributing to $gg \rightarrow gg$ [19] . . . . .	56
4.11	Negative/Positive Spectra for Pythia 8 based internal PDF Sets for all the hard qcd processes. . . . .	58
4.12	Comparing fractional yields for positive and negative charged particles based on quark and gluon switches. . . . .	59
4.13	Negative to positive ratio of hadrons for only quark+quark collisions for inbuilt Pythia 8 PDF Sets. . . . .	59
4.14	Negative to positive ratio of hadrons for only gluon+gluon collisions for inbuilt Pythia 8 PDF sets. . . . .	60
4.15	Deep Inelastic Scattering (DIS) : a lepton collides with a proton to probe the internal structure of the proton [20] . . . . .	62
4.16	Drell-Yan Scattering (DY) : Lepton pair production from parton anti- parton annihilation [21] . . . . .	63
4.17	A schematic plot of ratio of parton distribution functions $R_i^A(x, Q^2)$ as a function of the momentum fraction of the parton $x$ and at a fixed value of four momentum exchange $Q^2$ [7]. . . . .	64
4.18	The distribution functions for the partons based on PDFLIB library, plotted as a function of $x$ at $Q^2 = m_W^2$ , where $m_w$ is the mass of the W boson from [22] and the fluctuations are of the order of 20% can be noticed based on the choice of PDF used for analysis in the u and d quark distribution. . . . .	67

4.19	The figure to the left is the PDF distribution at a smaller value of four momentum $Q^2 = 10 \text{ GeV}^2$ exchanged between the partons and the figure to the right is at a smaller value of four momentum $Q^2 = 10^4 \text{ GeV}^2$ [23] . . . . .	68
4.20	Valence quark, sea quark, EPS09 vs EPPS16 comparison [7] . . . . .	71
4.21	Kinematic reach plots or the $x$ vs $Q^2$ plots, to measure the extent to which the experimental data could be used for the generation of PDFs [7] . . . . .	71
4.22	The ratio of cross-sections from Pythia 8 simulations comparing the free proton PDF of type EPPS16+CT14nlo to that of type another free proton PDF of type EPS09+CT10nlo from the Table. 4.2 . . . . .	73
4.23	The ratio of cross-sections from Pythia 8 simulations comparing the free proton PDF of type CT14nlo to that of type another free proton PDF of type CT10nlo from the Table. 4.3 . . . . .	75
4.24	$\sigma_{\text{PDF Set}}^{\langle \text{collision system} \rangle}$ represents the cross-section of a certain type of collision system and the PDF set based on which the cross-section values are obtained. The plot gives the of comparison for cross-sections from different collision systems, a symmetric pp collision system with two PDF sets CT10nlo and CT14nlo, and an asymmetric pPb collision system with the two PDF sets EPPS16+CT14nlo and EPS09+C10nlo are compared along with the plots shown above for different $\hat{p}_T$ intervals in units of GeV/c . . . . .	76
4.27	Momentum fraction of the parton vs the four momentum exchange for three different intervals $\hat{p}_T$ s 120-170, 300-10K, combined for positive charged particles. Note that the same plots appear identical for negative charged particles as well. . . . .	76
4.25	Spectra of positively charged particles from Tune4C for all $\hat{p}_T$ s after cross-section weighting . . . . .	77

4.26	Spectra of positively charged particles from Tune4C for all $\hat{p}_T$ s <i>before</i> cross-section weighting . . . . .	78
4.28	$\langle x_1 \rangle$ vs hadron $p_T$ for positive and negative charged particles from free proton pdf CT14nlo . . . . .	79
4.29	$\langle x_2 \rangle$ vs hadron $p_T$ for positive and negative charged particles from free proton pdf CT14nlo . . . . .	79
4.30	Comparing the $\langle x_1 \rangle$ for positive and negative charged particle yields for asymmetric pPb type collision based on EPPS16 PDF Set. . . . .	80
4.31	Comparing the $\langle x_2 \rangle$ for positive and negative charged particle yields for asymmetric pPb type collision based on EPPS16 PDF Set. . . . .	80
4.32	Comparing $\langle x_1 \rangle$ vs $\langle x_2 \rangle$ for all partons contributing to positively charged particles. . . . .	81
4.33	Comparing $\langle x_1 \rangle$ vs $\langle x_2 \rangle$ for all partons contributing to negatively charged particles. . . . .	81
4.34	Comparing negative to positive ratios for different collision systems from Pythia simulations by varying the PDF sets (Pb:EPPS16+CT14nlo, p:CT14nlo) and real data for pp, pPb and PbPb collision systems. The dotted lines matching the colors is to show the linearity amongst different collision systems. . . . .	82
4.35	Comparing negative to positive ratios for different collision systems from Pythia simulations by varying the PDF sets (Pb:EPS09+CT10nlo, p:CT10nlo) and real data for pp, pPb and PbPb collision systems. The dotted lines matching the colors is to show the linearity amongst different collision systems. . . . .	83
4.36	Combining the figures 4.35, 4.34 based on the older version (EPS09, CT10nlo) and the newer version (EPPS16, CT14nlo) respectively. . . . .	84

4.37	Ratio of momentum fraction of parton from the Pb going side ( $x_2$ ) to the parton from from the proton going side ( $x_1$ ) . . . . .	85
4.38	Ratio of parton yields as a function of the charge type of the hadron. dpt: d-quark, hqa: HardQCDAI, bfn: Bound and Free Proton Collision, g: gluon, nh: negative charged hadron, ph: positively charged hadron. . . . .	86
5.1	Comparing the Nuclear Modification Factor $R_{pA}$ for a deuteron-gold collision system based on two different experiments PHENIX and STAR and for two different nuclear PDFs EPS09nlo and HKN07 [24]. . . . .	90
5.2	Deviation metrics per gen/tune and observable group [25, 26, 27] . . .	91

## Chapter 1

### Quantum Chromodynamics and Quark Gluon Plasma

#### 1.1 Introduction

Quantum Chromodynamics, also referred to as the theory of strong interactions refers to the interactions between particles, called quarks and gluons, contained inside nucleons protons and neutrons and heavier resonances, where gluons are the mediating particles of the interaction. It was formulated theoretically based on nuclear physics experiments in 1954 by Yang and Mills [28], since then referred to as Yang and Mill's theory.

During the 1940s experiments done to measure the magnetic moment of the proton revealed that a proton has a magnetic moment of  $\mu_P = 2.792\mu_N$  [29] as did the neutron, whose value is  $\mu_N = 2.792\mu_N$  [30].  $\mu_N$  is the magnetic moment of a spin-1/2 particle, given by the expression  $\mu_N = eh/2m_N$ , where  $m_N$  is the mass of the nucleon under consideration. It was very puzzling when this was discovered, since a point like particle wouldn't have a magnetic moment beyond the value given by the formula. It lead to some suspicions that a nucleon might not be a point like particle. What was even more non-intuitive is that the magnetic moment of a particle without an electric charge, like that of a neutron, has a finite and negative value. In a series of experiments done by Robert Hofstadter et. al [31], scattering electrons from the protons elastically, the magnetic moments of the particles were measured, confirming that the proton and the neutron might not be a point like particle. The difference between Hofstadter's experiments and Deep Inelastic Scattering(DIS) experiments [32] is that, the nature of scattering is elastic for the former and inelastic for the

latter. Since, then the experiment was repeated several times to measure the value more precisely. Magnetic moment measuring experiments are done at very low energy, keeping the proton structure intact, while that of DIS are done at a very high energy, where the proton is completely shattered off.

## 1.2 Quantum Chromodynamics (QCD)

### 1.2.1 Gell-Mann's Hypothesis

In the late 1950s, the accelerators became powerful enough, that a lot of new, extremely short lived (lifetime:  $\sim 10^{-23}$ s) resonances were observed, which couldn't be explained theoretically with the ideas of that time. Back then, it was the era of Quantum electrodynamics (QED), which was extremely successful in explaining a lot of properties like the magnetic moment of the muon to several orders of magnitude. However, generalization of QED based theories were not quite successful in explaining the properties of the newly measured resonances, until a new symmetry was proposed.

Gell-Mann's hypothesized that particles like proton, neutron, etc are not elementary, but are composite particles made up of smaller particles called partons. Parton is the collective name for quarks and gluons, where gluons are the force carriers between quarks. He extended the symmetry of the QED from SU(2) to SU(3). Based on this symmetry of YM theory he predicted that the existence of a new type of particle called the  $\Omega$  baryon, which is made up of only strange particles and having a negative charge and three strange quarks. It was observed at Brookhaven National Laboratory (BNL) in 1964 and found to have a mass of  $m(\Omega \approx 1672.450.29)\text{MeV}/c^2$  [33].

By extending the symmetry to SU(3), Gell-Mann successfully classified the hadrons into baryons and mesons separately based on the valence quarks and hadrons are col-

orless singlets. It should however be noted that, although partons i.e. quarks and gluons were proposed, they were not observed as isolated entities like an electron, proton, etc.

### 1.2.2 Asymptotic Freedom

Asymptotic Freedom refers to the property of the YM theory, where under high momentum transfer between the partons  $Q^2 > 1\text{GeV}^2$ , the particles behave like free particles because the running coupling constant becomes very small, however at small momentum transfers, they are strongly interacting with each other. This property helps divide QCD into two regions: *Perturbative Quantum Chromodynamics*(pQCD) and *Non-Perturbative QCD* (npQCD) based on the magnitude of the strong coupling constant.

$$\alpha_s(Q^2) = \frac{12\pi}{33 - 2n_f \ln\left(\frac{Q^2}{\Lambda^2}\right)} \quad (1.1)$$

This formula for the coupling constant is a function of the momentum transfer between the interacting partons. It is also dependent on the number of flavors  $n_f$  and the renormalization point  $\Lambda$ , with a value of  $0.2\text{GeV}$ . The equation clearly reflects that, if the momentum transfer gets very small close to  $\Lambda$ ,  $\alpha_s$  becomes very large, because mathematically logarithm doesn't have a value at 0. The property of *Asymptotic Freedom* is based on this equation and was discovered by Wilczek and Gross [34] in the year 1973 for QCD from the Yang-Mill's theory. The physical meaning of the property is that, at very large momentum exchanges between partons, the coupling constant becomes very small, and the partons behave like freely moving particle, but at very low momentum transfers, they are strongly interacting., which is counter-intuitive. pQCD corresponds to the domain of large momentum

transfers and npQCD corresponds to the domain of small momentum transfers between partons. Since then the QCD related Feynman diagrams are being calculated to increasingly larger orders of the coupling constant  $\alpha_s$ . Also, this property is vital for the applicability of *Factorization*, without which the required cross-sections cannot be treated independently because of the underlying correlations that arise in any  $2 \rightarrow 2$  scattering of partons.

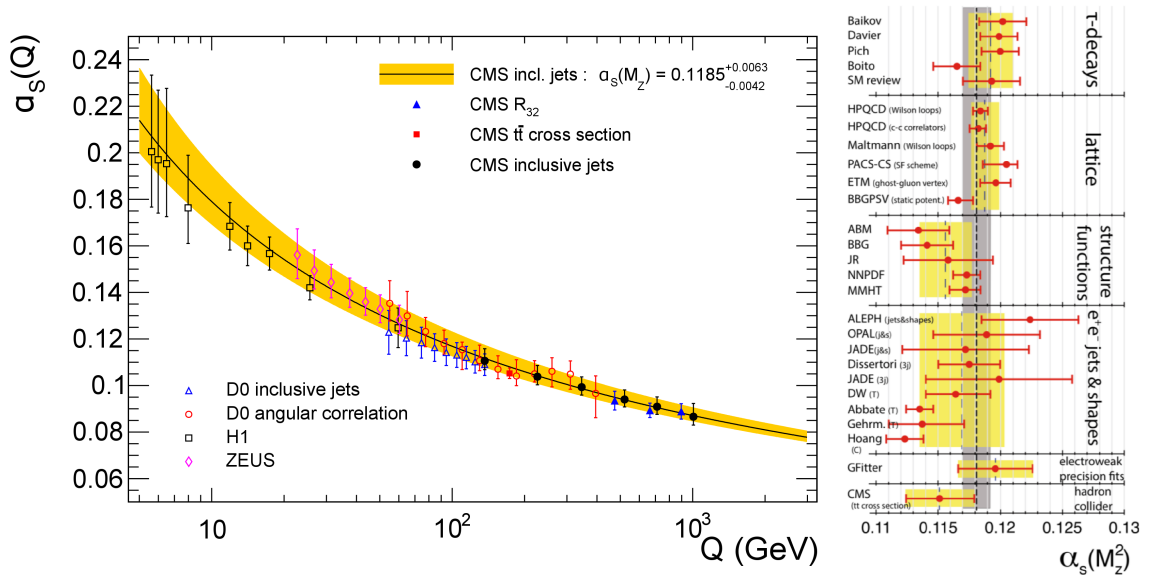


Figure 1.1: **Left:** Coupling Constant  $\alpha_s$  [1] as a function of  $Q^2$  from various experiments over a wide range of  $Q^2$  and at Leading Order (LO), Next to Leading Order (NLO) and Next to Next to Leading order (NNLO), **Right:** Coupling Constant  $\alpha_s$  from different experimental groups with the world average shown along the vertical line.

As it will be explained in the following chapters, the Monte Carlo (MC) generator Pythia is based on the *Leading Order* cross-section from pQCD. To this date, nearly all the results based on pQCD have been validated by experimental groups all over the world and a lot of packages were developed to calculate Feynman diagrams to increasing orders. The magnitude of the coupling constant measured by different experimental groups is shown Fig. 1.1 and is consistent with experimental uncertainties and varying between 0.112 to 0.118. It is a key parameter for this work because

the evolution of parton distribution functions are based on this quantity, therefore any errors introduced will be propagated into the simulation. Parton Distribution Functions (PDF) are the distribution of momentum of the partons inside the nucleus.

In the domain of perturbative QCD (pQCD), the cross-sections can be analytically calculated, hence it is relatively straightforward to compare with experiment and a lot of symbolic computations are being developed rapidly for this purpose, since the creation of the very first symbolic package referred to as *Schoonschip* [35] by Veltman. However for the case of Non-Perturbative QCD (npQCD), the calculations are no longer possible because the coupling constant becomes very large and there is no recipe invented yet for analytical computation.

Given that pQCD provides a way to do QCD calculations, the domain of npQCD remains much an open problem to this day. In the recent times, *Non-Perturbative QCD* based calculations are handled numerically and the domain is referred to as Lattice QCD [36]. It is a whole new field in itself and is computationally very expensive as the size of the lattice is increased. The basic idea in doing lattice QCD simulations is to position quarks on a lattice and let the system evolve stochastically. The YM theory is written down as a difference equation based on the distance between the quarks on the lattice instead of having continuous variables. A lot of challenges have been dealt with in the past to address these problems and lattice QCD has now been successfully used in high-performance computing environments to obtain the masses of some of the hadrons.

Although QCD is very successful in explaining some of the properties of hadrons, it remains to this day, a largely elusive theory, because there are no recipes available to analytically compute the properties of hadrons from first principles. With the

evidence gathered for more than five decades since the formulation of YM theory and with a lot of experimental data and the pioneering calculations by several physicists, it should in principle be possible to bridge the gap between nuclear physics, and high energy physics. However this has not been the case. Not surprisingly, in order to address the mathematical complexity introduced by Yang-Mills theory, it led to the birth of new ideas like *String Theory*, whose results found applications to many body QCD.

### 1.3 Quark Gluon Plasma (QGP)

During the mid 1970s [37, 38, 39] QGP was proposed as the deconfined state of nucleon matter following the quark model and the discovery of asymptotic freedom because of the non-Abelian nature of the interaction between partons.

Such a state of matter is realized experimentally in relativistic heavy-ion collisions [40], where, at least one of the colliding particle is a nucleus like Pb, a new state of matter is produced, where the partons inside the nucleons are deconfined, just like the case of a plasma, where positive and negative charged particles exist in a separated phase. The plasma is an extremely short-lived state of matter ( $\tau_{\text{QGP}} \approx 10^{-23} s$ ) created during the heavy-ion collisions at relativistic energies. This phase of matter is more relevant to a situation, where the energies involved in the collision are several times larger than the mass of the nucleon. Shuryak coined the phrase Quark Gluon Plasma(QGP) for this new state of matter, where colored objects would exist in a gas like phase before converting into colorless objects.

Subsequently, physicists have proposed several observables like *Particle Correlations* [41, 42] and the *Nuclear Modification Factor* [43, 44], etc, that can be compared with experiment within the context of QGP to analyze the properties of the cre-

ated medium. *Correlations* are used to understand the collective properties of the interacting particles.

As with any many-body problem, correlations are a useful observable to understand the relationship among the phenomenological variables. In the case of heavy ion collisions as well, particle correlations help illuminate the link between the flow of particles in relationship to the shape of the region from which the particles are emitted. Large experimental collaborations like Relativistic Heavy-Ion Collider (RHIC) at Brookhaven National Labs(BNL), Large Hadron Collider(LHC) at CERN, are used to study the properties of QGP. Since the energy involved in the collision is very large, the accelerators needs to be configured to handle the large luminosities in heavy-ion collisions, due to which the accelerator complexes hosting several detectors are usually very large in size.

Since the temperatures involved in the production of QGP are very large, the study of QGP helps explore various properties that could not be obtained by first-principles thermodynamics and QCD calculations. The collective properties of quantum mechanical systems have always been a challenge to explain from ab-initio methods; thus QGP serves as a probe to understand the collective effects. Although QGP is heavily phenomenological, a lot of the ideas helped validate QCD itself. For example, the property of asymptotic freedom which corresponds to a small coupling constant at large momentum transfers between parton level scatterings helped model QGP as a relativistic free gas with more number of degrees of freedom like color and flavor, without which it wouldn't be possible to model such a complex state of matter thermodynamically. QGP also serves as a bridge between perturbative and non-perturbative phases QCD, to validate various assumptions on the basis of QCD alone. For example, particle production cross-sections calculated using pQCD were found to match with experimental evidence and Monte Carlo simulatons are heavily

based on these formulae.

### 1.3.1 Jet Quenching

The phenomena of *jet quenching* [45] plays an important role in the context of QGP because jets help us understand a lot about the properties of QGP medium. During the very onset of parton-parton collisions, due to the very high four momentum exchange, partons have a lot of energy. Such a large exchange of energy, will let partons fragment further, until they reach a point where hadronization can take place. This process of fragmentation is where a parton can generate more partons further. Because of this, a cone-like region in which the partons tend to be accumulated and moving forward. This cone is referred to as a jet of partons.

If the jet is produced in a medium like a QGP, then, the production of jets is naturally softened from a highly collinear pencil of partons interacting with the medium to loose momentum quickly, compared to a situation where there is no medium. Such a phenomenon is referred to as *Jet Quenching*. Studying the spectra of jets helps understand the effect of medium quantitatively, hence it forms an important sub-discipline in the area of Quark Gluon Plasma.

Since, the objective of this thesis is to understand why the ratio of positively and negatively charged particles show a difference, an understanding of jets helps us gain insight along with the other parameters that the yields depend upon. Since quarks have electrical charge, the jets that come out of positively charged quarks and negatively charged quarks can have an effect on the final state hadrons, unlike gluons, which do not have an electric charge. The yields of quarks vs gluon jets helps quantitatively account for the yields just before hadronization. These can be eventually

compared to the final state for any quantitative picture of the positively to negatively charged particles. It should also be appreciated that quark to gluon ratios are hard to disentangle experimentally, but, a qualitative understanding can be sought after by studying the spectra of jets or hadrons.

#### 1.4 Phase Space Diagram

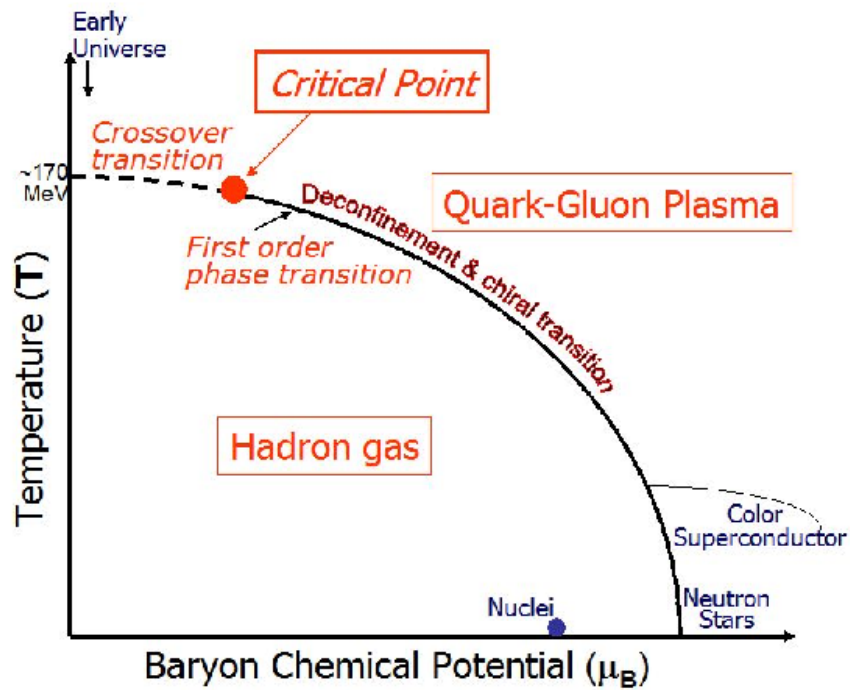


Figure 1.2: Quark Gluon Plasma Phase Diagrams [2]

In order to understand the contribution of Quark Gluon Plasma to the global picture of QCD, a *Phase Space Diagram* [46] is often used. It relates the change of one thermodynamic variable with respect to another where these can be any of the mathematical quantities like pressure, volume, etc. In order to explore QGP, a frequent choice is the temperature ( $T$ ) of the system vs, the baryon chemical potential  $\mu_B$ . *Chemical potential*( $\mu$ ) is an extensive thermodynamic quantity introduced to account for changes in the system when a particle leaves or enters the system. Baryon

chemical potential helps explore the differences in number of baryons, since *baryon number* has the status of a quantum number. Within the domain of QGP, phase diagrams help pin down the temperature at which the phase transition from nuclear matter to quark-gluon plasma happens. The Fig. 1.2 is extremely important because of the bridge it can potentially create from between experiment and theory. Doing a Lattice QCD simulations in itself is very expensive, considering the possibility that several nucleons are present is even more computationally expensive. Hence, inputs from heavy-ion collisions via experiments are obtained to plot Fig. 1.2. It should be noted that, the quantities obtained within the context of QGP are done phenomenologically and from thermodynamics.

Since quarks and gluons have not been observed as isolated particles, QGP based experiments helps us understand their properties and validate the models based on these particles. A lot of models like Pythia [47], Hijing [48], EPOS [49] were developed since an ab-initio calculation of QGP properties from basic QCD is computationally very expensive.

Relativistic heavy-ion collisions also help distinguish the cold nuclear medium from the hot nuclear medium. Cold Nuclear Medium is the phase of matter where the partons scatter off partons from other nucleons inside the nucleus. Hot Nuclear Medium is where, a lot of nucleons are wounded in a collision, leading to a deconfined phase of partons, which interact with the generated medium as opposed to undergoing scattering with cold nucleons.

Along with the aforementioned properties, QGP also helps quantitatively estimate the more fundamental properties of Quantum Chromodynamics (QCD) like *Phase Transitions* and *Equation of State*. Phase Transitions help understand the QGP as a deconfined state of matter, for which the phase diagram is often used and

the *Equation of State*, help obtain the relationship amongst the thermodynamic variables like pressure, temperature, volume, chemical potential, etc for a QGP medium.

#### 1.4.1 Different Phases of QGP formation

The cartoon 1.3 shows the collision between two nuclei, where the lenticular shape is the region through which particles are emitted and is the region containing the Quark Gluon Plasma. The QGP medium goes through various phases, before the final state particles are produced, which are eventually detected by the detector.

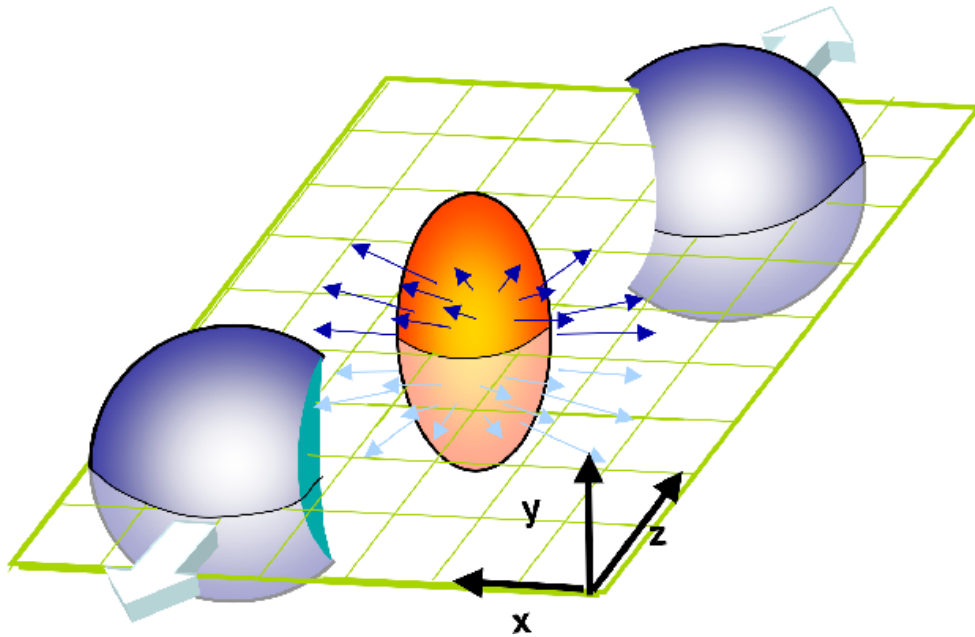


Figure 1.3: Nucleon Nucleon/Heavy-Ion collision, showing the formation of a lenticular shaped QGP region. The outward pointing arrows refer to the emitted final state particles [3].

1. *QGP Fireball* : This phase of matter corresponds to the deconfined phase of quarks and gluons generated immediately after the inelastic collision between the nucleons, where the partons participate in the hard scattering processes and undergo multiple scatterings in this non-equilibrium system. In various

simulation programs like Pythia, the Leading Order(LO) cross-sections have been used to model the scattering processes.

During this phase, the partons not only scatter amongst themselves elastically, but also produce more and more partons via fragmentation processes inside the fireball.

2. *Chemical Freeze-out* : Particle production ceases at the partonic level and the system transitions to a phase where hadronization begins to take place, i.e. the coalescence of quarks into colorless objects called hadrons. Any scattering process that might take place happens at the hadron phase and not at the partonic level. Note that most of the hadrons produced undergo further decay eventually.
3. *Kinetic Freeze-out* : This is the phase, where no further interactions happen via strong interactions i.e. no hadron level interactions. The system now behaves like a non-interacting hadronic relativistic gas, which eventually decays into various long-lived particles and stable particles.

#### 1.4.2 Hot Nuclear Medium and Cold Nuclear Medium

*Cold Nuclear Medium* refers to the state of matter, where the partons from a deconfined state of matter in a p+A collision are interacting with nucleons inside a nucleus, in which nucleons other than those from which partons are deconfined [50]. Since the partons scatter several times inside a nuclear medium which is relatively cold, it helps explore the nature of the nuclear system from which the partons hadronize. By studying this state of matter, one can better explore the underlying nature of the ground state nuclear medium.

On the contrary, *Hot Nuclear Medium* is the state of matter produced in a highly central heavy-ion heavy-ion collision like that of a PbPb collision, where the result of the collision is a deconfined state of matter, with no free nucleons available for partons to scatter off before hadronization as there are in cold-nuclear matter.

The following experimental result describes the results for the *Hot Nuclear Medium* from various experiments at various energies and for identified particles as well for a wide  $p_T$  range from  $[1, 120]$ GeV/c.

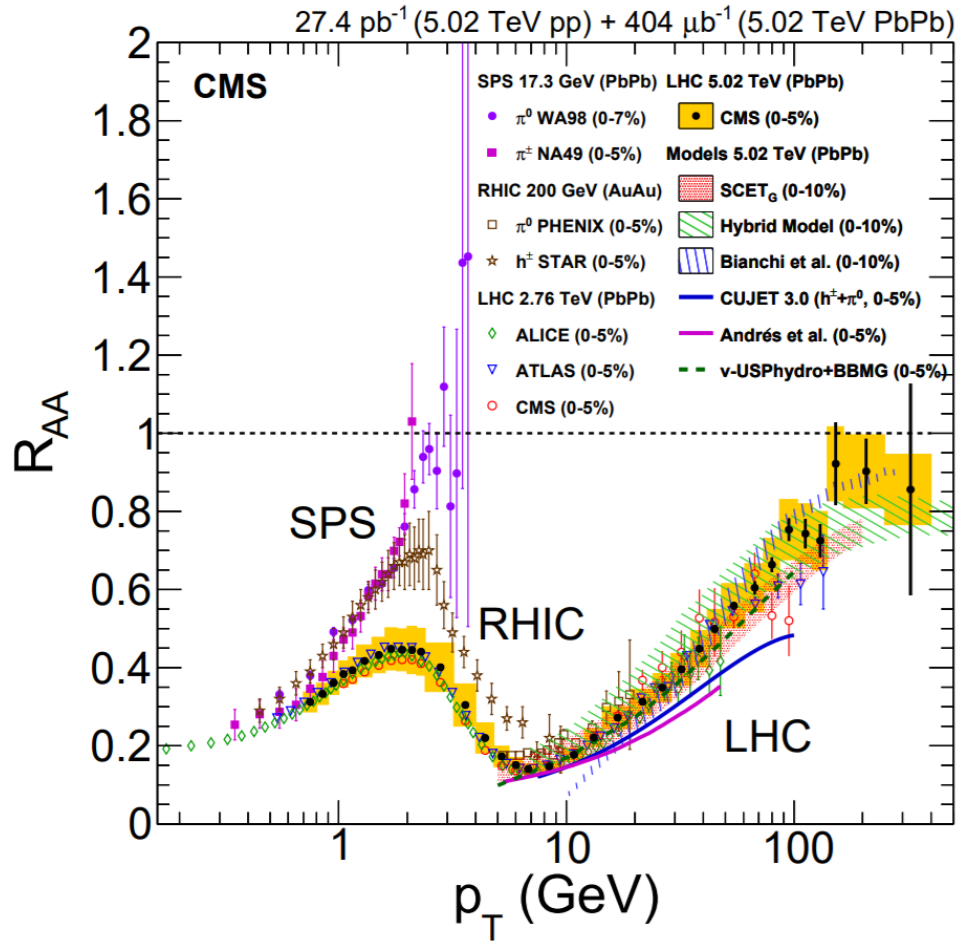


Figure 1.4: Nuclear Modification Factor  $R_{AA}$  from different several experiments and from different types of nucleon-nucleon collisions [4].

*Nuclear Modification Factor* is defined as the ratio of particle yields of a certain type in one collision type compared to another collision type. The physical meaning of the observable nuclear modification in this particular plot 1.4 is that the aggregate number of charged particles produced in a PbPb collision system within a certain  $p_T$  bin and  $\eta$  range, averaged over a large number of events is smaller than the aggregate number of charged particles in a proton-proton collision, averaged over the same number of events and normalized to the equivalent number of proton-proton collisions. The normalization factor  $N_{\text{coll}}$  is obtained from the *Glauber Model*. The yields in two different collision systems are compared, thus this observable helps illuminate the effects related to the medium. Because, the probability of production of particles are modified because of the medium with, a conclusion based on comparison with several phenomenological models like HIJING, Pythia and the Glauber Model to which the data are compared. It should be noted that HIJING has the effect of jet quenching included. Pythia doesn't have any information about QGP, and the Glauber Model is a purely geometry based.

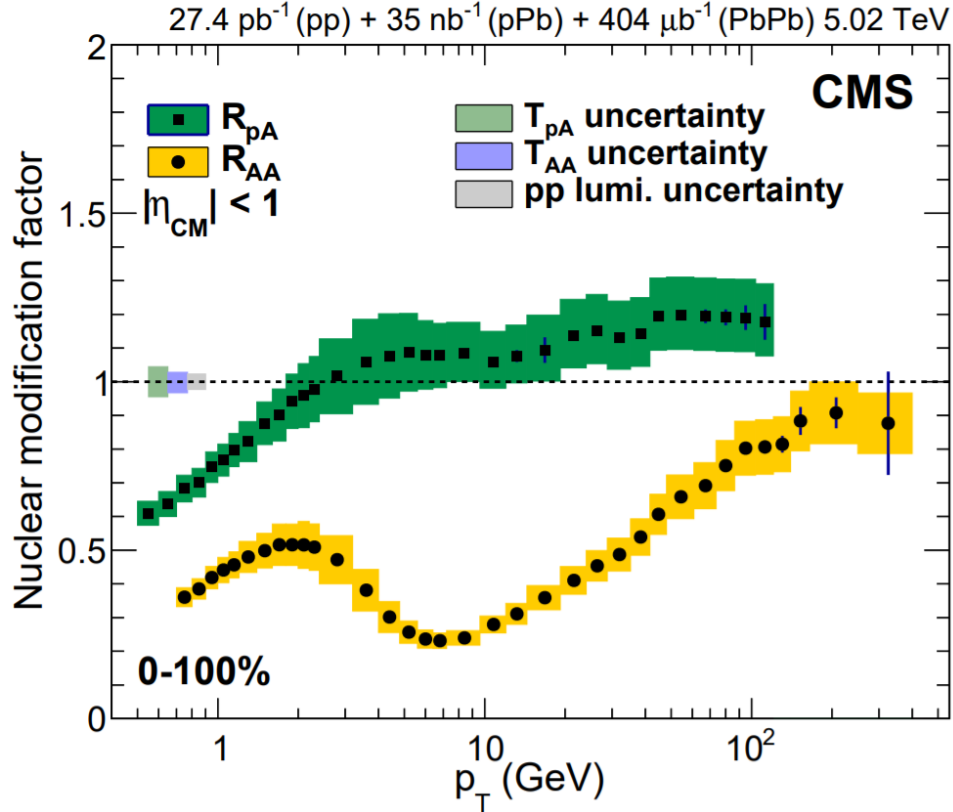


Figure 1.5: Experimental measurements of the nuclear modification factor for both PbPb and pPb collisions. The green and yellow boxes show the systematic uncertainties for  $R_{pA}$  and  $R_{AA}$ , respectively, while the  $T_{pA}$ ,  $T_{AA}$ , and pp luminosity uncertainties are shown as boxes at low  $p_T$  around unity, where  $T_{pA}$  and  $T_{AA}$  are the overlap functions [4].

To study the effect of a nuclear medium, physicists have employed a similar, yet much more fundamental observable also referred to as the nuclear modification at nucleon level, which is the ratio of the parton distribution functions in a nucleus versus the parton distribution functions in a free proton. Parton Distribution Functions (PDFs) are key inputs that can only be obtained experimentally; they contain information about the momentum fraction of a parton inside a nucleon at a certain momentum transfer in a  $2 \rightarrow 2$  scattering.

It should be remembered that the outgoing hadrons are a product of hard scattering amongst partons, followed by multiple scattering and hadronization. Hence,

the study of the PDF of a nucleon inside a nucleus vs the PDF of a free proton in vacuum help us understand the nuclear medium.

## 1.5 Centrality of a Heavy Ion Collision

Centrality [5, 51] is an important experimental observable used to quantify the number of nucleons participating in a collision. Depending upon the *impact parameter* involved in the collisions, the number of outgoing particles can vary. It can be a highly central collision, if the impact parameter is near zero or a peripheral collision if the impact parameter is near maximum. Impact parameter is the distance between the centers of the two participating colliding species. If it is a more central collision, the nucleons participating in the collision, referred to as the wounded nucleons, can be very large.

Based on Fig. 1.6, it can be inferred that there's a difference in the particle yields depending on how central the collision is or how small/large the impact parameter might be.

Intuitively, if no reaction has taken place, the number of particles  $N_{\text{ch}}$  observed in a very forward direction will be small.

Hence, the collision is very peripheral and on the contrary, if a reaction has taken place, a lot of charged particles will be observed in the pixel tracker detector and in other detectors as well and less in the forward detector, hence the centrality would be very high.

The variables are plotted as a function of events, and divided into different classes referred to as *Centrality Classes*, and a percentage is allotted to them from 0-100,

where 100 means the most central and 0, being the most peripheral collision. For the CMS detector, the energy deposit from the Hadron Forward (HF) calorimeter is used along with the tracking detector to measure the centrality.

There is a clear difference between a proton-lead collision vs a lead-lead collision from the nuclear modification plots and this effect becomes more pronounced at higher  $p_T$ . The effects of the nuclear medium are quite apparent as well.

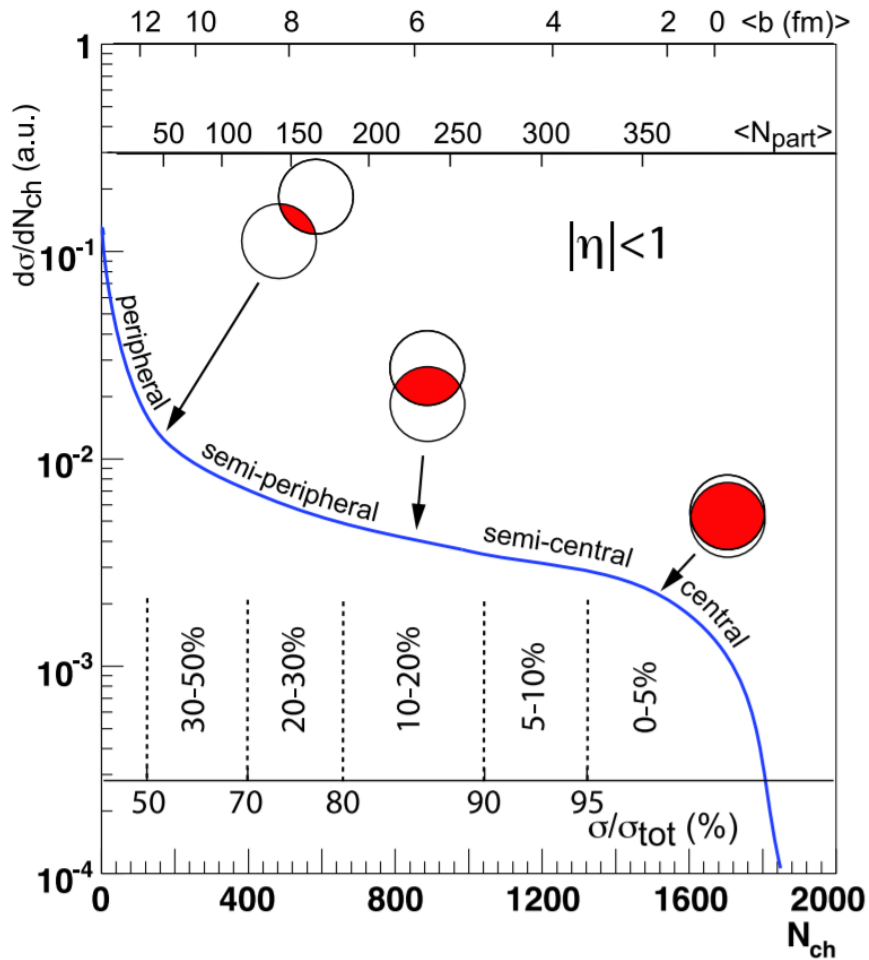


Figure 1.6: Dividing events into different classes of centrality [5]

Centrality is modeled theoretically based on the Glauber Model [52], where the mean number of binary collisions  $N_{coll}$  is obtained.

## 1.6 Glauber Model

The *Glauber Model* [53] is a Monte Carlo program used to calculate the number of participating nucleons ( $N_{\text{part}}$ ), mean number of binary collisions ( $N_{\text{coll}}$ ) and the overlap function  $T_{AB}(b)$ , where  $b$  is the impact parameter. The basic idea behind this model is that a nucleus is constructed by placing the nucleons based on the three-parameter Woods-Saxon nuclear distribution function, and since the nucleons can't overlap, the minimum distance between the nucleons is chosen based on the inelastic nucleon-nucleon cross-section.

The *Woods-Saxon* function [54] is a widely accepted distribution function for the distribution of nucleons in the nucleus spatially and it is parameterized based on a Fermi distribution. Several simulation codes like HIJING, VENUS, RQMD are based on this parameterization. Its functional form is as shown below:

$$\rho(r) = \rho_0 \frac{1 + w (r/R)^2}{1 + \exp\left(\frac{r-R}{a}\right)} \quad (1.2)$$

where  $R$  is the radial size of the nucleus,  $\rho_0$  is the density of the nucleus at the center,  $a$  is the skin-depth and  $w$  is a measure of the deviation from the spherical shape of the nucleus.

## 1.7 Motivation and Objective of this Thesis

The main motivation for this thesis is based on the observed asymmetry in the negative to positive charged particle distributions in the nuclear modification factor

from the experimentally observed, but unpublished analysis note (AN12-017) from the CMS experiment at LHC.

This asymmetry of charged particles is at least to the first order, is expected to be a consequence of nucleon level PDF distributions i.e. due to possibly an initial state effect or a final state effect. *Initial State* refer to the partons that participate in the scattering process related to the final state hadrons and *Final State* refer to the partons just before hadronization related to the final state hadrons. To understand this phenomenon, simulations with Pythia were performed by modifying the PDF sets and the results are given in Chapter 4.

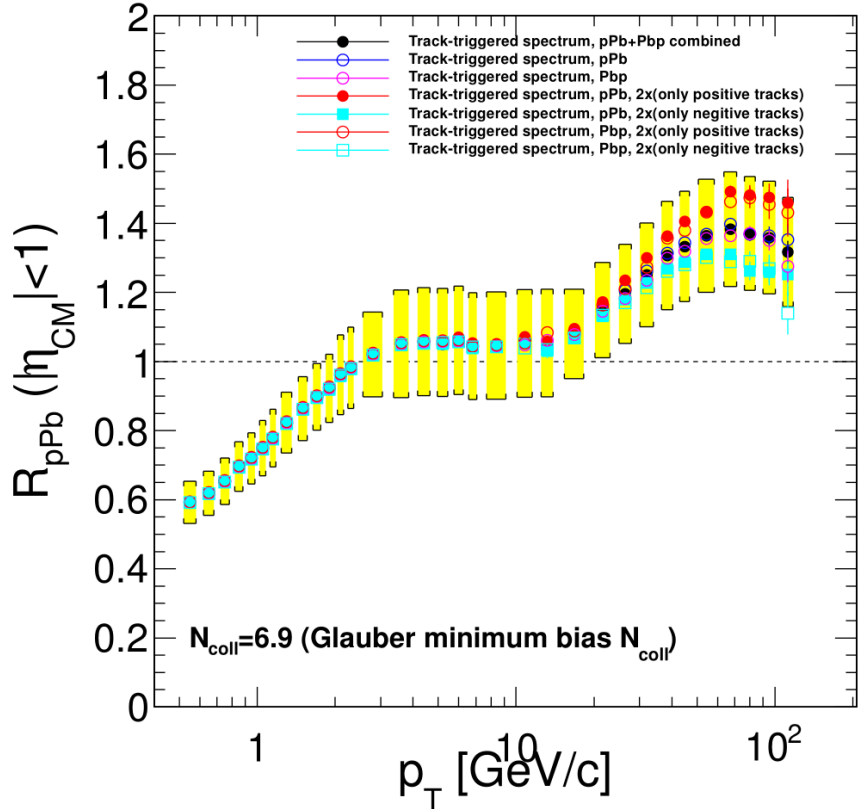


Figure 1.7: *Nuclear Modification Factor*  $R_{pPb}$  for positive, negative and all charged particles, measured at mid-rapidity  $|\eta| < 1$  within a  $p_T$  range of 120 GeV/c with data sets from the CMS Detectors [6]

The physics reasons for this is that, the production of particles in a high energy collision happens because of due to parton level hard scatterings. The Fig. 1.7 compares a proton-lead collision with a proton-proton collision. Therefore, the primary cause expected is due to the difference in the nuclear parton distribution functions (PDFs) from a nuclear PDF and a free proton PDF.

In order to quantitatively account for such a difference, a more fundamental observable also referred to as nuclear modification factor, but at parton level is considered.

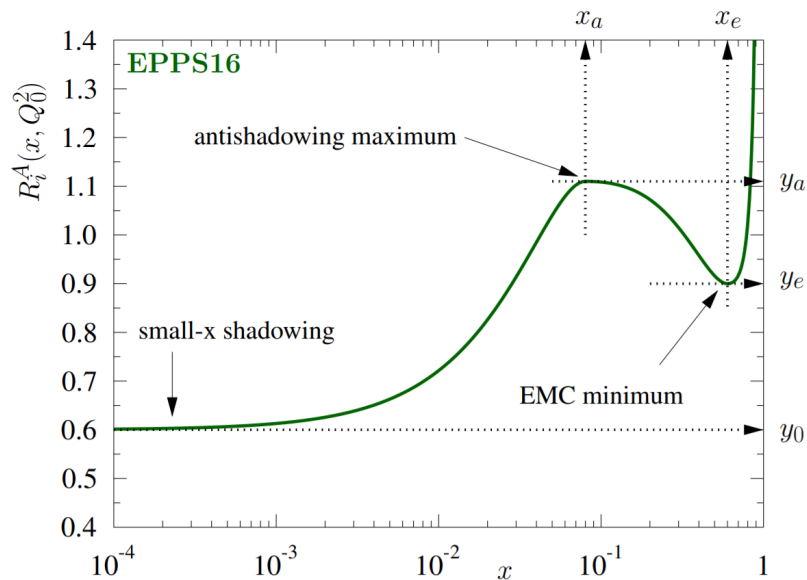


Figure 1.8: A schematic plot of ratio of parton distribution functions  $R_i^A(x, Q^2)$  as a function of the momentum fraction of the parton  $x$  and at a fixed value of four momentum exchange  $Q^2$  [7].

This observable is the ratio of nuclear PDF and a proton PDF against the momentum fraction of the parton participating in the hard-scattering at the onset of collision for both the collision systems. It should be noted that, the results presented in Chapter 4 are possible due to the availability of nuclear Parton Distribution Function(PDF) sets for lead as well as proton and with the options available in the Monte Carlo simulator to use the PDF sets. More about this topic is explained in Chapter 4.

There are three distinct regions in the plot, depicting the physics phenomena involved due to the hard-scattering of partons, labelled as *small-x shadowing*, *antishadowing*, and the *EMC minimum*. More explanation about this phenomena can be read from the Section 4.3.4 *Physics phenomena based on PDFs* in Chapter 4.

## 1.8 Summary

- Yang Mill's theory formulated in 1954.
- Gell-Mann's proposed that hadrons are no longer elementary, but made up of partons [quarks and gluons].
- The property of Asymptotic Freedom for the YM theory was proved in 1973.
- Edwark Shuryak coins the word Quark Gluon Plasma (QGP) as the deconfined state of sub-nucleonic matter.

## Chapter 2

### Experiment

#### 2.1 CMS Detector at LHC

The LHC is a 27km circular accelerator with five interaction points, where each of the detectors CMS, ATLAS, ALICE, LHCb, LHCf are located. The Compact Muon Solenoid (CMS) is one of the detectors at LHC, situated at Cessy on the French side. It is worth remembering that, it took several years, a lot of money and man power to build a detector of such complexity, which is a major accomplishment in the history of mankind in helping expand the understanding of natural phenomena.

In the next few sections, the components of the detector are described briefly, [55, 56].

##### 2.1.1 Superconducting Magnet

State-of-the-art technology is used to build the superconducting magnet for the CMS detector, given the large amount of magnetic field that is needed to for bend the charged particles at velocities close to the velocity of light. The CMS detector has a solenoidal superconducting magnetic enclosing the ECAL, HCAL and the Tracker Detectors and a tube carrying the beams.

The superconducting solenoidal magnet has a diameter of 6m and a length 12.5m. It can store about 2.6GJ of energy at full current. The magnetic material is based on the Niobium, Titanium alloy. The field energy is so large, that the alignment of the mechanical structure can change because of the magnetizing and demagnetizing cycles

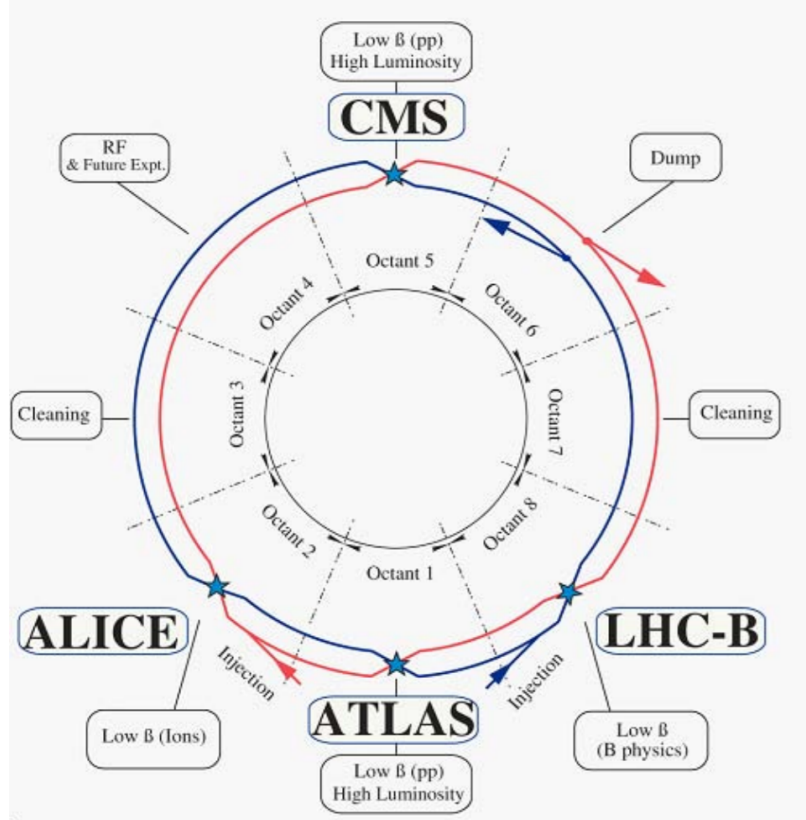


Figure 2.1: Large Hadron Collider Detector Complex [8]

and there is a dedicated team to keep track of the changes. To power the solenoid, the bipolar thyristor power convertor rated at 520kW with LC filters is used. Stored magnetic energy is extracted by thermal dissipation in the *dump resistor*. NbTi is cooled by liquid He, at a critical temperature,  $T_c = 7.3\text{K}$  at  $B = 4.6\text{T}$ , and the operating current is 19,143 amperes.

### 2.1.2 Electromagnetic Calorimeter (ECAL)

ECAL is a calorimetric detector used to measure the energy deposited by the particles. For example, the energy deposited by photons from pions, eta mesons, etc are measured by this detector. It is made up of 61200  $PbWO_4$  crystals made up of two pieces, the ECAL Endcap(EE) and ECAL Barrel(EB). The crystals have

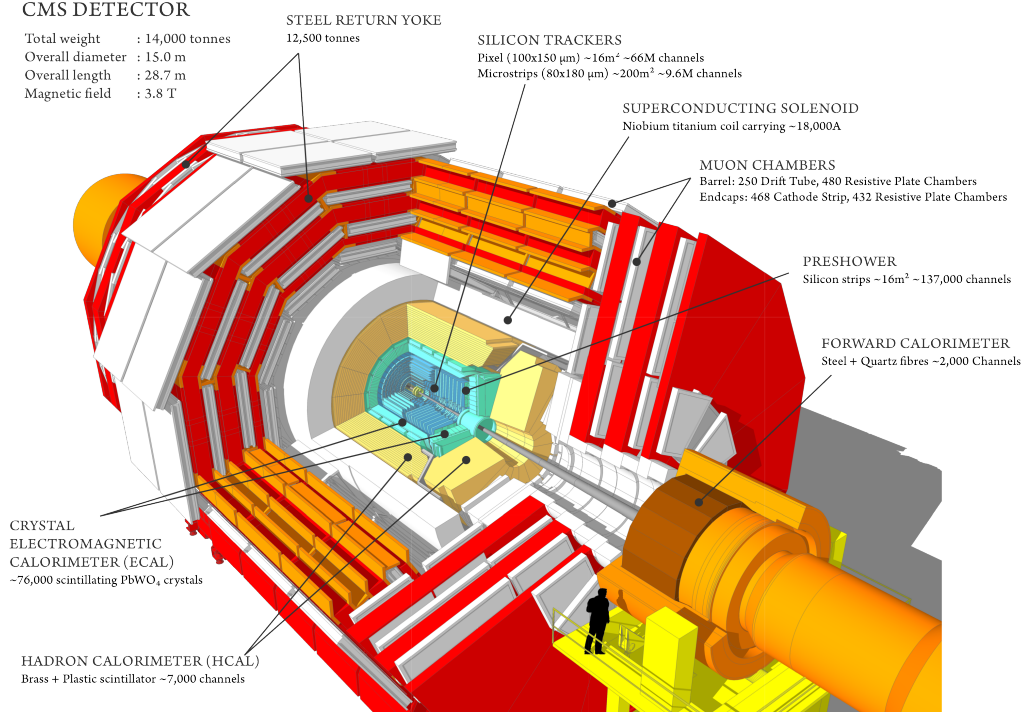


Figure 2.2: CMS Detector Cross-Section [9]

a radiation length, which is of the order of 0.89cm and a Moilere length of 2.2cm. About 80% of the light is emitted within 25ns. Avalanche Photo diodes (APDs) are used as photodetectors for the barrel and vacuum phototriodes (VPTs) are used in the end caps. The rapidity interval over which the ECAL can perform calorimetry is  $|\eta_{\text{Barrel}}| < 1.479$ . The radius of the barrel is  $r = 1.29\text{m}$ , from the axial line that coincides with the beam pipe to the front faces of the crystals facing towards the axial line. The radius of the barrel section (EB) has an inner radius of 129cm, having a pseudorapidity coverage of  $0 < |\eta| < 1.479$  and the Endcaps (EE) have an inner radius of 314cm from the vertex covering a pseudorapidity range of  $1.479 < |\eta| < 3$ , each structured as two Dees. The readout system is structured in sets of 5x5 crystals. The energy of the measured particle is estimated based on the chosen matrix of crystals into which the energy is deposited.

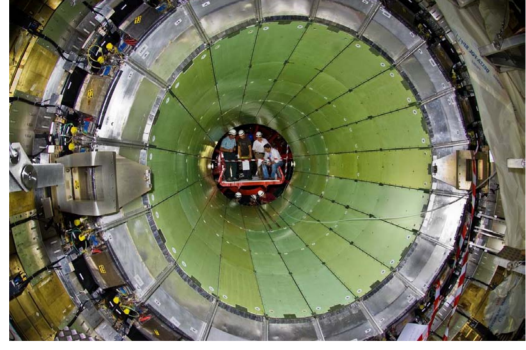
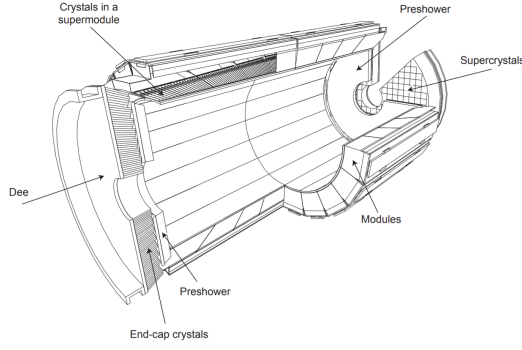


Figure 2.3: Electromagnetic Calorimeter [10]

### 2.1.3 Hadron Calorimeter(HCAL)

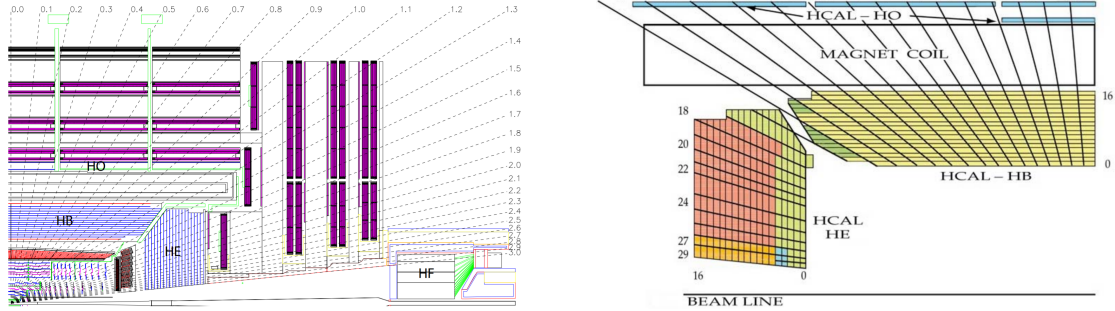


Figure 2.4: Hadron Forward Calorimeter [10].

The hadron calorimeter is used to measure the missing transverse energy  $E_T$  of the hadrons. It is made up of 4 parts, Hadron Barrel(HB), Hadron Outer(HO), Hadron Endcap(HE) and Hadron Forward(HF) and is similar in the design to ECAL. The detector is made up of a plastic scintillator and has wavelength shifting fibers. Each of the four pieces covers a different pseudorapidity interval, i.e. HB covers a pseudorapidity interval of  $|\eta| < 1.4$ , with a granularity of  $\Delta\eta \times \Delta\phi = 0.087 \times 0.087$ , with 2304 towers, the HO covers  $|\eta| < 1.26$  and is made up of tiles grouped in  $30^\circ$  sectors segmented along  $\phi$  radially, and divided into 5 sections along the  $\eta$  referred to as rings, the HE, covers  $1.3 < |\eta| < 3$ , has a variable segmentation scheme and is made up of 2304 towers; the HF covers  $3 < |\eta| < 5$  and has a variable segmentation scheme that fits with the overall structure as shown in Fig. 2.4

#### 2.1.4 The Muon System

Muons are reconstructed from the muon system and the tracker detector. The process of reconstruction happens by matching the hits in the muon chambers with that of the tracks from the pixel trackers, and it employs the track extrapolation technique to estimate the path the muon must have taken and to the most probable location in a chosen detector. Muons are measured based on the choice of scanned cone size in  $\eta, p_T$  ranges of the silicon track. The method depends on the choice of the seed, and the five trajectory parameters. The reconstruction of muons that are well measured is faster and with higher efficiency compared to the poorly measured ones. The choice of resonances for muon production is  $Z \rightarrow \mu^+ + \mu^-$ ,  $Z' \rightarrow \mu^+ + \mu^-$ ,  $J/\psi \rightarrow \mu^+ + \mu^-$  and other Drell-Yan dimuon samples within the mass range of 70 to 1000 GeV/ $c^2$ .

Muons are also observed as background sources from the cosmic-ray and beam-halo as well, they are predominantly used for calibration, alignment, triggering, and reconstruction efficiency. The reconstruction algorithms for muons from heavy ions collisions are different from that of a pp based reconstruction.

#### 2.1.5 Forward Detectors

There are two major calorimetric detectors CASTOR and Zero Degree Calorimeters (ZDC) used to measure physics at lower Bjorken-x ( $\sim 10^{-6}$ ), and centrality in AA collisions respectively and can also be used to tag the ultra-peripheral events as well.

CASTOR is an azimuthally symmetric electronic/hadronic calorimeter covering a pseudorapidity range of  $5.3 < |\eta| < 6.5$ , for the EM section and  $5.15 < |\eta| < 6.4$

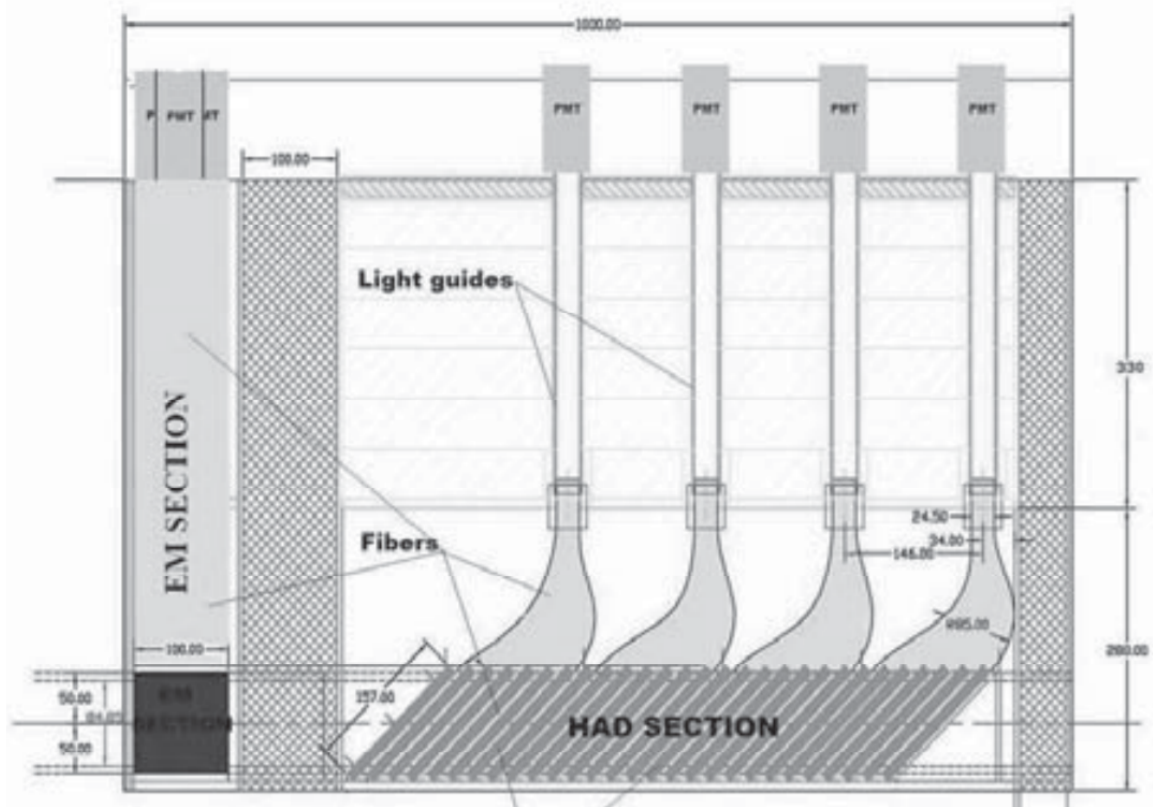


Figure 2.5: Zero Degree Calorimeter [11].

for the hadronic sections. It has 16 sectors divided along the azimuth and 12 slices referred to as Reading Units (RU) to measure the propagation of hadronic cascades.

Since the ZDC is used for centrality, its basic design requirement is to resolve a single neutron efficiently and it should have good energy and time resolution and should be made up of a radiation hard material. During the design, a single neutron with an energy of about  $1TeV$  is resolved with the peak having a width of  $\sim 12\%$ .

### 2.1.6 Tracking Subsystem

Since positively charged particles bend in a direction opposite to the negatively charged particles and such a differentiation is essential for this analysis, this detector subsystem is ideally suited for this analysis, owing to its excellent momentum reso-

lution, enabling accurate measurement of transverse momentum  $p_T$  of the particles. The outermost radius of the tracker extends to about 110cm and the length of the tracker is 540 cm.

### 2.1.6.1 Track Reconstruction

The main purpose of the tracking detector is to detect the stable charged particles and any particle that has a decay range within the tracking detector can be detected as well. Whenever a charged particle enters a magnetic field, it bends in a certain direction depending on the polarity of the charge, be it positive or negative. The direction in which the positive charged particle bends is opposite to that of the negative charged particles. The multiplicity of charged particles is very high in a pPb collision compared to a pp collision and the CMS tracking detector is able to withstand such large multiplicities in a pPb collision and has the computing power to do online reconstruction. Approximately 3000 charged particles per unit rapidity would be detected in a typical central collision. The tracking detectors works by doing pattern recognition based on a lot of tracklets reconstructed based on the hits registered in the Si pixel. This detector is central to this analysis, because of the measurement of both positive and negative charged particles; polarity is of an important concern here and hence, any real measurement would require the need to check for efficiencies for both types of charged particles. The method of track reconstruction is based on the following 5 steps.

- *Hit Reconstruction*: In which the clustering of strips or pixels is done to estimate the position and uncertainty.
- *Seed Generation*: The choice of initial trajectory candidates is necessary to start reconstructing the tracks. The five parameters  $d_0, z_0, \phi, \cot \theta, d_0 = y_0 \cos \phi -$

$x_0 \sin \phi$ , are chosen for the fit.  $x_0, y_0$  are the transverse coordinates of the impact,  $\phi$  is the azimuthal angle and  $\theta$  is the polar angle respectively. Since, there is more than one layer, a choice of the set of points per layer also makes a difference in this process.

- *Pattern Recognition or Trajectory Building*: The Kalman filter algorithm is used to construct the tracks, based on the combinatorial approach.
- *Ambiguity Resolution*: To prevent counting the tracks twice, the fraction of tracks shared between two trajectories is estimated, and this step is carried out two times and the track with the highest  $\chi^2$  value is discarded.
- *Final Track Fit*: At least 8 hits and a hit missing not more than 1 layer with  $p_T > 0.8 \text{ GeV}/c$  are considered as a reconstructed track and it should match with at least 50% of the tracks reconstructed from the simulations.

As part of the HIN-12-017 [6] analysis, the collections chosen to measure the charged particles also accounted for misreconstructed tracks, fake tracks and trigger turn on possibilities as well.

### 2.1.6.2 Vertex Reconstruction

Based on the reconstructed tracks, the next step is to construct the vertices. Vertices are of two types, *primary* and *secondary* vertices. The primary vertex corresponds to the collision point from where all the particles have originated, and the secondary vertex is the point where a particle decays into other particles. If there is no pile up in the event, i.e. not more than one pPb collision per bunch crossing is responsible for generating the tracks, then there would be only one primary vertex.

The process of vertex reconstruction is done in two steps, *Vertex finding* and *Vertex fitting*. Vertex finding is accomplished by a few standard algorithms like Kalman filter

(KVF), Adaptive Vertex Fitter(AVF) and Trimmed Vertex Fitter(TKF)

Vertex fitting is based on the best estimate of the vertex parameters; position, covariance matrix, track parameters, and other statistical factors like  $\chi^2$ , ndof, track weights, *etc*

## 2.2 CMS Computing Model

The CMS grid computing facility is a part of the World LHC Computing Grid (WLCG) built to provide computing facilities for all experiments at LHC and is based on a hierarchial *Tier* model. The largest computing facility, Tier-0 is at CERN and at Budapest, Hungary with approximately 200,000 cores and a few hundred petabytes of storage space. The next smaller tier is referred to as Tier-1, is in 7 countries, and linked to the Tier-0. Further down the tier hierarchy, there are Tier-2s in 40 countries. The computing capacities in terms of cores and the storage space decreases from Tier-0 to Tier-2. The job submission infrastructure is set up such that the data sets can reside anywhere, while the jobs can run anywhere in the world. Once an analyzer/physicist submits a set of jobs, *crab3*, a job submission framework takes care of job submission, scheduling the jobs to run and the *xrootd* system takes care locating the data sets required for the jobs and fetching them when the jobs begin to run. All this system is completely automated, so that the analyzer works only on using the CMS Software Application Programming Interface (CMSSW API).

CMSSW API is a framework developed by a dedicated team to interface with the CMS Detector to access the datasets processed at different tiers. The same framework is tightly integrated to work with Monte Carlo programs as well. The entire software stack referred to as the CERN Virtual Machine File System (CVMFS), that the analyzer uses is maintained centrally and mounted at all the Tiers. Results for this research were possible because of the tight integration between CMSSW API,

Monte Carlo simulation framework, ROOT and the Les Houches Accord Parton Distribution Function (LHAPDF) framework and the jobs were run at the Vanderbilt, ACCRE Tier-2 high performance computing cluster.

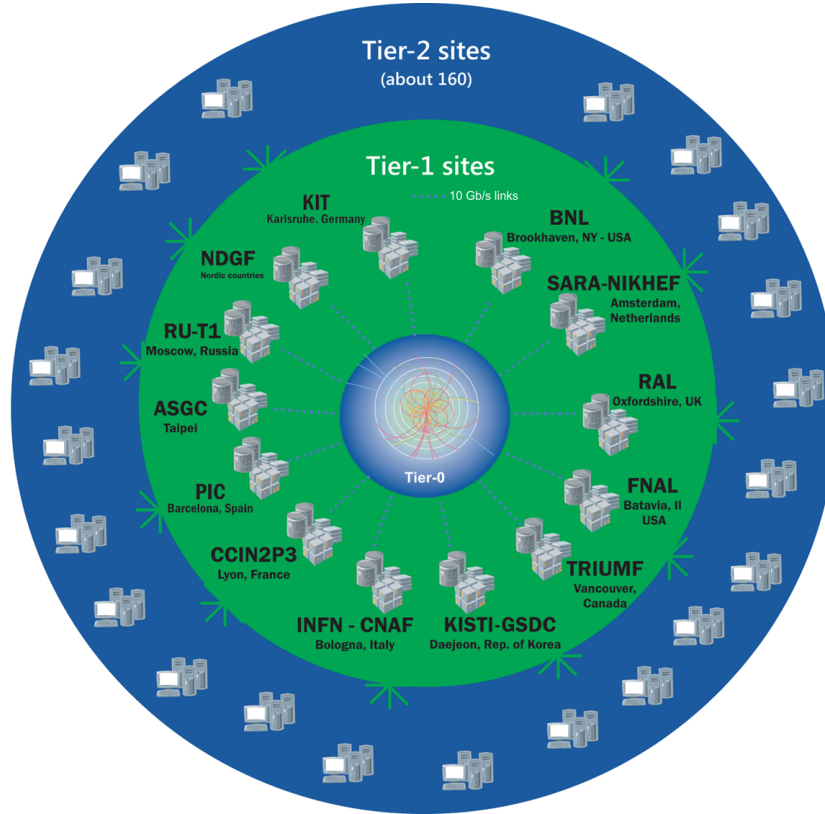


Figure 2.6: Schematic for the CERN Grid Computing System. Moving radially outward, the storage capacity and the available number of cores for processing per Tier becomes smaller [12].

### 2.3 CMS Module Framework

CMS Analyzer code is set up to work as a series of interlinked modules 2.7, where the flow of information, in the form of various data structures are passed via modules. Each module can work independently and the results can be chained into different root files. The objects from collections can be accessed by the analyzer code and passed to different modules as per the analysis requirements.

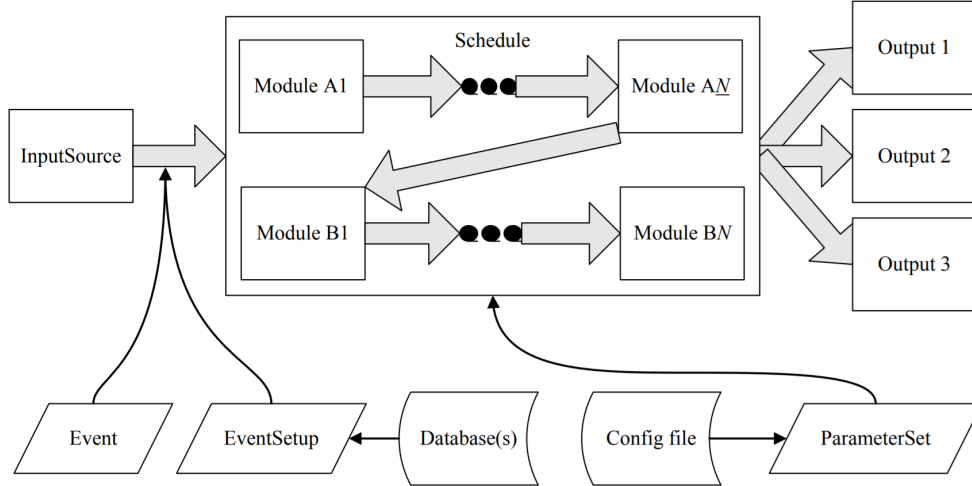


Figure 2.7: Modules within the CMS Application Framework [13]

## 2.4 Data Formats : RAW, RECO and AOD

The CMS detector has a bandwidth of about 6Gbps, transferring data from the detector during the run to the Tier-0, the central computing facility at CERN for real time processing based on L1 triggers and also post processing based on several algorithms, say for example Tracking Algorithms.

1. **RAW Data Sets:** RAW data is the data from detector directly dumped into Tier-0 and is *not used by analysis*, however is stored on tape for future use. It is the largest data set from which the rest of the data formats are generated.
2. **RECO Data Sets :** Reconstructed Data Sets (RECO) are the processed datasets from RAW, which can also be used by the analyzers, however, they are currently replaced by a more leaner data format called AOD. The RECO data sets have information in accessible format referring to a *collection*, for use in the CMSSW framework. This format is generated after running algorithms on the RAW data and packing them into collections for analysis, for example, the pixel hits collection from the tracking detector. The RECO data sets can be processed again, also called re-RECO datasets depending on the requirements

from Physics Analysis Groups (PAG).

3. **AOD Data Sets** : Analysis Object Data (AOD) is the format currently in use by heavy ion analyzers as the RECO dataset use has been deprecated after the 2013 Run. Due to the larger processing time and presence of unwanted collections occupying more space. AOD is a stripped down version of RECO or re-RECO data sets and is approximately 20% of the RECO data set.

The time it takes to process a collection offline depends on the size of the data sets, the algorithms chosen and the number of modules that needs to be processed per event. Since searching for particles is like looking for a needle in a hay stack, more data should be available for the analyzer to hunt for an important phenomena. And since, the detectors do not collect data the entire time and the rate of data acquisition is directly proportional to the trigger rate, the requirement for collecting more data has increased and this created the need for leaner data formats occupying less space that can be processed in the shortest possible time. It should be noted that the RECO data sets take a much larger time to process compared to the AOD data sets.

## 2.5 CMS Data Acquisition Workflows

Before the run begins, a simulation of the expected amount of data with the defined settings is done and is referred to as *Replays*. Replays make sure, the software works and the processing time and the generated output is within expected limits. This is a concerted effort by the Physics Interest Groups (PInG) and the Physics Analysis Groups (PAG).

Once the CMS detector goes online, the data from the detector is transferred



as the data is flowing from the detector and into the Tier-0 computing center

- (a) CAF : This system handles mission critical activities like the alignment, calibration and detector/trigger commissioning from the Data Acquisition System (DAQ). The goal of this system is to ensure that the quality of data with detector related parameters is as expected from the Conditions Database (CondDB) after the *Express reconstruction* is completed.
- (b) *Express Reconstruction* : The transferred data from the detector is processed in real time in this block.
- (c) *Prompt Reconstruction* : This phase is executed at the Tier-0. The express streams are processed inside a loop known as Prompt Calibration Loop(PCL), where the information from the calibrations data base is used to run this step and it should be finished within 48 hours.
- (d) *Storage and Distribution*: The Offline Reconstruction Condition DB Online System (ORCON), Online Master Database System (OMDS), Offline Reconstruction Condition DB Offline (ORCOFF) are read by the network and updated about the alignment and calibration info.
- (e) *High Level Trigger(HLT)*: The purpose of a trigger is to filter a specific set of events based on the user specified constraints. This is the first trigger through which all events get filtered immediately after the collision in real time. The purpose of this trigger is to reduce the rate at which event data is collected; should it not be the case, the storage space would be inadequate.
- (f) *ORCON, ORCOF*: ORCON stands for Offline Reconstruction Condition DB Online System and

- (g) *Alignment and Calibration* : For undertaking this step, dedicated *Al-CaReco* samples are taken. Depending on the nature of workflow i.e. for cases where the constants change rapidly, the online version and for more complex workflows, the offline versions of the software are run on the High Level Trigger (HLT) .
- (h) *Commissioning and Physics DQM*:
- (i) *Tier-0* : Tier-0 is the CERN's central computing facility based on CERN Geneva and from Budapest Hungary. The entire data from the detector flows into the EOS low latency storage system. From here the Tier-0 begins processing the data and it should all finish in less than 48 hours as was done during the *Replays*. Replays are simulation runs done in a real world environment to make sure the entire system is working as expected before the real time data flows in.

It should be noted that, despite the post processing done on the RECO data sets, validations are run on the data set to ensure the information contained is accurate and matches with the DAQ's Alignment and Calibration database. This information is made available to the analyzers after the post processing is completed.

## 2.6 Event Display

A visualization of a real event is shown in the Fig. 2.9. The tracks can be seen clearly seen as yellow lines in both pictures.

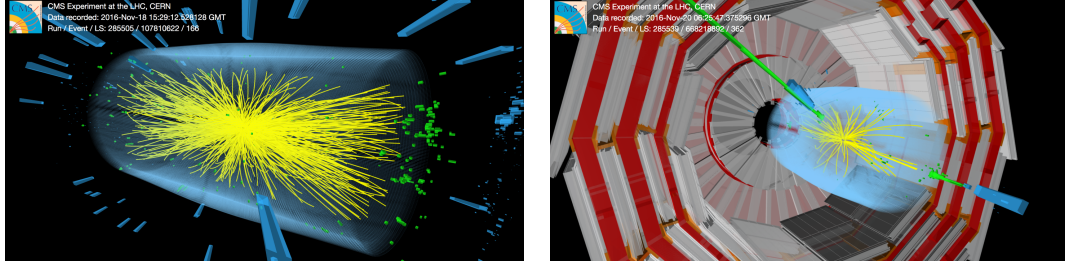


Figure 2.9: Event Display based on the data collected in November 2016 for pPb collisions [15, 16]

## 2.7 Summary

- (a) Large Hadron Collider has five interaction points to collide particles; CMS, ALICE, ATLAS, LHCb and LHCf detectors.
- (b) Although the CMS detector has a total  $4\pi$  pseudorapidity coverage, the different parts of the detector cover a part of this coverage, hence the physics that happens in different pseudorapidity range is studied based on the signals processed at the chosen detector.
- (c) Description of the CMS subdetectors: ECAL, HCAL, Forward and Tracking Detectors.

## Chapter 3

### Measurement of Nuclear Modification Factor $R_{pPb}$

In this chapter, the method that was used to obtain the nuclear modification factor as cited in [6] is described. The mathematical formula for nuclear modification factor for pPb collisions:

$$R_{pPb}(p_T, |\eta|, \sqrt{s_{NN}}) = \frac{d^3 N_{pPb}/N_{\text{evt}} dp^3}{\langle N_{\text{coll}} \rangle d^3 N'_{pp}/N'_{\text{evt}} dp^3} \equiv \frac{\text{QCD Medium}}{\text{QCD Vacuum}}$$

where, the numerator refers to the spectra normalized to the total number of events in a pPb collision and the same quantity in the denominator is for a pp collision. The factor  $\langle N_{\text{coll}} \rangle$ , is obtained from the *Glauber Model* and has a value of about 6.9. It stands for the mean number of binary collisions i.e. a single proton can strike more than one nucleon in the lead nucleus; in order to account for that, the *Glauber Model* simulation was done to estimate the number of nucleons wounded in the Pb nucleus by a single incoming proton.

Qualitatively, this quantity helps understand the influence of the yields of hadrons because of a lot of parton level scattering in a cold nuclear medium compared to that of a proton-proton collision in vacuum at same energy.  $R_{pPb}$  depends on the center of mass energy  $\sqrt{s}$ , momentum range  $p_T$ , in which the spectra is obtained. It also depends on the pseudorapidity interval  $|\eta|$  within which the spectra is obtained experimentally or via simulations and doesn't depend on the number of events ( $N_{\text{evt}}$ ) used in the numerator or the denominator as they are taken into account while doing spectra normalization.

### 3.1 Method and Data Sets

During the time of HIN-12-017 analysis, pp data at  $\sqrt{s} = 5.02$  TeV was not available. Without the pp reference, the nuclear modification factor couldn't be estimated. Hence, the *direct interpolation* approach was taken to estimate the reference spectrum at  $\sqrt{s_{NN}} = 5.02$  TeV, based on the data sets published in the previous years and comparing with Pythia simulations. Two methods of *direct interpolation* were applied for cross-checking purposes, since results from simulations alone wouldn't be a reliable estimate and it was found that Z2 Tune based on Pythia v6 gives a better estimate compared to ProQ2 Tune based on Pythia v8.

Charged particle spectra from the CMS Collaboration [43, 57] at  $\sqrt{s} = 0.9, 2.76, 7$  TeV were used and as a cross-check, similar results from the CDF Collaboration at  $\sqrt{s} = 0.63, 1.8, 1.96$  are also used. For the CMS spectra, the yields of both positively and negatively charged particle spectra from non-single diffractive collision events are chosen, and the integrated luminosity was obtained to convert to cross-sections and the inelastic cross-sections were used from the CDF Collaboration.

#### 3.1.1 Spectra of All Charged Particles: 2013 pPb and 2015 pp data sets

The spectra of charged particles is a the key observable that's obtained from the detector and is a function of the transverse momenta  $p_T$  and the pseudo-rapidity  $\eta$  for this analysis. It is given by the formula  $\frac{d^2N}{dp_T d\eta}$ . Based on the data from the CMS Heavy Ion Run 2013 and in the mid rapidity range ( $|\eta| < 1$ ), it was published in [6].

To obtain the total spectra of the charged particles, the spectra from the individual triggers are combined and normalized with the scaling factor. Scaling factor is the number that represents the rate in Hz at which the data is collected by the triggers. Since the production of particles is not uniform at all  $p_T$  intervals, to accumulate for more statistics at higher  $p_T$ , different triggers are designed with varying rates.

From the Heavy Ion 2013 UPC data set, spectra from three triggers were combined to generate the combined spectra. When extracting the information from the triggered data sets, one should make sure, the *turn on* curves are properly accounted for during summation. Turn on curves are the points where a trigger starts. For analysis purposes, one has to make sure that trigger is fully efficient before reading the data.

In order to combine the spectra, the following recipe was used since triggers have to be normalized with the corresponding rates.

The pp reference data used for the analysis in [6] is based on interpolation of data sets from older data. However with the Run 2015, pp data at the same center of mass energy was available, but with four different triggers.

Based on the methods described above, the spectra can be obtained for positively and negatively charged particles from 2013 pPb and 2015 pp data sets.

### 3.1.1.1 Combination of Spectra from different Data Sets

$p_T$ Range	Dataset
$p_T < 20$	Minimum Bias
$20 < p_T < 26$	FullTrack18
$26 < p_T < 36$	FullTrack24
$36 < p_T < 47$	FullTrack34
$47 < p_T < 55$	FullTrack45
$p_T > 55$	FullTrack53

2015 pp Reference data set

$p_T$ Range	Dataset
$p_T < 14$	Minimum Bias
$14 < p_T < 22$	FullTrack12
$22 < p_T < 32$	FullTrack20
$p_T > 32$	FullTrack30

2013 pPb data set

Published results for the combined spectra from 2013 pPb UPC MinBias and Track Triggered Data sets.

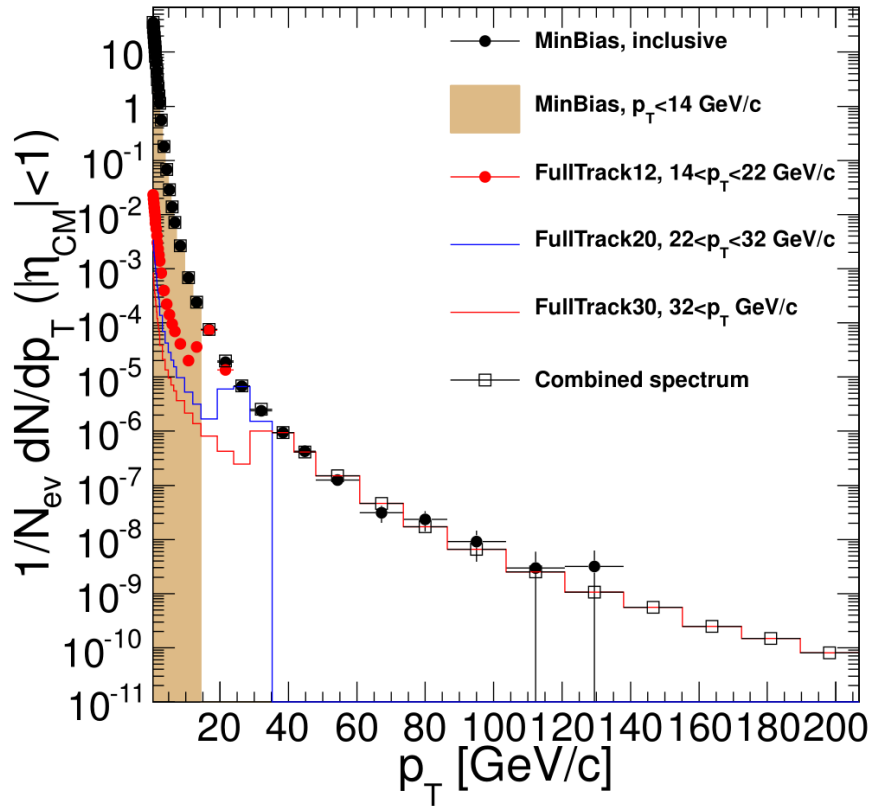


Figure 3.1: Combined spectra of all charged particles for 2013 pPb data [6]

Published results for the combined spectra from 2015 pp MinBias and Track

Triggered Data sets.

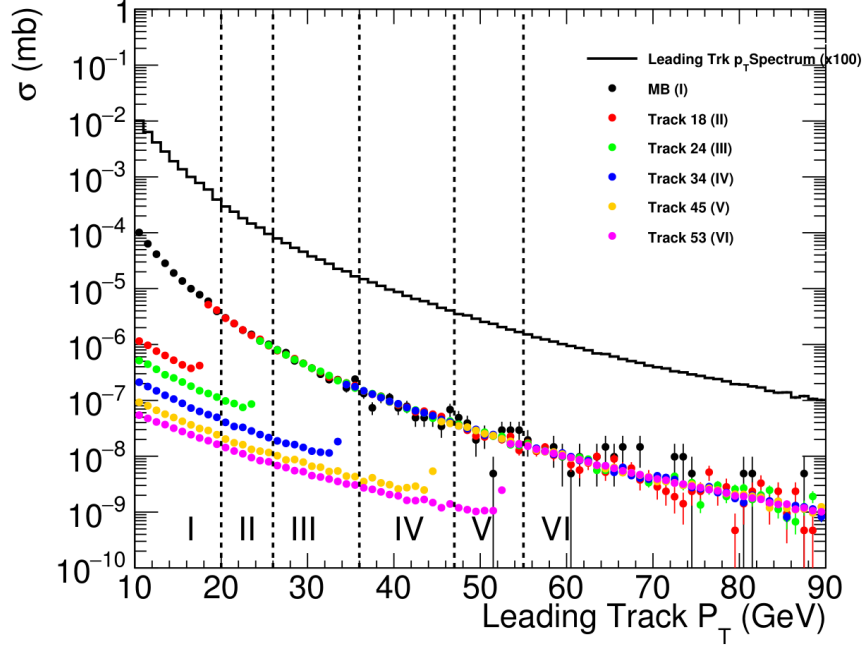


Figure 3.2: Combined spectra of all charged particles for 2015 pPb data [4]

$$\text{Spectra}[\text{Type}] = \frac{dN_{\text{ch}}}{dp_T}[\text{Type}]$$

[*Type*] can be Minimum Bias or any of the Track triggers as exemplified below.

$$\text{Spectra}[\text{Combined}] = \text{Spectra}[\text{MB}] + \text{Spectra}[\text{Track12}] + \text{Spectra}[\text{Track20}] + \text{Spectra}[\text{Track30}].$$

To obtain the MB, Track12, Track20, Track30 spectra, the following recipe is applied. A buffer of 2GeV/c is considered after the trigger turn on happens, when the data taking becomes maximally efficient and flows into the next trig-

ger. Hence the range for  $p_T$  for the leading track is increased by two units.

$$\begin{aligned} \text{Spectra}[\text{MB}] &= \frac{dN_{\text{ch}}}{dp_T}(\text{MB, leading track } p_T < 14 \text{ GeV}/c)/N_{\text{MB}} \\ \text{Spectra}[\text{Track12}] &= \frac{dN_{\text{ch}}}{dp_T}(\text{Track12, leading track } 14 < p_T < 22 \text{ GeV}/c)/N_{\text{Track12}} \\ \text{Spectra}[\text{Track20}] &= \frac{dN_{\text{ch}}}{dp_T}(\text{Track20, leading track } 22 < p_T < 32 \text{ GeV}/c)/N_{\text{Track20}} \\ \text{Spectra}[\text{Track30}] &= \frac{dN_{\text{ch}}}{dp_T}(\text{Track30, leading track } p_T > 32 \text{ GeV}/c)/N_{\text{Track30}} \end{aligned}$$

$$N_{\text{MB}} \equiv N_{\text{MB, all events}}$$

$$N_{\text{Track12}} \equiv N_{\text{MB}} N_{\text{Track12, } 14 < p_T < 22} / N_{\text{MB, } 14 < p_T < 22}$$

$$N_{\text{Track20}} \equiv N_{\text{Track20}} N_{\text{Track20, } 22 < p_T < 32} / N_{\text{Track12, } 22 < p_T < 32}$$

$$N_{\text{Track30}} \equiv N_{\text{Track20}} N_{\text{Track30, } p_T > 32} / N_{\text{Track20, } p_T > 32}$$

Applying the same recipe for the pp reference data

$$\begin{aligned} \text{Spectra}[\text{MB}] &= \frac{dN_{\text{ch}}}{dp_T}(\text{MB, leading track } p_T < 20 \text{ GeV}/c)/N_{\text{MB}} \\ \text{Spectra}[\text{Track18}] &= \frac{dN_{\text{ch}}}{dp_T}(\text{Track18, leading track } 20 < p_T < 26 \text{ GeV}/c)/N_{\text{Track12}} \\ \text{Spectra}[\text{Track24}] &= \frac{dN_{\text{ch}}}{dp_T}(\text{Track20, leading track } 26 < p_T < 32 \text{ GeV}/c)/N_{\text{Track20}} \\ \text{Spectra}[\text{Track24}] &= \frac{dN_{\text{ch}}}{dp_T}(\text{Track20, leading track } 22 < p_T < 32 \text{ GeV}/c)/N_{\text{Track20}} \\ \text{Spectra}[\text{Track53}] &= \frac{dN_{\text{ch}}}{dp_T}(\text{Track30, leading track } p_T > 32 \text{ GeV}/c)/N_{\text{Track30}} \end{aligned}$$

$$N_{\text{MB}} \equiv N_{\text{MB, all events}}$$

$$N_{\text{Track12}} \equiv N_{\text{MB}} N_{\text{Track12, } 14 < p_T < 22} / N_{\text{MB, } 14 < p_T < 22}$$

$$N_{\text{Track20}} \equiv N_{\text{Track20}} N_{\text{Track20, } 22 < p_T < 32} / N_{\text{Track12, } 22 < p_T < 32}$$

$$N_{\text{Track30}} \equiv N_{\text{Track20}} N_{\text{Track30, } p_T > 32} / N_{\text{Track20, } p_T > 32}$$

### 3.2 Data Driven Analysis: Positive and Negative Charged Particles

In this section, the data-driven analysis for this study is presented for both types of charged particles. Primarily, the spectra of positively and negatively charged particles is obtained based on the methods developed in the published analysis [6] for spectra combination with similar cuts. The major difference being, the results are presented for 2013 pPb data sets as well as 2015 pp data sets, which were unavailable prior to this analysis at  $\sqrt{s_{NN}} = 5.02$  TeV.

The algorithm applied to obtain the positive and negative charged particle spectra from track data generated from the CMS detector.

```

Loop(Events)
  if (vertex cuts passed)
    Loop(Tracks from Collection)
      if (track cuts passed)
        extract[track( $p_T$ ), charge]

```

### 3.3 Summary

- Nuclear modification factor  $R_{AA}$  helps understand the differences in QCD in a nuclear medium versus QCD in vacuum.
- Spectra in both pPb and pp collision systems are obtained based on track triggered datasets, because of the smaller probability in obtaining a hadron at high  $p_T$ , triggered data sets are used in 3 or more intervals to obtain the spectra of positive, negative and all charged particles.
- Nuclear modification is calculated by taking the ratio of the spectra by including the factor  $\langle N_{\text{coll}} \rangle$  to account for the equivalent number of proton-proton collisions as a single proton can strike more than one proton on its way into the lead nucleus.

## Chapter 4

### Monte Carlo Simulations

Monte Carlo simulators are event generators which have a parameter space within which the simulator can be compared with experimental data. One of the ways to simulate a proton-proton collision or a proton-lead collision at a very high center of mass energy is to perform a Monte-Carlo simulation with different Parton Distribution Function(PDF) sets and then compare with experimental data. For the purpose of this thesis, the event generator Pythia was used, owing to its success in describing LHC data and also being a key input to various other event generators.

A schematic for how complex a proton-proton collision can be given in Fig. 4.1, and for the case of a proton-lead collision the situation is expected to be more complicated. For the case of this study, only the PDF distributions were changed, and the rest of the parameters remain the same, as defined by Tune 4C.

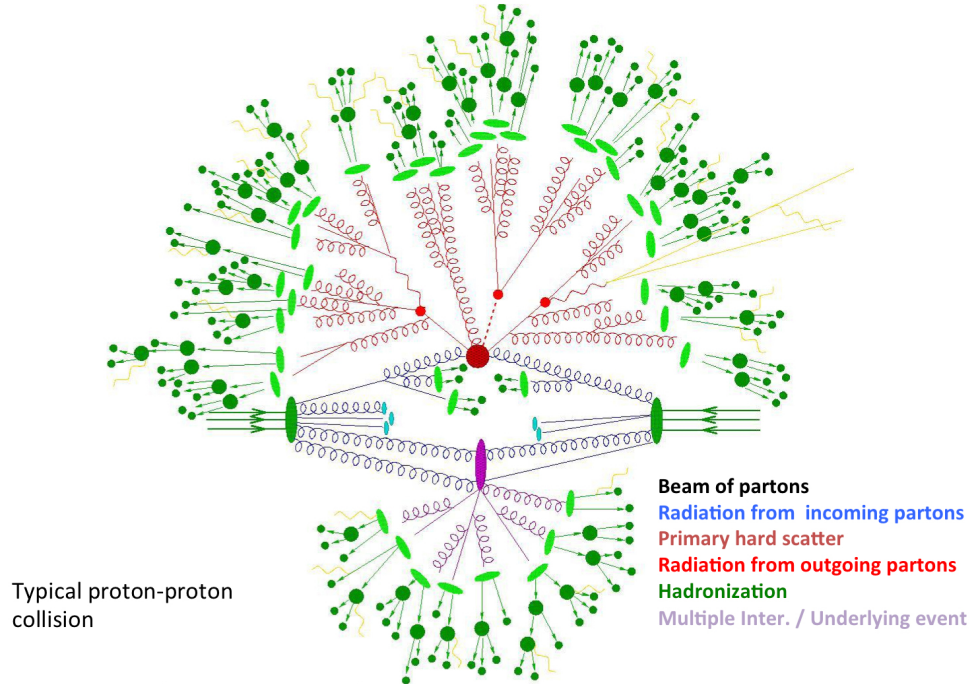


Figure 4.1: Proton-Proton collision at a very large energy, where several hard-scatterings take place before the onset of hadronization [17]

#### 4.1 Event Generator: Pythia

Pythia is an event generator developed by Bo Andersson at Lünd University. Initially, it was programmed in Fortran 77 by the physicist Torbjörn Sjöstrand from the same university in [58] and was later converted to C++ in [18]. The core of the program was initially referred to as JETSET. In the year 2004, the conversion from Fortran 77 to C++ was begun and released in 2007 as a stable release with the version latest version, Pythia 8.2 [59].

Some of the key features in Pythia include :

- (a) Describes physics phenomena at a large center of mass collision energy range,  $10\text{GeV} < \sqrt{s} < 100\text{TeV}$

- (b) Various switches for the user to control the type of participating partons like hard-process, soft-process switches for QCD processes.
- (c) Integrated with Les Houches Accord Parton Distribution Function (LHAPDF) library, so that simulation specific PDF distributions can be added.
- (d) Availability of several inbuilt tunes [60, 61, 25] to study different physics phenomena at different collision energy range. Although Tune 4C [62] is used for the analysis, it is recommended by the MC groups to make the PDF to be compatible with the Tune 4C of choice or develop a new Tune, which requires validation from the Monte Carlo experts.
- (e) Can describe momentum fraction of the parton starting from a very low value of  $10^{-8}$  and upward until unity.
- (f) Has provision to turn on/off the following switches at parton level collisions:
  - i. Initial State Radiation (ISR) : The production of partons before the parton from one nucleon participate in a hard scattering with a parton from another nucleon
  - ii. Multiple Parton Scattering (MPI) : Partons scattering off each other beyond the very first hard scattering processes from the cascade of partons produced.
  - iii. Final State Radiation (FSR) : The point where partons fragment further before the onset of hadronization

The block diagram 4.2 explains the functional aspect of Pythia in the latest version. The core functionality for the most part is the same as the fortran version of the program Pythia 6 [58].

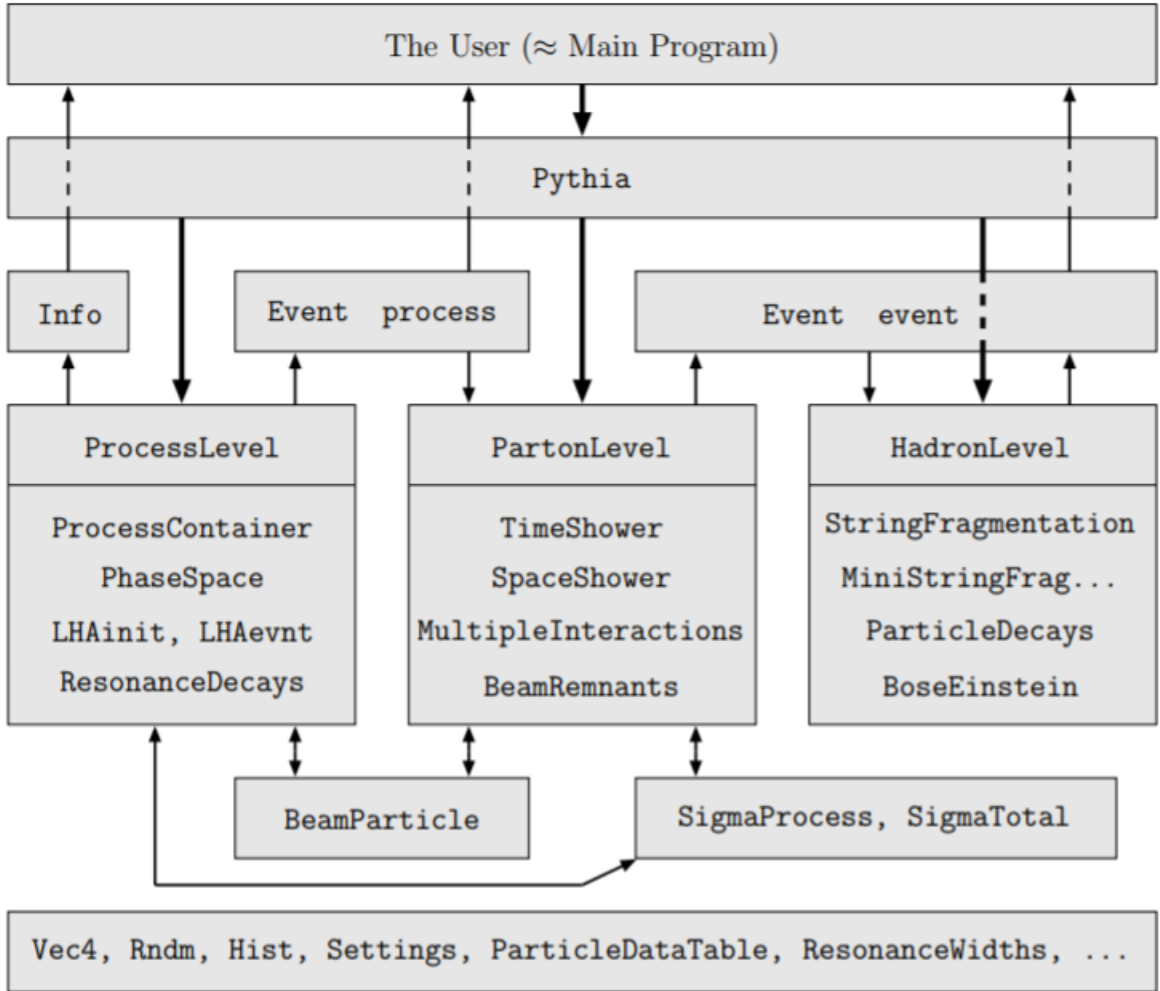


Figure 4.2: The relationship between the main classes in Pythia 8. The thick arrows show the flow of commands to carry out different physics tasks, whereas the thinner arrows show the flow of information between the tasks. The bottom box contains common utilities that may be used anywhere [18].

The heart of the program is based on the hard-scattering leading-order cross-section formulas at the parton level. The hard-scattering results are implemented only for  $2 \rightarrow 2$  scatterings i.e. a parton colliding with another parton to yield another pair of partons of different types. Hard-scattering refers to the cross-sections valid only in the context of pQCD i.e the  $2 \rightarrow 2$  scatterings should exchange a momentum greater than 1GeV and where factorization is valid. Within QCD, the LO Cross-sections are calculated based on the results

in the Table. 4.1.

The most important feature of the program is the inbuilt hadronization model and with a wide range of values for  $x$  and  $Q^2$  as it is being validated by several experimental groups. *Hadronization* refers to the process in which the partons after undergoing the hard-scattering processes at the partonic level, after multiple parton scattering, where the partons produced in a cascade undergo scatterings several times beyond which they get converted to colorless final state hadrons. These hadrons in turn decay to more stable particles.

The functional purpose of each of the subsystem is explained below. *ProcessLevel*, *PartonLevel*, *HadronLevel*, *BeamParticle*, *SigmaProcess*, *SigmaTotal* are the some of the core classes inside Pythia, which have settings to modify them during initialization or within the developer's code as well. It should be noted that, the classes are dependent on one another.

- (a) ***BeamParticle*** : The incoming particle beam PDG ID, which can be a proton, neutron or other particles based on the physics to be studied. For this study, the proton is used. Pythia provides a lot of options, even particles like electron, positron, pions and composite particles like Pomeron could also be initialized.
- (b) ***ProcessLevel***: A choice of possibilities, for the type of hard scattering as listed in table 4.1.
- (c) ***PartonLevel***: In this section there are three important possibilities, Multiple Parton Scattering(MPI), Initial State Radiation (ISR) and Final State Radiation (FSR) are included, which can influence the spectra of the outgoing particles.

- (d) ***HadronLevel***: Has options to control hadronization and parameters to control the string model parameters just after parton showering has completed along with any strong interaction based decays, which generate only hadrons.

The options described above are only some of the basic ones which are required to run an event, there are lot more options which are set up and must not be modified in general, because they are dependent on one another and can give results that may not be interpreted.

And, there are four kinds of settings: *Flag*, a boolean for turning things on and off, *Mode*, stored as an integer, *Param*, stored as a double and *Word*, stored as a double, where double refers to the data type in computer science jargon. These are intrinsic to Pythia, are not separate data structures, but are configured by the developers of Pythia for ease of use. The basic programming recipe for Pythia is as follows:

```
Load (Configuration File)
Loop (Events[n])
    Set Parameters [rapidity range]
    Read Outgoing Particle Info
        [momentum, pdgId, momentum fraction]
```

Process Switch	Explanation
HardQCD:qq2qq	Two incoming quarks scatter off to produce the incoming quarks of the same type.
HardQCD:gg2qqbar	Two incoming gluons produce a quark and an anti-quark
HardQCD:gg2gg	Two incoming gluons scatter off to produce two gluons
HardQCD:qqbar2gg	A quark and anti-quark annihilate to produce two gluons
HardQCD:qq2qg	An incoming quark/anti-quark and a gluon scatter off to produce a quark/anti-quark and a gluon
HardQCD:all	For all the hard scatterings listed above

PROCESS	$d\hat{\sigma}/d\phi_2$ [19]	FIGURES
$q_i q_j \rightarrow q_i q_j$	$\frac{1}{2\hat{s}} \frac{4}{9} \frac{\hat{s}^2 + \hat{u}^2}{\hat{t}^2}$	4.5
$q_i q_i \rightarrow q_i q_i$	$\frac{1}{2\hat{s}} \left[ \frac{4}{9} \left( \frac{\hat{s}^2 + \hat{u}^2}{\hat{t}^2} + \frac{\hat{s}^2 + \hat{t}^2}{\hat{u}^2} \right) - \frac{8}{27} \frac{\hat{s}^2}{\hat{u}\hat{t}} \right]$	4.4
$q_i \bar{q}_i \rightarrow q_j \bar{q}_j$	$\frac{1}{\hat{s}} \frac{4}{9} \frac{\hat{t}^2 + \hat{u}^2}{\hat{s}^2}$	4.3
$q_i \bar{q}_i \rightarrow q_i \bar{q}_i$	$\frac{1}{\hat{s}} \left[ \frac{4}{9} \left( \frac{\hat{s}^2 + \hat{u}^2}{\hat{t}^2} + \frac{\hat{t}^2 + \hat{u}^2}{\hat{s}^2} \right) - \frac{8}{27} \frac{\hat{u}^2}{\hat{s}\hat{t}} \right]$	4.6
$q_i \bar{q}_i \rightarrow gg$	$\frac{1}{2} \frac{1}{\hat{s}} \left[ \frac{32}{27} \frac{\hat{t}^2 + \hat{u}^2}{\hat{t}\hat{u}} - \frac{8}{3} \frac{\hat{t}^2 + \hat{u}^2}{\hat{s}^2} \right]$	4.7
$gg \rightarrow q_i \bar{q}_i$	$\frac{1}{2\hat{s}} \left[ \frac{1}{6} \frac{\hat{t}^2 + \hat{u}^2}{\hat{t}\hat{u}} - \frac{3}{8} \frac{\hat{t}^2 + \hat{u}^2}{\hat{s}^2} \right]$	4.9
$gq_i \rightarrow gq_i$	$\frac{1}{2\hat{s}} \left[ -\frac{4}{9} \frac{\hat{s}^2 + \hat{u}^2}{\hat{s}\hat{u}} + \frac{\hat{u}^2 + \hat{s}^2}{\hat{t}^2} \right]$	4.8
$gg \rightarrow gg$	$\frac{1}{2} \frac{1}{2\hat{s}} \frac{9}{2} \left( 3 - \frac{\hat{t}\hat{u}}{\hat{s}^2} - \frac{\hat{s}\hat{u}}{\hat{t}^2} - \frac{\hat{s}\hat{t}}{\hat{u}^2} \right)$	4.10

Using the following selection of switches in Pythia 8, the type of hard-scattering processes can be changed. Although experimentally, all processes account for the production of hadrons, through these options, a certain set of possibilities can be studied exclusively. The Fig. 4.2 is produced based on the *HardQCD:all* option to compare with experiment. And the corresponding cross-sections for the Feynman diagrams [4.6, 4.7, 4.8, 4.9, 4.10, 4.5, 4.4, 4.3] used to compute the hard-scattering cross-sections contained in Pythia are listed in the table 4.1

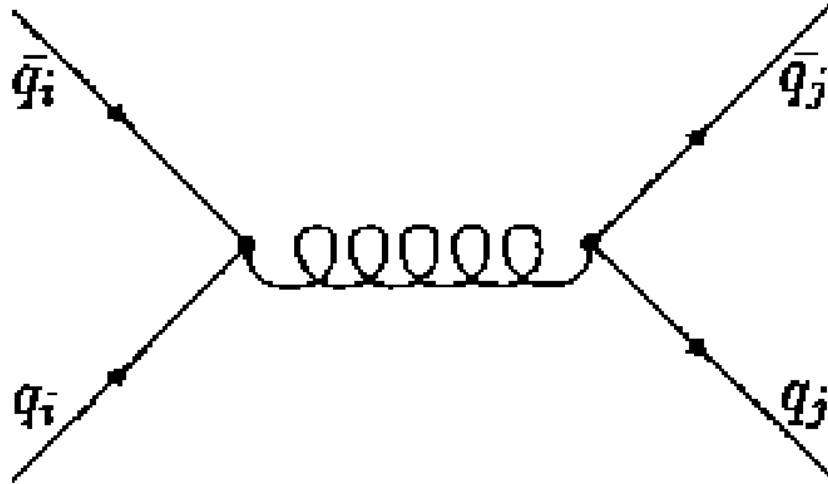


Figure 4.3: The lowest tree level diagrams contributing to  $q_i \bar{q}_i \rightarrow q_j \bar{q}_j$ ,  $i \neq j$  [19]

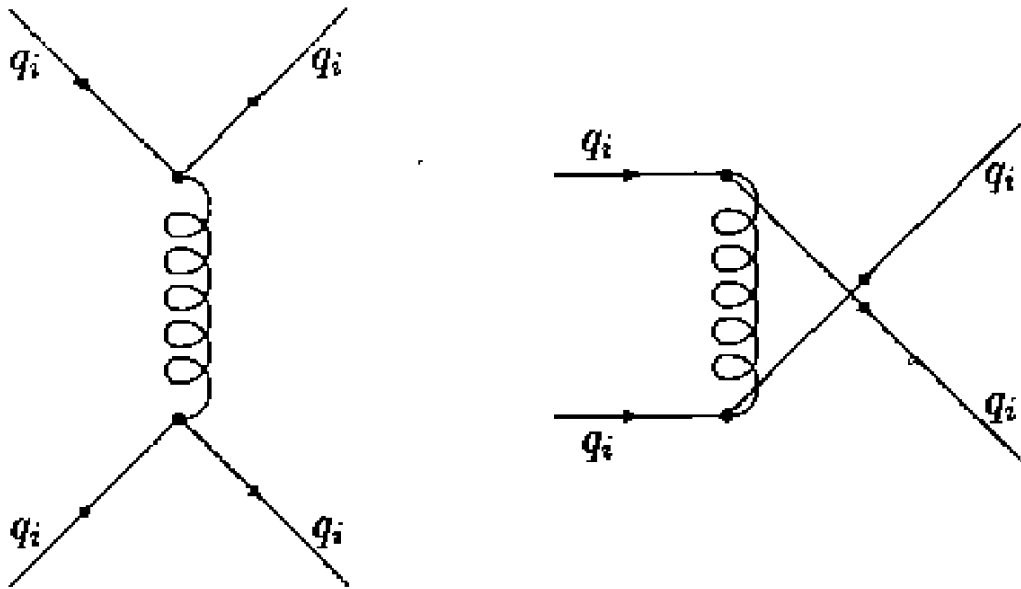


Figure 4.4: The lowest tree level diagrams contributing to  $q_i q_i \rightarrow q_i q_i$  [19]

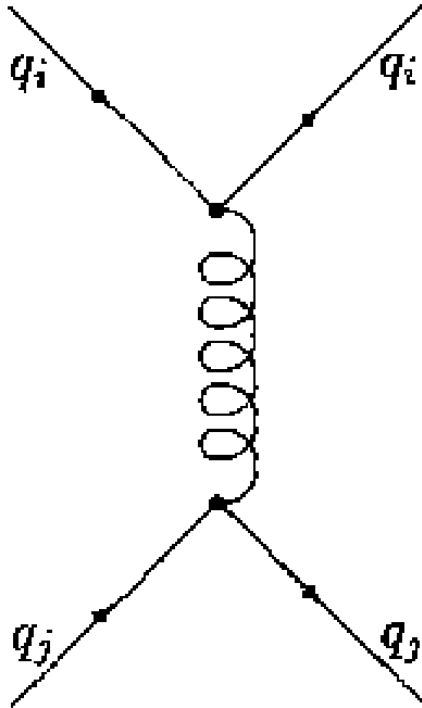


Figure 4.5: The lowest tree level diagrams contributing to  $q_i q_j \rightarrow q_i q_j$ ,  $i \neq j$  [19]

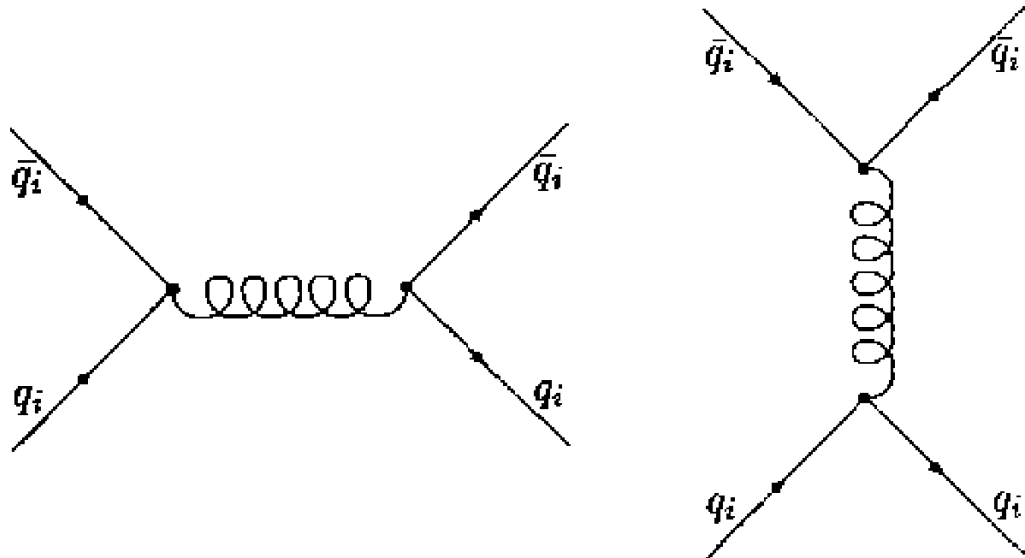


Figure 4.6: The lowest tree level diagrams contributing to  $q_i \bar{q}_i \rightarrow q_i \bar{q}_i$  [19]

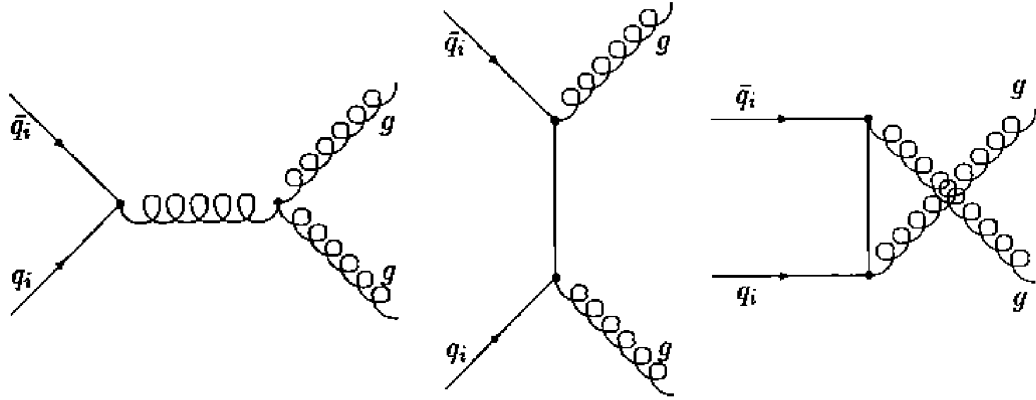


Figure 4.7: The lowest tree level diagrams contributing to  $q_i \bar{q}_i \rightarrow gg$  [19]

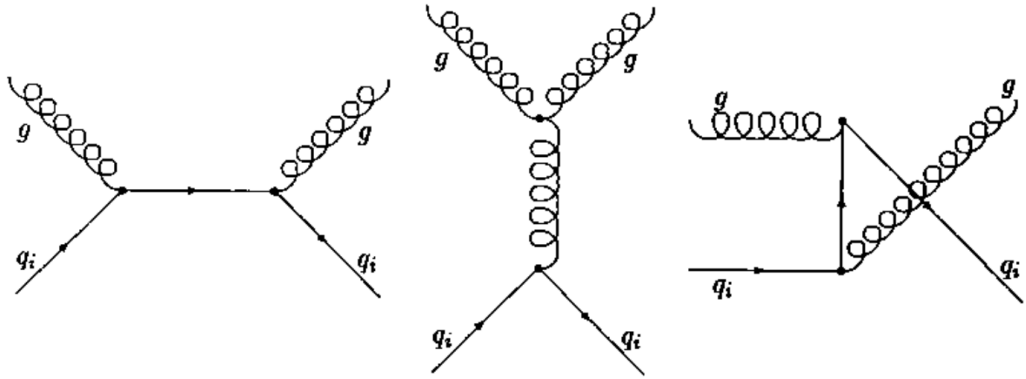


Figure 4.8: The lowest tree level diagrams contributing to  $q_i g \rightarrow q_i g$  [19]

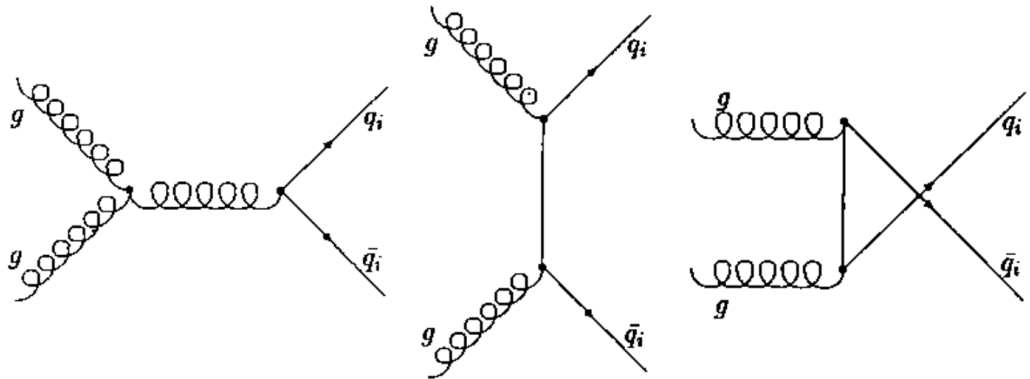


Figure 4.9: The lowest tree level diagrams contributing to  $gg \rightarrow q_i \bar{q}_i$  [19]

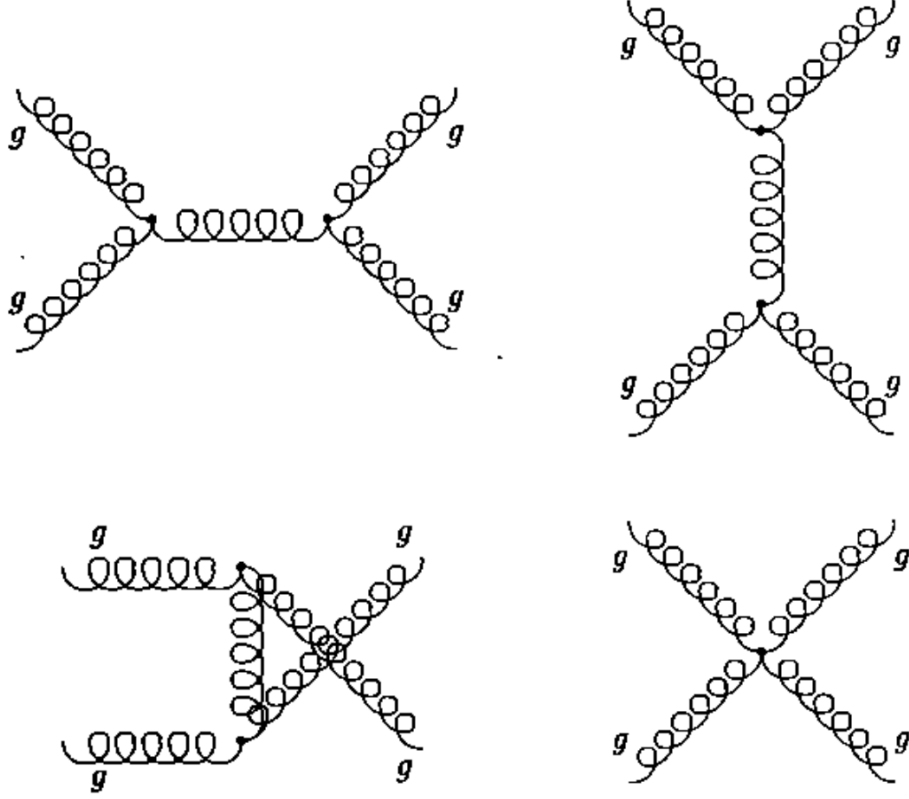


Figure 4.10: The lowest tree level diagrams contributing to  $gg \rightarrow gg$  [19]

$$\sigma(A + A \rightarrow X + h) \approx \sum_{i,j} \int_0^1 dx_1 dx_2 x_1 f_i(x_1, Q^2) \otimes x_2 f_j(x_2, Q^2) \frac{d\hat{\sigma}_{ab}}{dt} D_i^h(z, \mu^2)$$

$\sigma(A + A \rightarrow X + h)$  is the final cross-section of the inclusive hadrons simulated based on the chosen PDF distributions from parton-parton hard-scatterings. Here  $\hat{\sigma}_{ab}$  is the parton level  $2 \rightarrow 2$  cross-section,  $x_1, x_2$  are the momentum fraction of the parton from the beam and target respectively,  $Q^2$  is the four momentum transferred between the partons,  $f_i(x_1, Q^2), f_j(x_1, Q^2)$  are the parton distribution functions of the  $i^{\text{th}}$  and the  $j^{\text{th}}$  partonic species from the beam and the target nucleons respectively, i.e. can be u,d,s,b,c,t quarks or gluons.  $D_i^h(z, \mu^2)$  is the fragmentation function for a parton  $i$  to fragment into a hadron

Parameter	Tune 2C	Tune 2M	Tune 4C
SigmaProcess:alphaSvalue	0.135	0.1265	0.135
SpaceShower:rapidityOrder	on	on	on
SpaceShower:alphaSvalue	0.137	0.130	0.137
SpaceShower:pT0Ref	2.0	2.0	2.0
MultipleInteractions:alphaSvalue	0.135	0.127	0.135
MultipleInteractions:pT0Ref	2.320	2.455	2.085
MultipleInteractions:ecmPow	0.21	0.26	0.19
MultipleInteractions:bProfile	3	3	3
MultipleInteractions:expPow	1.60	1.15	2.00
BeamRemnants:reconnectRange	3.0	3.0	1.5
SigmaDiffractive:dampen	off	off	on
SigmaDiffractive:maxXB	N/A	N/A	65
SigmaDiffractive:maxAX	N/A	N/A	65
SigmaDiffractive:maxXX	N/A	N/A	65

Table 4.1: Comparison of different Tunes developed for Pythia [62]

$h$  with a momentum fraction of the parton  $z$ .  $\mu^2$  is the scale beyond which factorization is valid.

## 4.2 Hard Scattering Processes

### 4.2.1 Tune Parameters

Most of the data in Pythia is given as an input file and often referred to as a Tune, as of the version 8.150, Tune 4C has been a default in the main package. Depending on the type of phenomenology and the experiment, the Tunes vary and may not be quite compatible with one another or with a different experiment. Some of the model parameters in tunes can be read from the table 4.1.

Pythia has a lot of inbuilt PDF sets each calibrated to study a selected Physics case and is tune parameter dependent globally. Hence, the results for spectra are

expected to be different per PDF set. Pythia also provides a choice of collision type, i.e. a  $2 \rightarrow 2$  hard-scattering process, where the hadrons produced are based on three possibilities for colliding partons. To understand the difference of negative to positive spectra ratios per PDF set, a simulation of one million events were run per PDF set. There is some statistical fluctuation per PDF Set, but not very significant quantitatively.

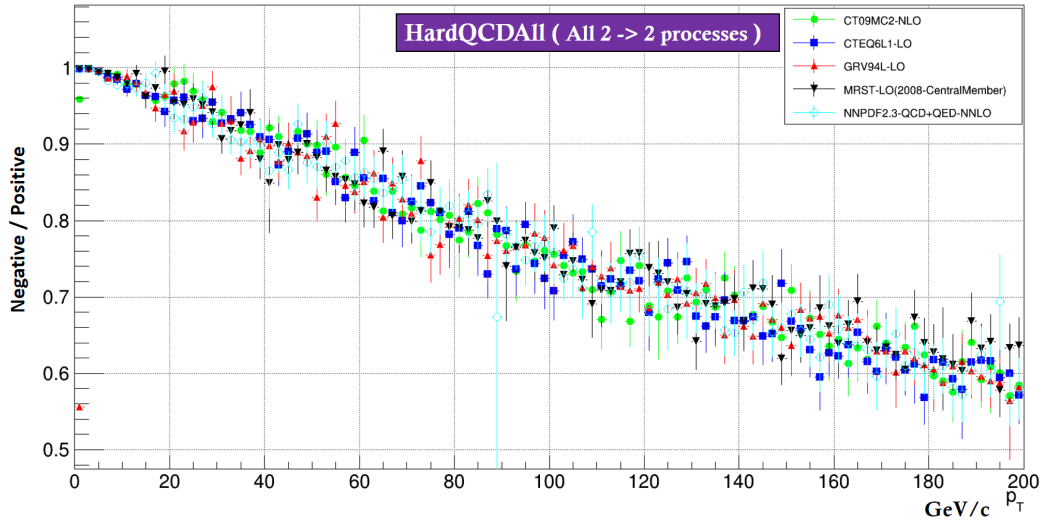


Figure 4.11: Negative/Positive Spectra for Pythia 8 based internal PDF Sets for all the hard qcd processes.

To identify the increase in the yield of positively or negatively charged particles as a function of the  $2 \rightarrow 2$  type of scattering, the spectra was obtained from each of three processes and the ratio was taken as a function of all the inbuilt PDF Sets provided by Pythia 8. The trend can be clearly seen in Fig. 4.12, where, the yield of positively charged hadrons as well as negatively charged hadrons is increasing as the  $p_T$  increases when the type of collision happens to be due to a quark participating in a hard scattering with another quark, giving rise to hadrons which eventually are hadronized to obtain the spectra. Similarly a decreasing trend is observed for the spectra of hadrons based on hard-scattering of gluons with respect to all the processes. Also, more importantly, only two of

the NLO PDF sets, show a difference, while *NNPDF2.3-QCD+QED-L014*, set also showing significant deviations for the yields from quark-quark scattering. More information about the PDF sets can be read from the references [23, 63, 64, 65, 66].

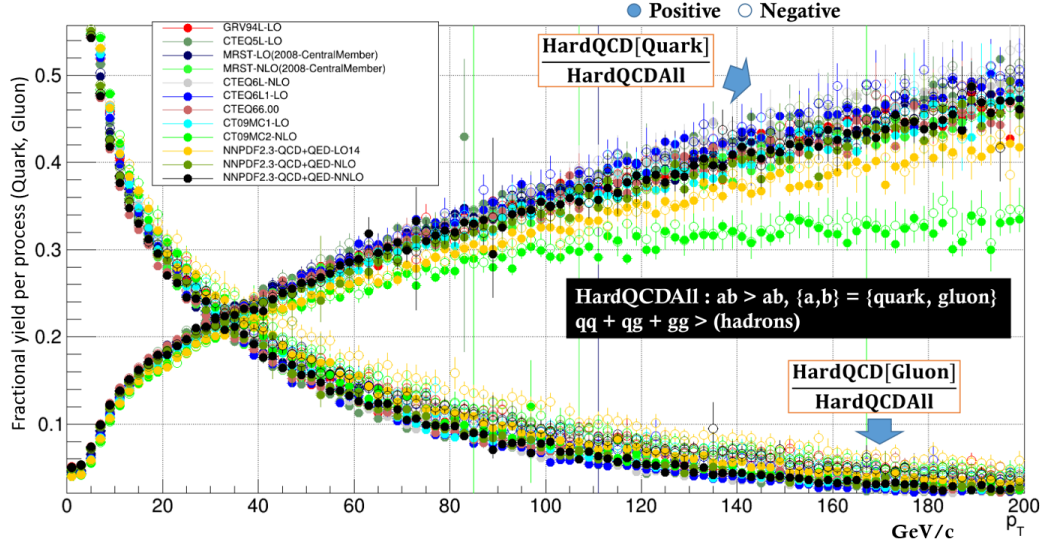


Figure 4.12: Comparing fractional yields for positive and negative charged particles based on quark and gluon switches.

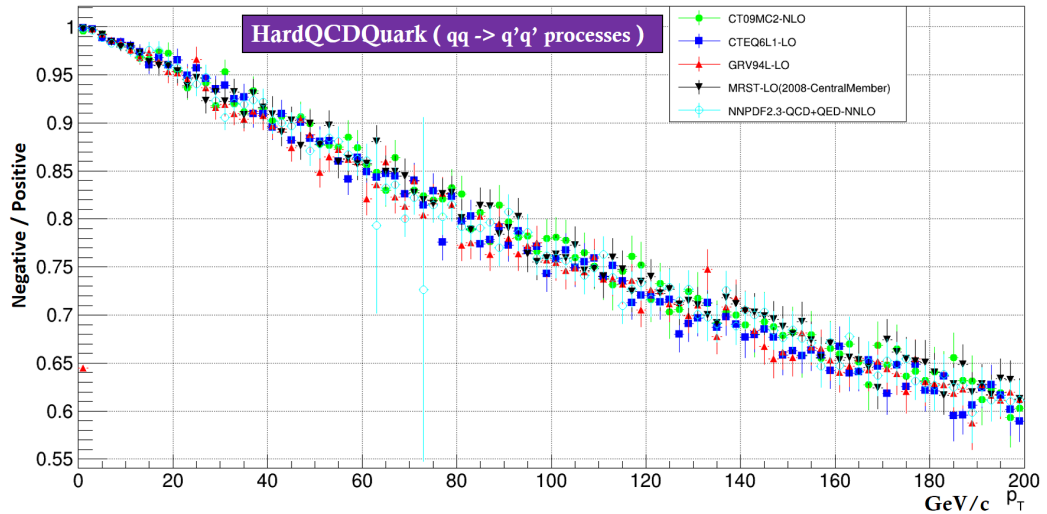


Figure 4.13: Negative to positive ratio of hadrons for only quark+quark collisions for inbuilt Pythia 8 PDF Sets.

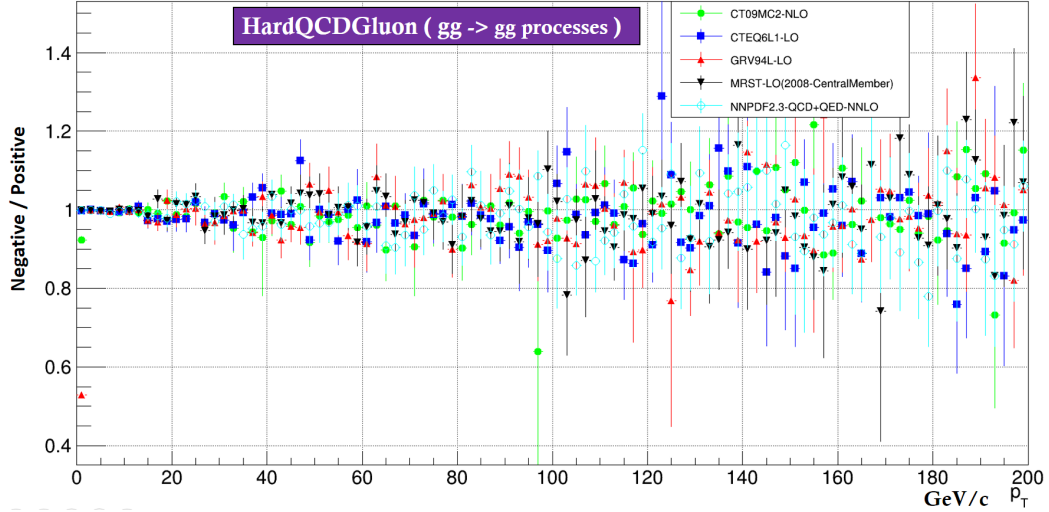


Figure 4.14: Negative to positive ratio of hadrons for only gluon+gluon collisions for inbuilt Pythia 8 PDF sets.

#### 4.2.2 Pythia 6 vs Pythia 8

There are some key differences between the Fortran version of Pythia and the C++ version of pythia in terms of parameters used and the labels they refer to. They are not quite the same as the official documentation mentions, although the physics content is the same. Pythia 8 is a very streamlined version of Pythia 6 with interfaces to other libraries like Les Houches Accord Parton Distribution Function (LHAPDF) and HepMC, so that the events generated can be consumed by other programs. A short list of differences in the parameter set can be found in the table 4.1.

### 4.3 Parton Distribution Functions (PDF)

Parton Distribution Function (PDF) is a key input to calculate cross-sections for several processes, where the incoming beams are hadrons. Since hadrons are composite particles made up of partons i.e. quarks and gluons, the information

about their momentum fractions are essential in any MC event generator doing parton-parton scatterings. Since PDFs cannot be obtained theoretically, they are obtained from various experiments and given as an input file parameterized with the variables momentum fraction  $x$  against the four momentum exchange  $Q^2$  among the partons [67].

#### 4.3.1 Experimental Measurement of PDFs

PDFs are measured primarily from the Deep Inelastic Scattering (DIS) experiments [32] and Drell-Yan (DY) scattering experiments [68, 69]. Experimentally PDFs are extracted from the *Fragmentation Functions*  $F_2$  which are measured from the cross-sections of an electron+positron, electron+proton, proton+proton and proton+nucleon collisions.

#### 4.3.2 Deep Inelastic Scattering (DIS)

DIS scattering experiments are those, where a hadron like a proton is collided with a lepton like an electron in order to explore the structure of the proton. In this process, the proton breaks inelastically and the electron interacts with a quark exchanging momenta, hence enabling the measurement of the momentum fraction of the partons. DIS was also one of experiment that validated the parton model of QCD 4.15.

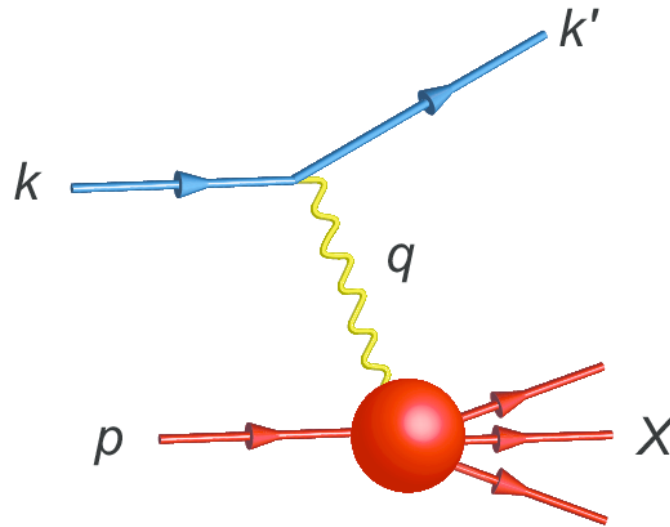


Figure 4.15: Deep Inelastic Scattering (DIS) : a lepton collides with a proton to probe the internal structure of the proton [20]

### 4.3.3 Drell-Yan Scattering (DY)

DY scattering is the process in which a parton from one nucleus and an anti-parton from another nucleus exchange momenta beyond the hard-scattering regime and annihilate to produce a pair of leptons. The advantage in considering this process for PDF extraction is that the properties outgoing particles are known, hence the cross-section formulas can be calculated analytically within the pQCD domain to extract the PDFs. A schematic showing the process, Fig. 4.16

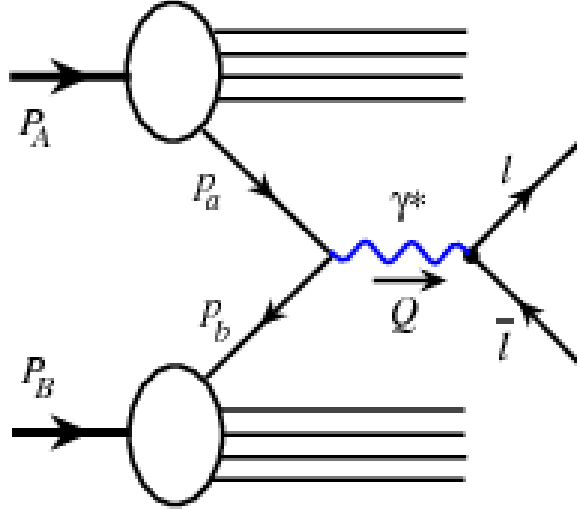


Figure 4.16: Drell-Yan Scattering (DY) : Lepton pair production from parton anti-parton annihilation [21]

#### 4.3.4 Physics Phenomena based on PDFs

The parton distributions in a free proton are not expected to be the same as in nuclear proton, which is bound, since the environment in which the hadrons live are different, and also the PDFs are a function of momentum transfer  $Q^2$  between two partons participating in hard-scattering.

Since the yields of hadrons are a consequence of colorless objects created from partons. The higher the number of partons generated as a consequence of collisions at a large  $Q^2$ , the higher would be the number of hadrons generated; however, experimentally, when nucleons are involved in the collisions, the yields of partons produced increase and decrease alternately.

The plot shown in Fig. 4.17 depicts three distinct regions for the physics phenomena, due to the free proton PDFs and bound proton PDFs. Note that the

momentum transfer should be beyond the hard-scattering limits and such a schematic plot is available for partons of different types as well [7].

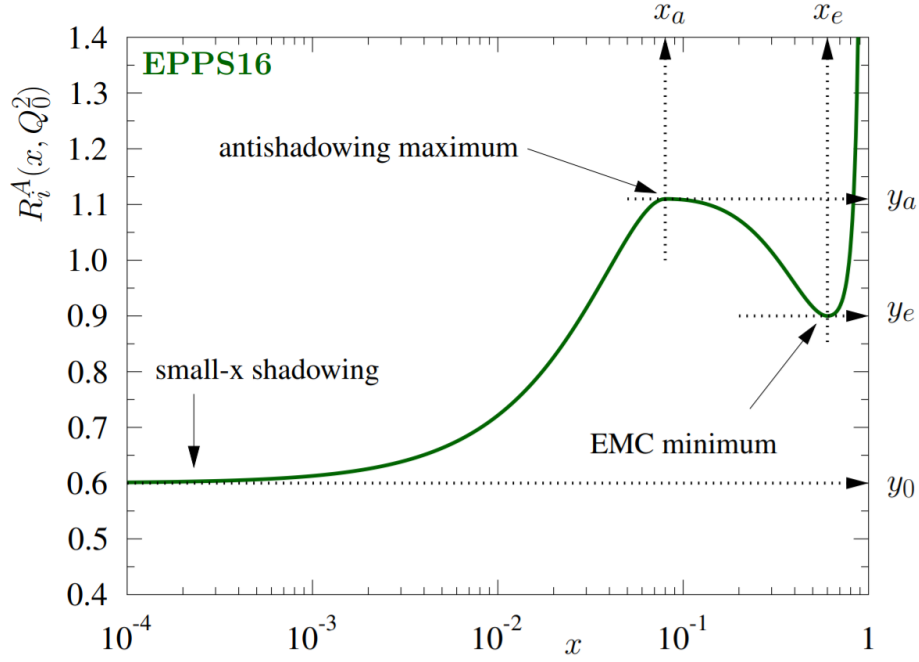


Figure 4.17: A schematic plot of ratio of parton distribution functions  $R_i^A(x, Q^2)$  as a function of the momentum fraction of the parton  $x$  and at a fixed value of four momentum exchange  $Q^2$  [7].

They are of four types and most of these phenomena do not yet have a concrete theoretical explanation. Since, a nuclear environment in which the hadron exists is very different from a free proton: PDF sets alone might not suffice to account for all nuclear effects because of the partons scattering from multiple nucleons.

*Shadowing* refers to the decrease in the yields of hadrons and *Anti-shadowing*, refers to the increase in the yields in comparing a free proton-nucleon based collision system to that of a symmetric proton-proton collision system :

- (a) *Shadowing at small-x* : At a very small value of  $x$ , i.e. when the momentum

fractions of the partons participating in the collision is very small, the momentum spectra of partons observed experimentally in a nucleon is less than the momentum fraction of partons in a free proton. The theoretical reasons for this is not yet available, despite the fact that the pQCD cross-sections are available.

- (b) *Anti-Shadowing* : This is the region where, the yields of partons from a nuclear PDF greater than the yield of partons in a free proton PDF.
- (c) *EMC Effect* : In this region, shadowing is at relatively larger- $x$ . This minimum from approximately  $x = 0.05$  to  $x = 0.65$  was first observed by the European Muon Collaboration during 1983 in comparing the PDFs of a iron nucleon to that of the deuteron nucleon and since then it has been cited as the *EMC Effect* [70].
- (d) *Fermi Motion* : Very large- $x$  partons have more intrinsic momentum, due to which they can participate in a lot of subsequent collisions until before they hadronize which one can intuitively expect to produce a greater number of hadrons in the final state in comparison with the hadrons from a pp collisions due to the lack of availability of such a large number of large- $x$  partons.

#### 4.3.5 PDFLIB and LHAPDF

PDFLIB is the package that contains a compiled list of parton distribution functions as a function of momentum fraction of the parton  $x$  and the momentum transferred square  $Q^2$ , from several experiments. It is written in Fortran 77 and has been in use for a very long time by several event generators. It is deprecated in favor of LHAPDF [22].

About 100 sets of such distributions from different experiments are compiled and are available for both the valence and sea quarks up to the heaviest top quark and the information is extracted from deep inelastic scattering experiments with the older sets compatible with leading order evolution using the DGLAP equation.

LHAPDF<sup>[71]</sup> is a library initially developed in Fortran 77 until version 5, as a successor to PDFLIB to create a better set of functions for the user. The latest LHAPDF version is developed in C++ since version 6 and is highly optimized with reduced memory foot print of the order of gigabytes. In PDFLIB, the interpolated values between two  $x$  values are also stored at a given  $Q^2$ , which made the code very cumbersome and backward incompatible when a certain version of DGLAP code needs to be used to generate PDFs at a different  $Q^2$ . Since then, LHAPDF chose to have the values only at the lowest value of  $Q^2$ , beyond which a DGLAP evolution code can be used to generate the values at a higher  $Q^2$ , instead of having to store the interpolated values as well and to eliminate the problem of backward compatibility with DGLAP. For this study, the latest version of LHAPDF v6 is used, which is also compatible with Pythia 8.

When using PDF distributions, systematic errors can be introduced due to the initialization values of that particular PDF Set, since the coupling constants and masses of quarks are initialized along with the PDF file.

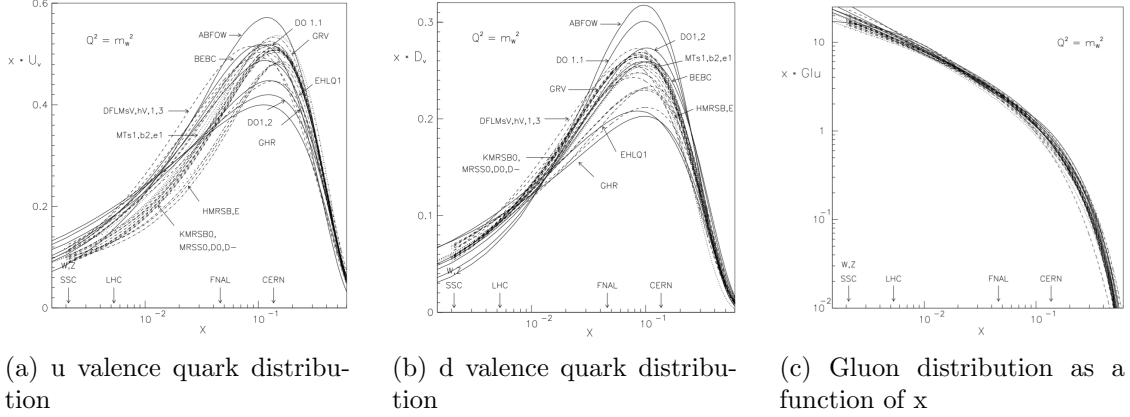


Figure 4.18: The distribution functions for the partons based on PDFLIB library, plotted as a function of  $x$  at  $Q^2 = m_w^2$ , where  $m_w$  is the mass of the W boson from [22] and the fluctuations are of the order of 20% can be noticed based on the choice of PDF used for analysis in the u and d quark distribution.

#### 4.3.6 DGLAP Equation

The parton distributions are different for varying energies of collision, i.e, they are a function of the momentum fraction  $x$  of the parton of a certain flavor and the momentum exchanged  $Q^2$ . Since, most of the experiments studying hadrons do so at only one energy, the PDF distributions extracted will be relevant for any simulation at only that specific energy range. However, during the late 1970s three Russian physicists, Dokshitzer, Gribov, Lipatov and two European physicists, Altarelli and Parisi [72, 73, 74], have written down an evolution equation, often referred to as DGLAP that helps to calculate the forward evolution of the PDF distribution, given a certain energy range. It should be noted that DGLAP calculations are valid only in the domain of perturbative QCD, and the current valid point is beyond the mass of the charm quark  $m_c = 1.69 GeV/c^2$ .

The inputs to the DGLAP equation require the PDFs at a certain  $Q^2$  range and a few functions referred to as the *Splitting Functions* calculated theoretically at *Leading Order(LO)* and *Next to Leading Order(NLO)*.  $LO(\alpha^2)$  and  $NLO(\alpha^3)$

refer to the parton level cross-sections at increasing orders of coupling constants i.e. the number of Feynman Diagrams required to do the calculations increase enormously as the order of cross-section is increased and a few automated tools have become available recently to do the calculations. Numerically, however, the hard-scattering cross-sections are multiplied with a K-factor assigning a value of 2 to account for any discrepancy, because of the non-inclusion of higher order terms [75].

An example of a DGLAP evolved PDF in the Fig. 4.19 shows the difference in the distributions of partons increased at larger value of  $Q^2$ .

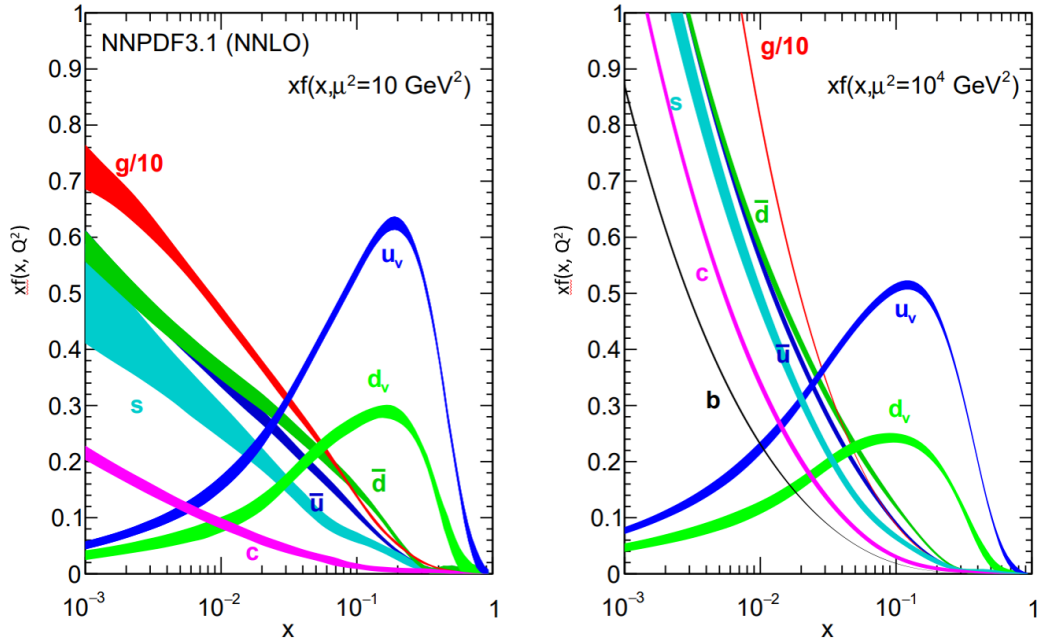


Figure 4.19: The figure to the left is the PDF distribution at a smaller value of four momentum  $Q^2 = 10 \text{ GeV}^2$  exchanged between the partons and the figure to the right is at a smaller value of four momentum  $Q^2 = 10^4 \text{ GeV}^2$  [23]

### 4.3.7 Free Proton PDF and Bound Proton PDF

Pythia v8, by default is based on the LO *CTEQ 5L* [65], the PDF for a free proton i.e. whenever Pythia is initialized, it collides two protons with *CTEQ 5L* PDFs. However with LHAPDF v6, the PDF sets could be changed based on the physics one would like to study. Free proton PDFs are the distribution functions for partons from a free proton in vacuum and Bound Proton PDFs are from a bound proton like that of a proton inside a lead nucleus. For this analysis only the distributions for the partons u, d and gluons become applicable.

There are several PDF distributions indexed by LHAPDF depending on the physics phenomena one would like to study, however only CT10nlo [63] and CT14nlo [76] are the free proton PDFs that have been used for this analysis. EPS09 is a nuclear PDF and EPPS16 is the successor to EPS09. Note that the nuclear PDF EPS09 [24] is unavailable for Pb nucleus, and is generated based on CT10nlo by Dr. Andy Buckley. The later version of the nuclear PDF EPPS16 is based on CT14nlo is available officially, hence the baseline spectra would be valid only if the free proton collisions are done with Pythia based on CT10nlo and CT14nlo for the comparison to be valid.

CT10nlo is as successor of CT09 PDFs used by CTEQ6.6 and it should be noted that for DGLAP a reference  $Q^2$  value is necessary, which for CT10 is at the mass of  $1.3\text{GeV}^2$

### 4.3.8 Nuclear PDFs: EPS09 and EPPS16

Because the EPS09 is the one that was used for HIN-12-017, a comparison check with the latest nuclear PDF EPPS16 for the outgoing hadrons might reveal any potential differences.

The experimental data for obtaining the EPS09 and EPPS16 are taken from CERN, FNAL, SLAC, NMC, EMC and RHIC. Drell-Yan based results are from FNAL and the rest of the data are from DIS experiments. The key differences between EPS09 and EPPS16 could be are tabulated below [24, 7].

- (a) The mass of the charm quark  $m_{\text{charm}} = 1.3\text{GeV}/c^2$  is taken as the factorization scale  $Q^2 > Q_0^2 (= m_{\text{charm}}^2)$  in EPPS16 as well as in EPS09.
- (b) The free proton PDF used in EPS09 is based on CTEQ6.1M and that of EPPS16 is based on CT14nlo
- (c) Isoscalar corrections were accounted for in EPPS16, which amount to the differences in the cross-sections due to the unequal number of proton and neutrons in the nucleus
- (d) CHORUS (anti)neutrino-Pb DIS data is also used to generate the PDF sets, because it was known that neutrinos are known to bound differently based on the flavor of the quarks.
- (e) LHC dijet data, LHC W and Z boson based on 2013 pPb collisions at the center of mass energy of is also considered.

The parton level nuclear modification factors  $\mathcal{R}_V^{Pb}$  for the lead nucleus plotted are calculated for light quarks i.e. u and d quarks only in comparison with u and d quarks from the proton. Similarly the plotting is done for sea quark,  $\mathcal{R}_S^{Pb}$ , however, in this case, strange sea quark are also included.

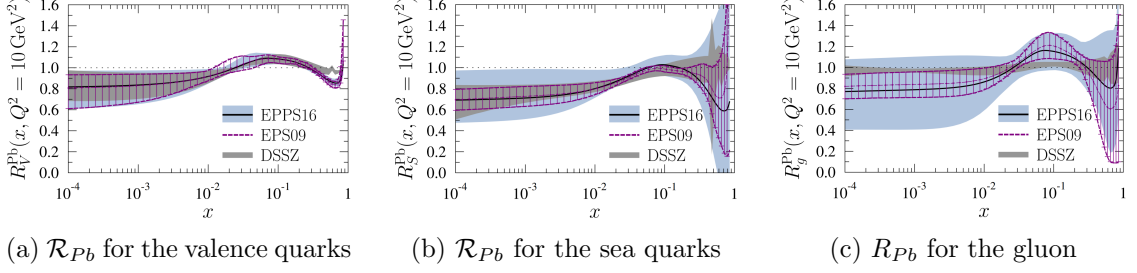


Figure 4.20: Valence quark, sea quark, EPS09 vs EPPS16 comparison [7]

$$\mathcal{R}_V^{Pb} \equiv \frac{u_V^{p/Pb} + d_V^{p/Pb}}{u_V^p + d_V^p}, \quad \mathcal{R}_S^{Pb} \equiv \frac{u_S^{p/Pb} + d_S^{p/Pb} + s_S^{p/Pb}}{u_S^p + d_S^p + s_S^{p/Pb}} \quad (4.1)$$

The suffix  $V$  is for valence quarks and  $S$  is for sea quarks respectively

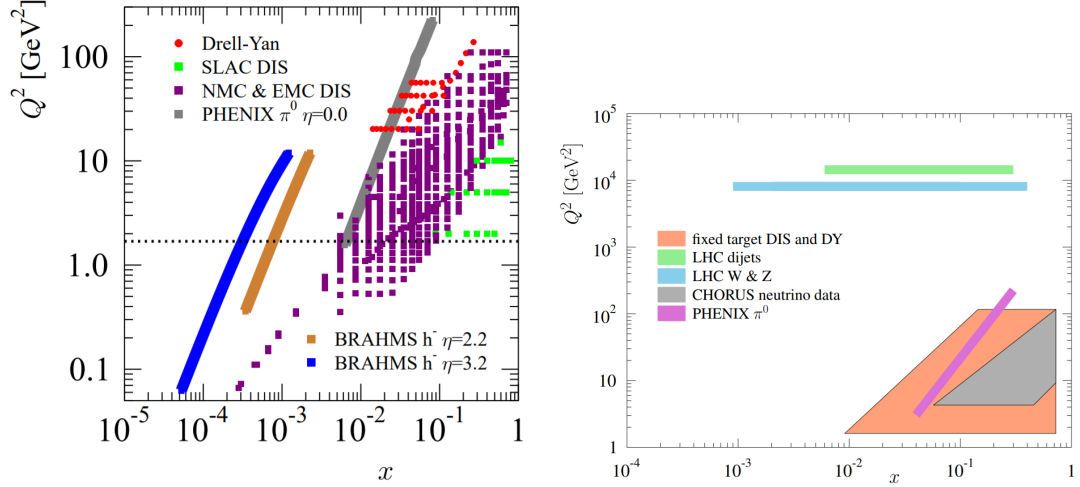


Figure 4.21: Kinematic reach plots or the  $x$  vs  $Q^2$  plots, to measure the extent to which the experimental data could be used for the generation of PDFs [7]

#### 4.3.9 $\hat{p}_T$ Spectra Summation

The momentum spectra of charged particles require the summation of hadron spectra from collisions in different  $\hat{p}_T$  ranges, because, the probability of producing a very high  $p_T$  hadron is very low and requires billions of parton level events to be simulated and takes a lot of time. Since, the momentum spectra of hadrons is produced from the collision of partons at a certain  $\hat{p}_T$  range, di-

<b>pPb Nuclear PDF</b>		
<b><math>\hat{p}_T</math> Range</b>	<b>EPPS16</b>	<b>EPS09</b>
10-20	1.88375	1.9092
20-30	1.3657e-1	1.3768e-1
30-50	3.142e-2	3.15485e-2
50-80	3.7672e-3	3.76655e-3
80-120	4.15156e-4	4.49585e-4
120-170	6.2644e-5	6.2214e-5
170-230	1.01589e-5	1.00765e-6
230-300	1.878e-6	1.859e-6
300-380	3.81785e-7	3.7834e-7
380-10000	1.07485e-7	1.0748e-7

Table 4.2: Cross-section data based on Pythia 8 simulations using the latest version of PDF set EPPS16+CT14nlo and the older version EPS09+CT10nlo.

viding the  $\hat{p}_T$  into 10 ranges and combining them is a practical choice to obtain the spectra for the desired range, which for this analysis runs from 0-120 GeV/c.

The 10  $\hat{p}_T$  intervals chosen to simulate using Pythia 8 are 1-30, 30-50, 50-80, 80-120, 120-170, 170-230, 230-300, 300-380, 380-10000 GeV/c to get the spectra of positive and negative charged particles for one million events. Each of the  $\hat{p}_T$ , generates hadrons only until a certain  $p_T$  range, i.e. consider the range for 1-30 in filled blue circles, the generates hadrons span only until  $\approx 30$  GeV/c, The method of summation of spectra of hadrons is by scaling the spectra with the cross-section values per  $\hat{p}_T$  and dividing by the total number of events, where the units for cross-section chosen is milli-barns. The same method was applied for hadron  $p_T$  spectra combination regardless of the nuclear PDF or free proton PDF, however an uncertainty was introduced in the cross-section values provided by Pythia and are tabulated below for each of the collision system, proton-lead and proton-proton.

The cross-sections obtained from Pythia by colliding a free proton PDF of

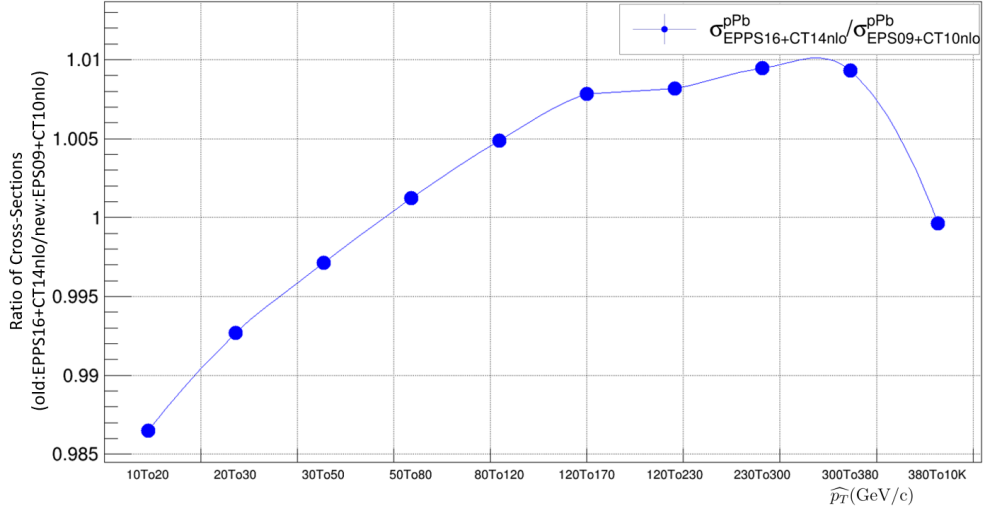


Figure 4.22: The ratio of cross-sections from Pythia 8 simulations comparing the free proton PDF of type EPPS16+CT14nlo to that of type another free proton PDF of type EPS09+CT10nlo from the Table. 4.2

CT10nlo with another free proton of the same type, i.e. a symmetric collision have a difference of about 3% as shown in the Fig. 4.23 and similarly for the case of a pPb like collision, where the ratios are taken for free proton collided with a nuclear proton for each of the PDF sets, with EPPS16 and EPS09, show a difference of the same amount.

Since the cross-sections are used for spectra combination, these errors introduce a systematic error when the nuclear modification factor for charged particles are calculated.

The final combined hadron spectra for positively charged particles, for all the 10  $\hat{p}_T$  before normalization in Fig. 4.25 and after normalization in Fig. 4.26.

<b>pp PDF</b>		
<b><math>\hat{p}_T</math> Range</b>	<b>CT14nlo</b>	<b>CT10nlo</b>
10-20	1.95255	1.9414
20-30	1.37225e-1	1.36395e-1
30-50	3.1084e-2	3.08815e-2
50-80	3.67505e-3	3.64185e-3
80-120	4.379e-4	4.33825e-4
120-170	6.0765e-5	6.0311e-5
170-230	9.92355e-6	9.88035e-6
230-300	1.85395e-6	1.8549e-6
300-380	3.82485e-7	3.8502e-7
380-10000	1.09925e-7	1.123e-7

Table 4.3: Cross-section data based on Pythia 8 simulations using the latest version of PDF set CT14nlo and the older version CT10nlo.

#### 4.3.10 Momentum Fraction of the Parton vs $Q^2$

The number of partons participating in a hard scattering is a function of the four momentum transfer  $Q^2$  between the partons i.e. larger the magnitude of  $Q^2$  can translate to a higher  $p_T$  of the final state hadron. Since Pythia provides a way to divide the collision into different  $p_T$  intervals, by studying the structure of the two dimensional plots, one can infer for any difference in the positive and negative charged particles.

Since many to many mapping, where the momentum fraction of several partons in a single collision generates several hadrons, an average of one of the variables, either  $x$  or  $p_T$  would help make a reliable estimate. In this analysis,  $x_1$ , the momentum fraction of parton from a free proton is matched against the mean of the transverse momentum of positive and negative charged particles respectively and the same method is repeated for  $x_2$ , the momentum fraction of a parton from a bound proton.

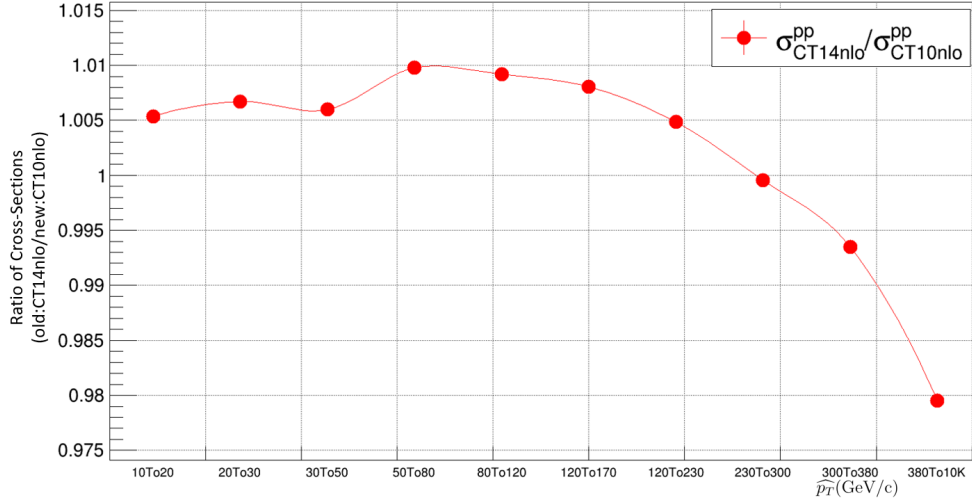


Figure 4.23: The ratio of cross-sections from Pythia 8 simulations comparing the free proton PDF of type CT14nlo to that of type another free proton PDF of type CT10nlo from the Table. 4.3

The Fig. 4.27, shows for three different  $\hat{p}_T$ s involved in the collisions and the spectrum of hadrons produced as a colored patch, whose values can be read in the bar to the right of the figure. As it can be noticed, the  $\hat{p}_T$  for 120-170 GeV/c and 380-10000GeV/c shows a different structure, but when the summation for all  $\hat{p}_T$  is done, the structure would be different. This way, any changes in positively and negatively charged particles can be observed.

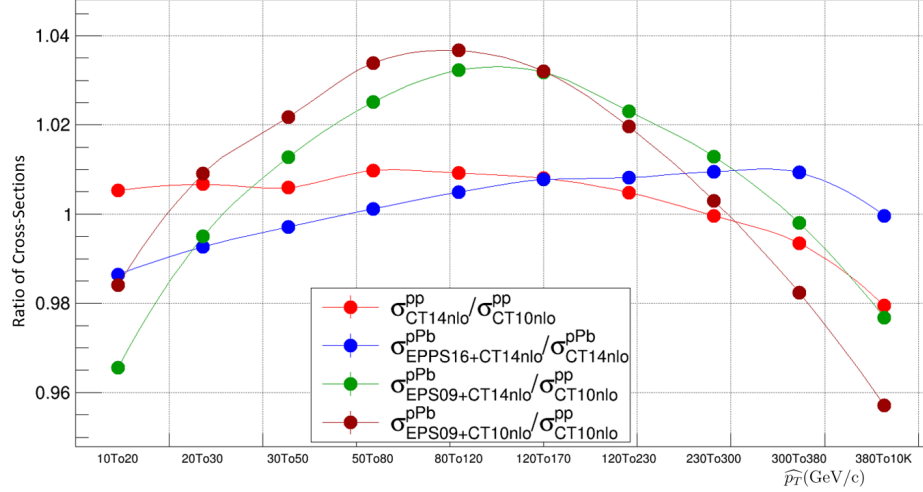


Figure 4.24:  $\sigma_{\text{PDF Set}}^{\langle \text{collision system} \rangle}$  represents the cross-section of a certain type of collision system and the PDF set based on which the cross-section values are obtained. The plot gives the of comparison for cross-sections from different collision systems, a symmetric pp collision system with two PDF sets CT10nlo and CT14nlo, and an asymmetric pPb collision system with the two PDF sets EPPS16+CT14nlo and EPS09+C10nlo are compared along with the plots shown above for different  $\hat{p}_T$  intervals in units of GeV/c

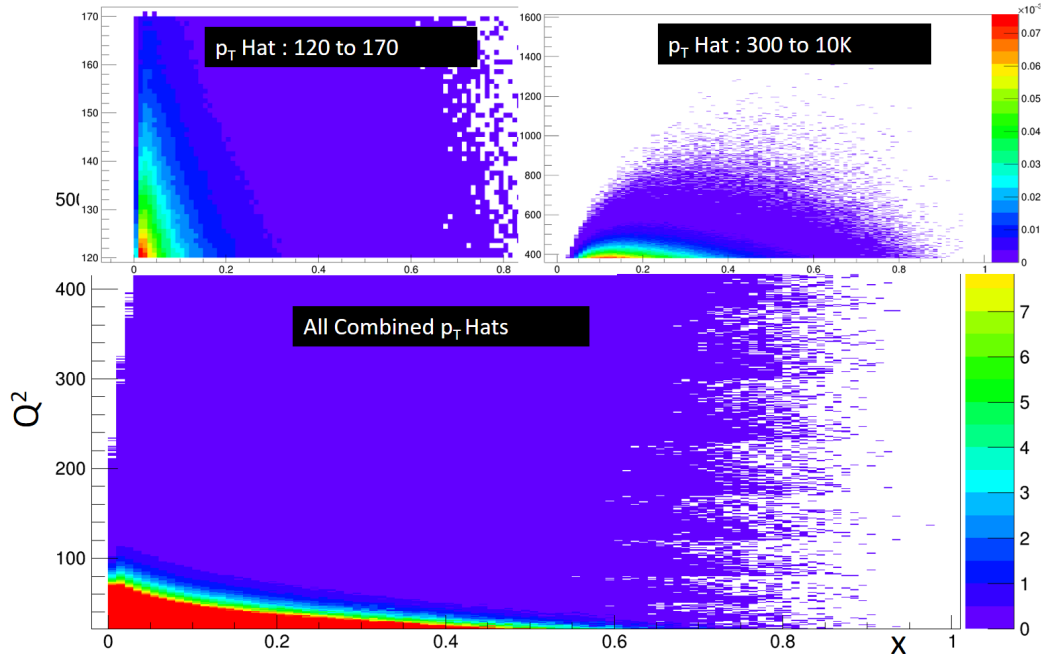


Figure 4.27: Momentum fraction of the parton vs the four momentum exchange for three different intervals  $\hat{p}_T$ s 120-170, 300-10K, combined for positive charged particles. Note that the same plots appear identical for negative charged particles as well.

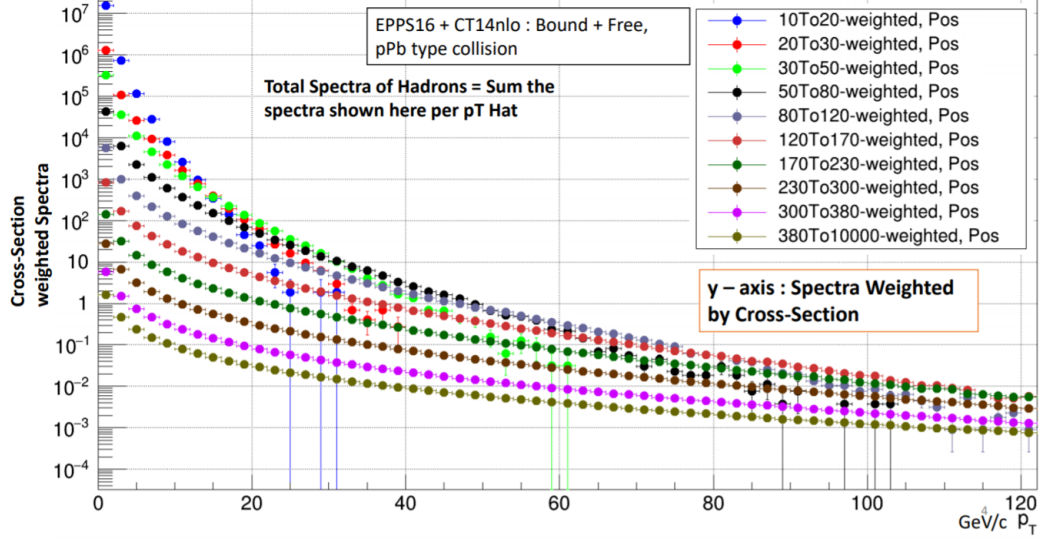


Figure 4.25: Spectra of positively charged particles from Tune4C for all  $\hat{p}_T$ s after cross-section weighting

#### 4.3.11 Mean Momentum Fraction of the Parton vs $p_T^{\text{hadron}}$

Since the incoming partons participating in hard scattering are responsible for the production of final state hadrons, a plot of the observable  $x$ , the momentum fraction of the parton vs the transverse momentum of positive and negative charged hadrons  $p_T$  would help understand the differences in the spectra yield of positive and negative charged particles produced due to partons participating at a certain momentum fraction.

The method of extraction of this function is by averaging the partons in a certain momentum fraction bin, because, there is more than one parton per event, that is responsible for producing a hadron i.e. say a parton of momentum fraction 0.2 units can produce a hadron of  $p_T = 20 \text{ GeV}/c$  in one event, and in another event, it can produce  $p_T = 50 \text{ GeV}/c$ . Therefore tagging per event is computationally expensive, hence, the mean momentum fraction is chosen for  $\langle x_{1,2} \rangle$ .

The Fig. 4.28, 4.29 are the results for the pp collisions in vacuum, based on the

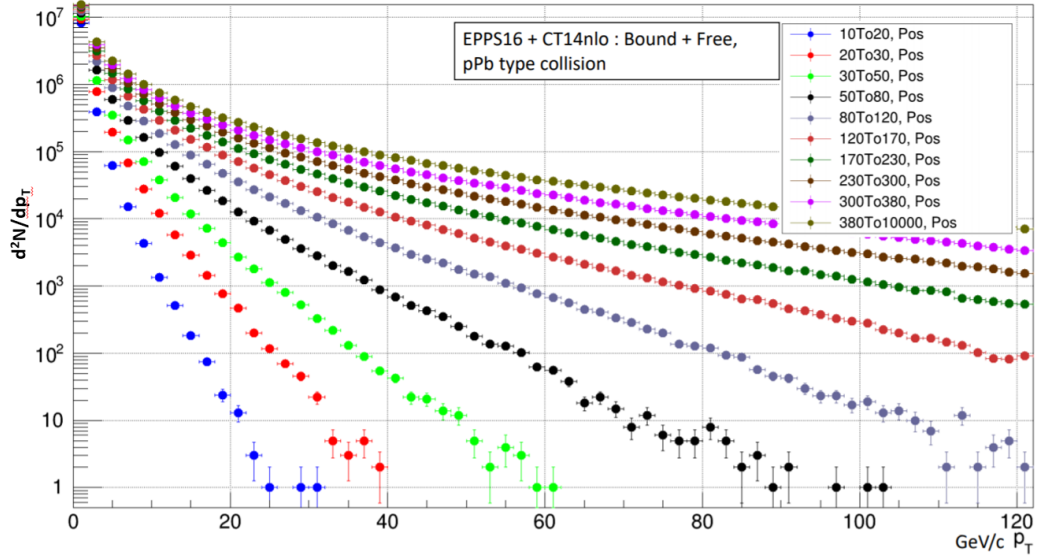


Figure 4.26: Spectra of positively charged particles from Tune4C for all  $\hat{p}_T$ s before cross-section weighting

CT14nlo for the momentum fractions  $x_1, x_2$  of partons from the target and the beam. This is the case of a symmetric collision. Hence, statistically for a large number of events, the yields of hadrons for all the charged particles are almost identical, however, here the goal is to search for the asymmetry in the yields of positive and negative charged particles.

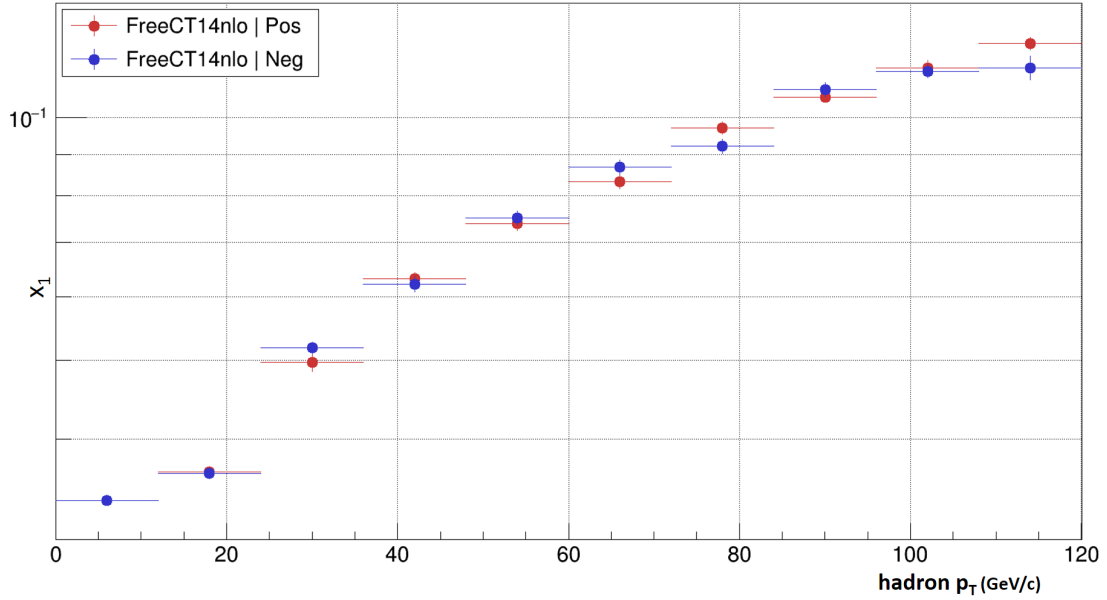


Figure 4.28:  $\langle x_1 \rangle$  vs hadron  $p_T$  for positive and negative charged particles from free proton pdf CT14nlo

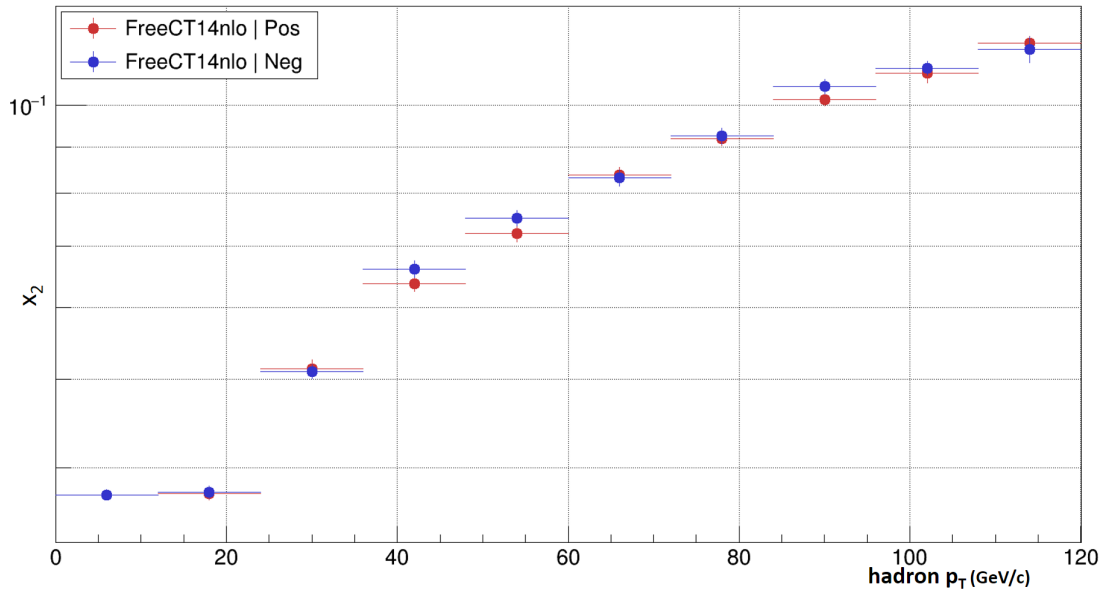


Figure 4.29:  $\langle x_2 \rangle$  vs hadron  $p_T$  for positive and negative charged particles from free proton pdf CT14nlo

Spectra summation makes use of cross-sections given by Pythia, which can be a source of systematic error, in order to account for that, the following plots are made and the results in Fig. 4.30, 4.31, 4.32, 4.33, show the difference, which

are practically identically i.e. cross-section numbers are not contributing much for  $\langle x \rangle$  vs  $p_T$  plots.

In order to compare an anti-symmetric collision system, one proton having a bound PDF (EPPS16 corrected with CT14nlo) and the other free proton (CT14nlo), the following plots compare the differences in  $\langle x_1 \rangle$  vs Positive,  $\langle x_2 \rangle$  vs Positive,  $\langle x_1 \rangle$  vs  $\langle x_2 \rangle$  for positive and negative separately. The differences are very small, less than a 1%, hence no obvious conclusions could be inferred from the plots.

Figure 4.30: Comparing the  $\langle x_1 \rangle$  for positive and negative charged particle yields for asymmetric pPb type collision based on EPPS16 PDF Set.

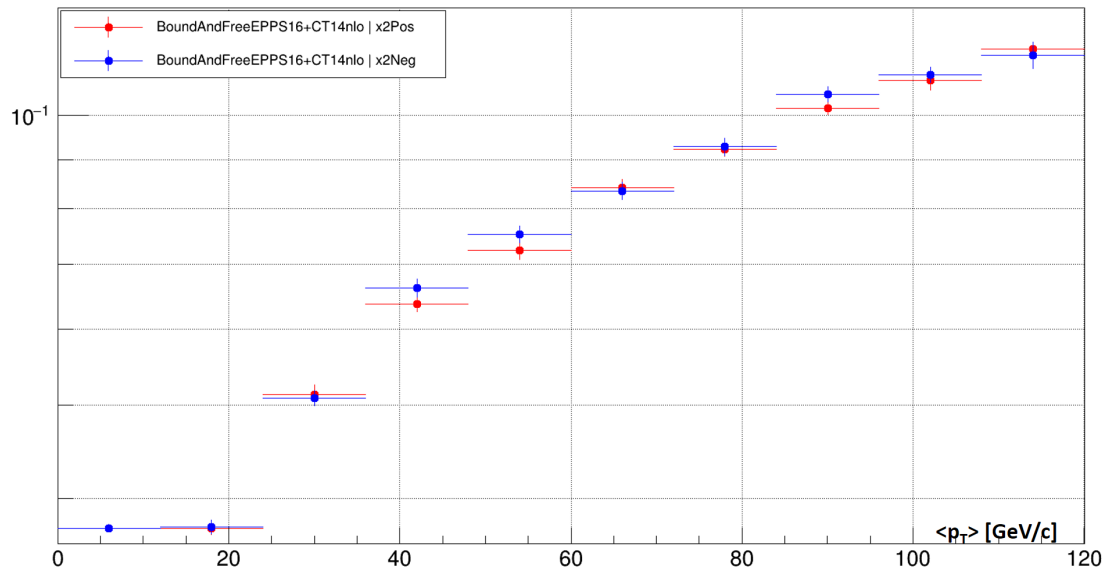


Figure 4.31: Comparing the  $\langle x_2 \rangle$  for positive and negative charged particle yields for asymmetric pPb type collision based on EPPS16 PDF Set.

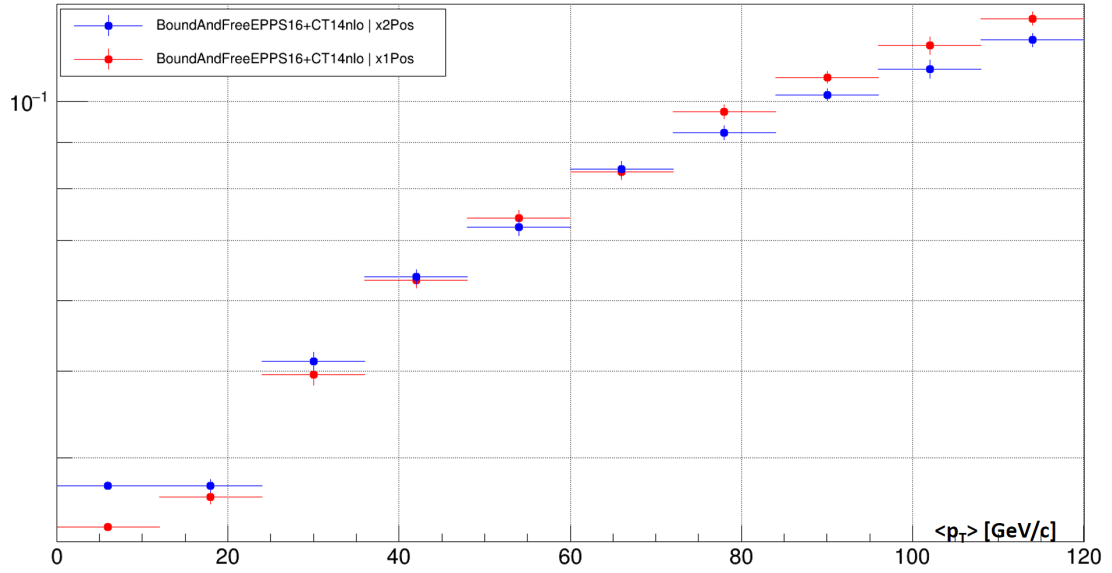


Figure 4.32: Comparing  $\langle x_1 \rangle$  vs  $\langle x_2 \rangle$  for all partons contributing to positively charged particles.

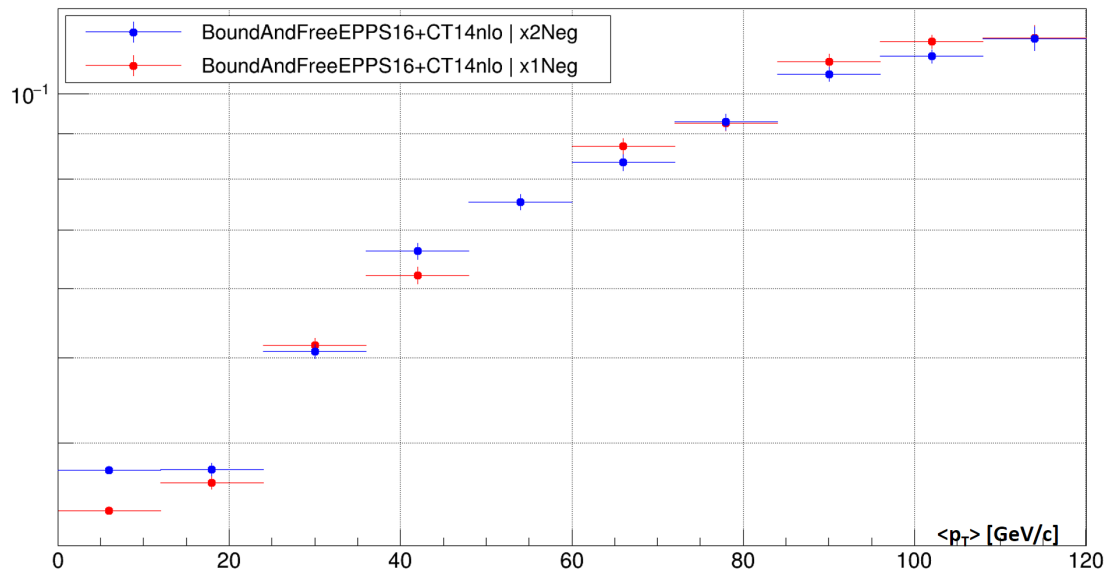


Figure 4.33: Comparing  $\langle x_1 \rangle$  vs  $\langle x_2 \rangle$  for all partons contributing to negatively charged particles.

### 4.3.12 Data and MC Comparison : Ratio of Negative To Positively Charged Particle Spectra

Based on the Figs. 4.36, 4.34, 4.35, it can be concluded that there are more number of positive charged particles compared to negatively charged particle and also, the results from simulations based on nuclear PDFs match well with pp, pPb and PbPb data within statistical uncertainties. A Bound+Bound collision system can be likened to a Pb+Pb like collision system, Free+Free collision system can be likened to a free proton colliding with another free proton and Bound+Free collision system can be likened to a free proton colliding with a lead nucleon.

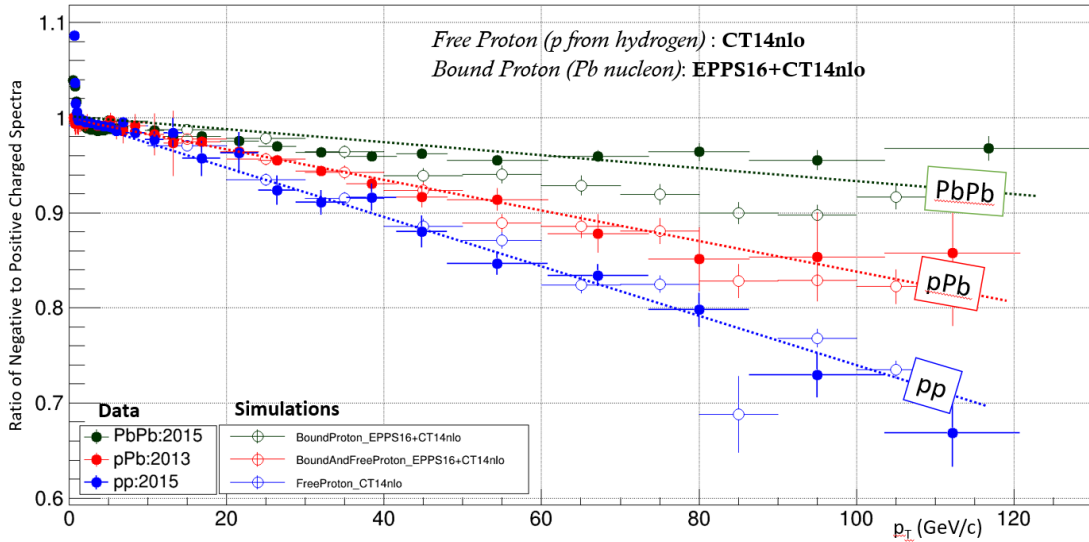


Figure 4.34: Comparing negative to positive ratios for different collision systems from Pythia simulations by varying the PDF sets (Pb:EPPS16+CT14nlo, p:CT14nlo) and real data for pp, pPb and PbPb collision systems. The dotted lines matching the colors is to show the linearity amongst different collision systems.

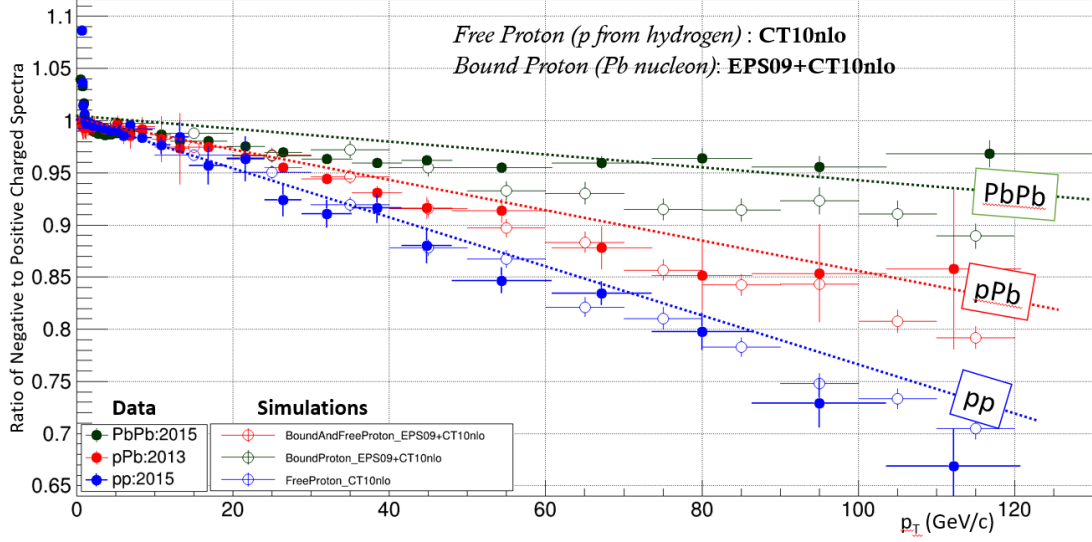


Figure 4.35: Comparing negative to positive ratios for different collision systems from Pythia simulations by varying the PDF sets (Pb:EPS09+CT10nlo, p:CT10nlo) and real data for pp, pPb and PbPb collision systems. The dotted lines matching the colors is to show the linearity amongst different collision systems.

The negative to positive ratios of hadrons obtained from three different data sets and the results from simulations are all measured at the same center of mass energy i.e.  $\sqrt{s_{NN}} = 5.02 TeV$ . The methods used to obtain the data points for charged particles are nearly identical for pp, pPb and PbPb data sets and within the same pseudorapidity range  $|\eta| < 1$ . Primarily, the information from the tracking detector was used for measuring the charged particle spectra. More information about the *Tracking Detector* [2.1.6] is available in Chapter 2 and also, the data set related information is taken from the analysis notes for the papers: [43, 57]. The choice of track labels is *highPurity*, which is a label for a set of high quality tracks with a set of statistically chosen parameters, where the detector specifics are taken into account, that give the best quality charged particle tracks.

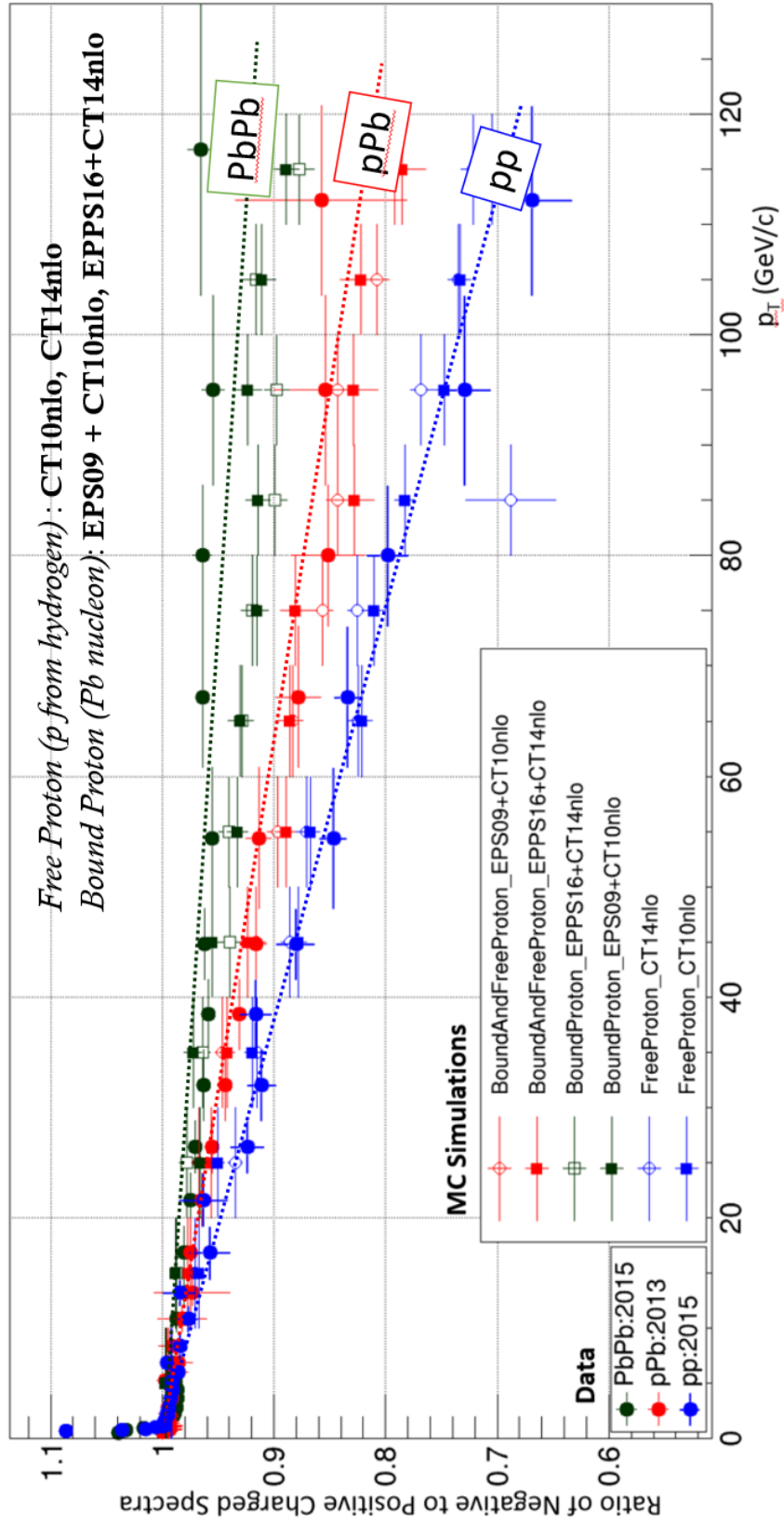


Figure 4.36: Combining the figures 4.35, 4.34 based on the older version (EPS09, CT10nlo) and the newer version (EPPS16, CT14nlo) respectively.

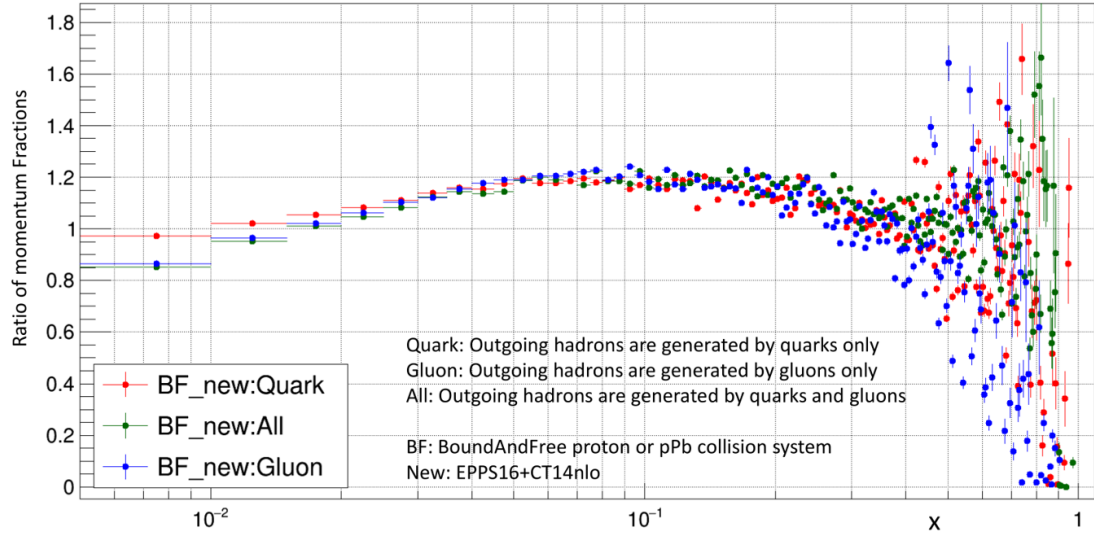


Figure 4.37: Ratio of momentum fraction of parton from the Pb going side ( $x_2$ ) to the parton from from the proton going side ( $x_1$ )

#### 4.3.13 Initial State Effect vs Final State Effect

There are three points in Pythia from which parton information and hadron information could be extracted. (1) The partons that went in at the onset of collision i.e. *Initial State* partons, (2) The partons just before hadronization, and (3) The final state positively and negatively charged hadrons.

By correlating the information at these three points, it could be inferred which partons are influencing the production of positive and negative charged particles to account for their differences.

In the Fig. 4.37, the ratio of the momentum fraction of the partons from the Pb going side and the p going side are taken, which is essentially the ratio of the PDF sets, similar to the Fig. 4.17 for all the three processes. The results appear similar regardless of the choice the process i.e. for all the different  $2 \rightarrow 2$  processes under consideration providing a sanity check for the underlying PDF

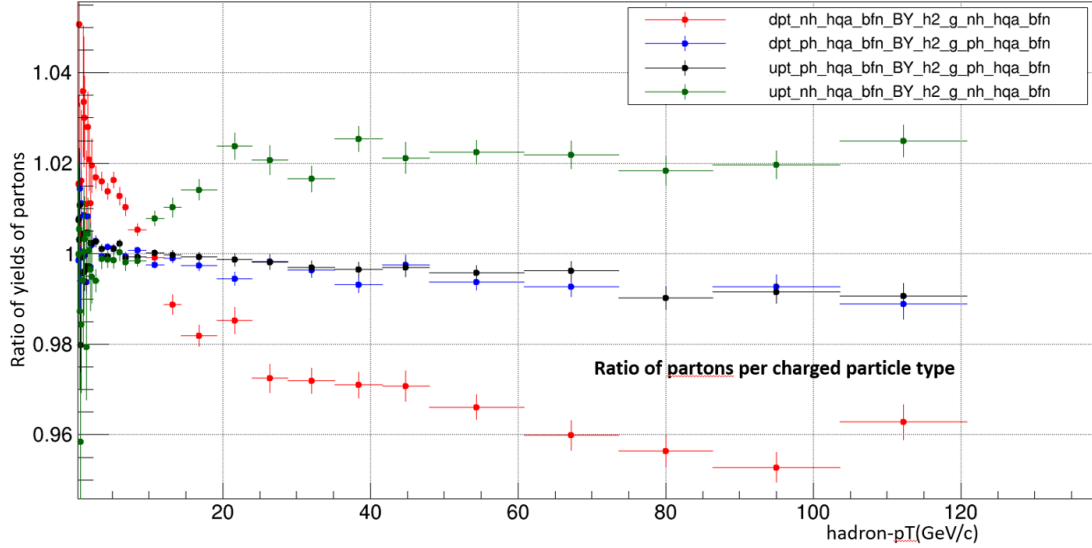


Figure 4.38: Ratio of parton yields as a function of the charge type of the hadron. dpt: d-quark, hqa: HardQCDAll, bfn: Bound and Free Proton Collision, g: gluon, nh: negative charged hadron, ph: positively charged hadron.

set ratios when an asymmetric collision system is taken.

The similarity in the Fig. 4.27 for  $x$  vs  $Q^2$  for both positive and negative charged particles implies the results are likely not due to an initial state.

In the Fig. 4.38, the ratio of parton of one type to the parton of other type is compared against the hadron of a specific charge type i.e. positive or negative. The ratio of partons are approximately linear for both positive and negative charged hadrons. Based on the simulations, it can be concluded that, in order to have a constant negative to positive charged hadron ratios, a linearity in the ratios of partons might be necessary. Note that the ratios amongst partons could not be uniquely related to the final state negative to positive charged hadrons. Also, the linear relationship amongst parton ratios is obtained for a large number of hadrons be it positive or negative, and for a total of one million collision events.

Note that, the construction of the hadron from scratch is a historically important unsolved problem, as listed in the *Clay Millenium Prize* problems. It is often referred to by the name Quantum Yang-Mills Theory [77]. The results obtained in this particular analysis are purely phenomenological in nature, hence, associating a parton to a hadron implies, the associated partons are contained in the hadron. Hence, the estimates even if be quantitative are crude in nature.

Thus, based on simulations with Pythia 8, it can be inferred that the negative to positive ratios of hadrons are likely to be a result of the final state parton production and possibly not an initial state effect.

#### 4.4 Summary

- Pythia, an event generator evolved from a Fortran 77 based simulator to a widely used C++ simulator for colliding different species, and hadronization with various tunes.
- Parton Distribution Functions(PDF) require input from several experiments which are additionally processed to obtain the free proton PDF and bound proton PDF.
- Obtaining hadrons from different  $\hat{p}_T$ s and combining them, helps reduce the time to generate very high  $p_T$  hadrons because of the very low probability of producing them.
- Based on similarity in the features observed in  $x$  vs  $p_T$  and  $x$  vs  $Q^2$  from Pythia 8 simulations for positive and negative charged hadrons, it can be concluded that, the negative to positive ratios are likely to be not an *initial*

*state effect.*

- Based on Fig. 4.38, it can be inferred that the ratios of partons correlated against negative or positive hadrons show a linearity, implying the ratio of positive to negative hadrons are likely to be a *final state effect*.

## Chapter 5

### Summary and Future Outlook

This analysis helps us understand the asymmetry of the charged particle ratios through simulations. Since PDF distributions are prone to several uncertainties and is dependent on the type of phenomena one would like to study, it is necessary to have the nucleon PDFs and the free proton PDFs be validated by the concerned groups before matching with the experimental data. Nuclear PDFs for this analysis was given by EPPS group and Free proton PDFs from the LHAPDF group [71].

In this analysis hadrons are generated by varying the PDF distributions, the outcome is compared with the experiment, hence, it provides a new source of input to the PDFs themselves to compare with hadrons at very high  $p_T$ , as was done for the EPS09 PDF which was compared with BRAHMS experiment.

This study helps explore the phenomena of *anti-Shadowing* better, where there is a increase in the hadron yield corresponding to a parton level participation at very high momentum fraction, since the mechanism by which this phenomena happens is less well understood.

Since experimental groups are dependent on various tunes or the flavors for the underlying event generator in use, a method to keep track of how much the physics observable is different with respect to different experiments needs to be monitored. To account for such a discrepancy, the project *Rivet* [78]

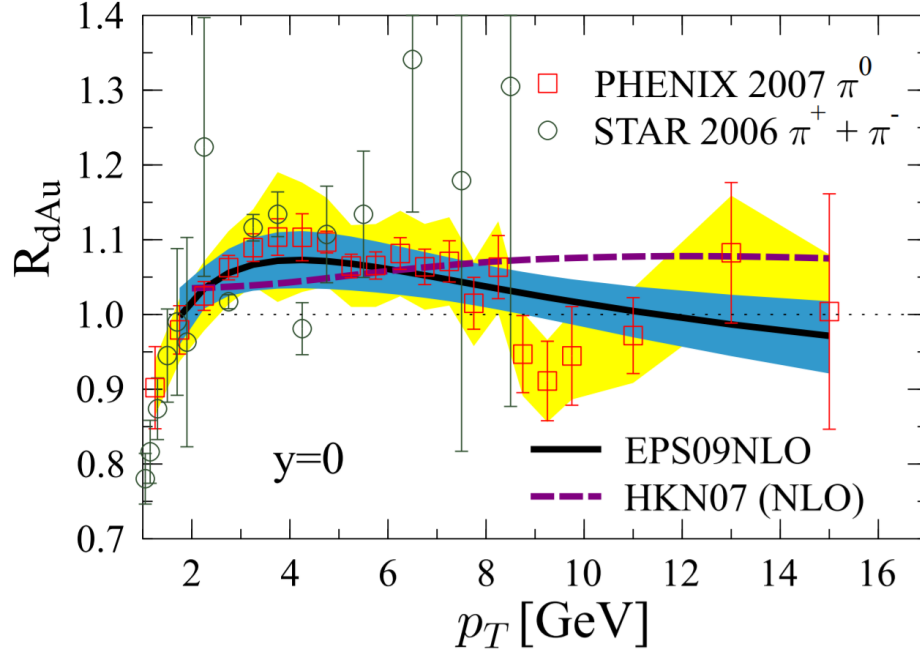


Figure 5.1: Comparing the Nuclear Modification Factor  $R_{pA}$  for a deuteron-gold collision system based on two different experiments PHENIX and STAR and for two different nuclear PDFs EPS09nlo and HKN07 [24].

was started in the 2012, [78] and helps not only validate but also compare the Monte-Carlo event generators with experimental data. Also *Professor* [79], a tool was created to prevent the effort in creating new tuning parameters based on brute-force method. Since brute force method leads to a waste of computing resources and with the increase in parameters, the time it takes to produce results grows exponentially.

## Tune Comparisons

Gen	Tune	UE	Dijets	Multijets	Jet shapes	W and Z	Fragmentation	B frag
<b>PYTHIA6</b>	AMBT1	0.39	1.20	0.54	0.77	0.27	0.93	1.63
	AUET2B-CTEQ6L1	0.16	0.92	0.44	0.59	0.74	0.67	0.91
	AUET2B-LOxx	0.13	1.33	0.55	0.58	1.15	0.67	0.90
	D6T	0.58	0.79	0.50	0.56	1.25	0.36	2.63
	DW	0.81	0.78	0.61	0.56	1.33	0.36	2.63
	P2010	0.30	0.93	0.82	1.07	0.30	0.44	1.74
	P2011	0.12	0.89	0.67	1.02	0.53	0.43	2.13
	ProfQ2	0.51	0.67	0.81	0.51	0.64	0.30	1.16
	Z2	0.18	0.94	0.73	0.80	0.30	0.95	2.78
<b>Pythia8</b>	4C	0.30	0.97	0.93	0.50	0.90	0.38	0.98

Figure 5.2: Deviation metrics per gen/tune and observable group [25, 26, 27]

Since the PDF sets, which are a core input to Pythia have changed, submission of the results to Rivet using the Professor tool would help resolve any possible discrepancy with the choice of the Tune, which is 4C [62].

The wealth of information from the momentum fraction of the partons versus the transverse momenta of the hadrons can be used to precisely pin point the increase/decrease of the positively charged particles over the negatively charged particles depending on the choice of the collision per PDF set. Additionally, it should be possible to extract parton specific momentum fractions as well and map them to hadron yields.

## References

- [1] Daniel Britzger. QCD Results from HERA. In *Proceedings, 52nd Rencontres de Moriond on QCD and High Energy Interactions: La Thuile, Italy, March 25-April 1, 2017*, 2017.
- [2] Tapan Nayak and Bikash Sinha. Search and study of Quark Gluon Plasma at the CERN-LHC. (arXiv:0904.3428):131–144. 15 p, Apr 2009. Comments: 15 pages, Invited article for the volume on LHC physics to celebrate the Platinum Jubilee of the Indian National Science Academy, Edited by Amitava Datta, Biswarup Mukhopadhyaya and Amitava Raychaudhuri (Jan 2009).
- [3] Guang-You Qin. Anisotropic Flow and Jet Quenching in Relativistic Nuclear Collisions. *Int. J. Mod. Phys.*, E24(02):1530001, 2015.
- [4] Vardan Khachatryan et al. Charged-particle nuclear modification factors in PbPb and pPb collisions at  $\sqrt{s_{\text{NN}}} = 5.02$  TeV. *JHEP*, 04:039, 2017.
- [5] Serguei Chatrchyan et al. Dependence on pseudorapidity and centrality of charged hadron production in PbPb collisions at a nucleon-nucleon centre-of-mass energy of 2.76 TeV. *JHEP*, 08:141, 2011.
- [6] Vardan Khachatryan et al. Nuclear Effects on the Transverse Momentum Spectra of Charged Particles in pPb Collisions at  $\sqrt{s_{\text{NN}}} = 5.02$  TeV. *Eur. Phys. J.*, C75(5):237, 2015.
- [7] Kari J. Eskola, Petja Paakkinen, Hannu Paukkunen, and Carlos A. Salgado. Epps16: nuclear parton distributions with lhc data. *The European Physical Journal C*, 77(3):163, Mar 2017.

- [8] Hywel Owen, Suliman Alshammari, Robert Appleby, Roger Barlow, and Adina Toader. Simulation of the LHC Collimation System Using MERLIN. In *Particle accelerator. Proceedings, 23rd Conference, PAC'09, Vancouver, Canada, May 4-8, 2009*, page WE6RFP012, 2010.
- [9] T.G. Karayiannis and M.M. Mahmoud. Flow boiling in microchannels: Fundamentals and applications. *Applied Thermal Engineering*, 115:1372 – 1397, 2017.
- [10] The CMS Collaboration and S Chatrchyan et. al. The cms experiment at the cern lhc. *Journal of Instrumentation*, 3(08):S08004, 2008.
- [11] Oleg A. Grachov, M. J. Murray, A. S. Ayan, P. Debbins, E. Norbeck, Y. Onel, and David G. d'Enterria. Status of zero degree calorimeter for CMS experiment. *AIP Conf. Proc.*, 867:258–265, 2006. [,258(2006)].
- [12] <https://sciencenode.org/feature/large-hadron-colliders-worldwide-computer.php>.
- [13] <https://twiki.cern.ch/twiki/bin/view/cmspublic/workbookcmsswframework>.
- [14] Hassen Riahi. *Design optimization of the Grid data analysis workflow in CMS*. PhD thesis, Perugia U., 2012-02-01.
- [15] <https://press.cern/press-releases/2016/05/2016-physics-season-starts-lhc>.
- [16] <https://www.sciencedaily.com/releases/2017/04/170410130104.htm>.
- [17] <http://steve.cooleysekula.net/goingupalleys/2011/09/05/physics-in-collision-2011/>.
- [18] Torbjorn Sjostrand, Stephen Mrenna, and Peter Z. Skands. A Brief Introduction to PYTHIA 8.1. *Comput. Phys. Commun.*, 178:852–867, 2008.

- [19] T. Tymieniecka and A. F. Zarnecki. Formulae and figures for basic two-body QCD processes in e p interaction. 1992.
- [20] Martin Hentschinski. Proton structure functions at small x. *Journal of Physics: Conference Series*, 651(1):012011, 2015.
- [21] Jen-Chieh Peng and Jian-Wei Qiu. Novel phenomenology of parton distributions from the DrellYan process. *Prog. Part. Nucl. Phys.*, 76:43–75, 2014.
- [22] H. Plathow-Besch. PDFLIB: A Library of all available parton density functions of the nucleon, the pion and the photon and the corresponding alpha-s calculations. *Comput. Phys. Commun.*, 75:396–416, 1993.
- [23] Richard D. Ball et al. Parton distributions from high-precision collider data. *Eur. Phys. J.*, C77(10):663, 2017.
- [24] K.J. Eskola, H. Paukkunen, and C.A. Salgado. Eps09 a new generation of nlo and lo nuclear parton distribution functions. *Journal of High Energy Physics*, 2009(04):065, 2009.
- [25] Summary of ATLAS Pythia 8 tunes. 2012.
- [26] Peter Skands, Stefano Carrazza, and Juan Rojo. Tuning PYTHIA 8.1: the Monash 2013 Tune. *Eur. Phys. J.*, C74(8):3024, 2014.
- [27] Peter Zeiler Skands. Tuning Monte Carlo Generators: The Perugia Tunes. *Phys. Rev.*, D82:074018, 2010.
- [28] C. N. Yang and R. L. Mills. Conservation of isotopic spin and isotopic gauge invariance. *Phys. Rev.*, 96:191–195, Oct 1954.
- [29] Georg Schneider, Andreas Mooser, Matthew Bohman, Natalie Schön, James Harrington, Takashi Higuchi, Hiroki Nagahama, Stefan Sellner,

Christian Smorra, Klaus Blaum, Yasuyuki Matsuda, Wolfgang Quint, Jochen Walz, and Stefan Ulmer. Double-trap measurement of the proton magnetic moment at 0.3 parts per billion precision. *Science*, 358(6366):1081–1084, 2017.

- [30] J. Beringer, J. F. Arguin, R. M. Barnett, K. Copic, O. Dahl, D. E. Groom, C. J. Lin, J. Lys, H. Murayama, C. G. Wohl, W. M. Yao, P. A. Zyla, C. Am- sler, M. Antonelli, D. M. Asner, H. Baer, H. R. Band, T. Basaglia, C. W. Bauer, J. J. Beatty, V. I. Belousov, E. Bergren, G. Bernardi, W. Bertl, S. Bethke, H. Bichsel, O. Biebel, E. Blucher, S. Blusk, G. Brooijmans, O. Buchmueller, R. N. Cahn, M. Carena, A. Ceccucci, D. Chakraborty, M. C. Chen, R. S. Chivukula, G. Cowan, G. D’Ambrosio, T. Damour, D. de Florian, A. de Gouvêa, T. DeGrand, P. de Jong, G. Dissertori, B. Dobrescu, M. Doser, M. Drees, D. A. Edwards, S. Eidelman, J. Erler, V. V. Ezhela, W. Fetscher, B. D. Fields, B. Foster, T. K. Gaisser, L. Gar- ren, H. J. Gerber, G. Gerbier, T. Gherghetta, S. Golwala, M. Goodman, C. Grab, A. V. Gritsan, J. F. Grivaz, M. Grünewald, A. Gurtu, T. Gutsche, H. E. Haber, K. Hagiwara, C. Hagmann, C. Hanhart, S. Hashimoto, K. G. Hayes, M. Heffner, B. Heltsley, J. J. Hernández-Rey, K. Hikasa, A. Höcker, J. Holder, A. Holtkamp, J. Huston, J. D. Jackson, K. F. Johnson, T. Junk, D. Karlen, D. Kirkby, S. R. Klein, E. Klempt, R. V. Kowalewski, F. Krauss, M. Kreps, B. Krusche, Yu. V. Kuyanov, Y. Kwon, O. Lahav, J. Laiho, P. Langacker, A. Liddle, Z. Ligeti, T. M. Liss, L. Littenberg, K. S. Lu- govsky, S. B. Lugovsky, T. Mannel, A. V. Manohar, W. J. Marciano, A. D. Martin, A. Masoni, J. Matthews, D. Milstead, R. Miquel, K. Mönig, F. Moortgat, K. Nakamura, M. Narain, P. Nason, S. Navas, M. Neubert, P. Nevski, Y. Nir, K. A. Olive, L. Pape, J. Parsons, C. Patrignani, J. A. Peacock, S. T. Petcov, A. Piepke, A. Pomarol, G. Punzi, A. Quadt, S. Raby,

G. Raffelt, B. N. Ratcliff, P. Richardson, S. Roesler, S. Rolli, A. Roman-iouk, L. J. Rosenberg, J. L. Rosner, C. T. Sachrajda, Y. Sakai, G. P. Salam, S. Sarkar, F. Sauli, O. Schneider, K. Scholberg, D. Scott, W. G. Seligman, M. H. Shaevitz, S. R. Sharpe, M. Silari, T. Sjöstrand, P. Skands, J. G. Smith, G. F. Smoot, S. Spanier, H. Spieler, A. Stahl, T. Stanev, S. L. Stone, T. Sumiyoshi, M. J. Syphers, F. Takahashi, M. Tanabashi, J. Terning, M. Titov, N. P. Tkachenko, N. A. Törnqvist, D. Tovey, G. Valencia, K. van Bibber, G. Venanzoni, M. G. Vincter, P. Vogel, A. Vogt, W. Walkowiak, C. W. Walter, D. R. Ward, T. Watari, G. Weiglein, E. J. Weinberg, L. R. Wiencke, L. Wolfenstein, J. Womersley, C. L. Woody, R. L. Workman, A. Yamamoto, G. P. Zeller, O. V. Zenin, J. Zhang, R. Y. Zhu, G. Harper, V. S. Lugovsky, and P. Schaffner. Review of particle physics. *Phys. Rev. D*, 86:010001, Jul 2012.

- [31] R. W. McCallister and R. Hofstadter. Elastic Scattering of 188-MeV Electrons From the Proton and the  $\alpha$  Particle. *Phys. Rev.*, 102:851–856, 1956.
- [32] J. Engelen and P. Kooijman. Deep inelastic scattering at hermes: A review of experimental results in the light of quantum chromodynamics. *Progress in Particle and Nuclear Physics*, 41:1 – 47, 1998.
- [33] V. E. Barnes, P. L. Connolly, D. J. Crennell, B. B. Culwick, W. C. Delaney, W. B. Fowler, P. E. Hagerty, E. L. Hart, N. Horwitz, P. V. C. Hough, J. E. Jensen, J. K. Kopp, K. W. Lai, J. Leitner, J. L. Lloyd, G. W. London, T. W. Morris, Y. Oren, R. B. Palmer, A. G. Prodell, D. Radojčić, D. C. Rahm, C. R. Richardson, N. P. Samios, J. R. Sanford, R. P. Shutt, J. R. Smith, D. L. Stonehill, R. C. Strand, A. M. Thorndike, M. S. Webster, W. J. Willis, and S. S. Yamamoto. Observation of a hyperon with strangeness minus three. *Phys. Rev. Lett.*, 12:204–206, Feb 1964.

- [34] David J. Gross and Frank Wilczek. Ultraviolet behavior of non-abelian gauge theories. *Phys. Rev. Lett.*, 30:1343–1346, Jun 1973.
- [35] H. Strubbe. Development of the schoonship program. *Computer Physics Communications*, 18(1):1 – 5, 1979.
- [36] Francesco Knechtli. Lattice Quantum Chromodynamics. *PoS, CORFU2016:020*, 2017.
- [37] Roman Pasechnik and Michal umbera. Phenomenological Review on QuarkGluon Plasma: Concepts vs. Observations. *Universe*, 3(1):7, 2017.
- [38] N. Cabibbo and G. Parisi. Exponential Hadronic Spectrum and Quark Liberation. *Phys. Lett.*, 59B:67–69, 1975.
- [39] John C. Collins and M. J. Perry. Superdense Matter: Neutrons Or Asymptotically Free Quarks? *Phys. Rev. Lett.*, 34:1353, 1975.
- [40] H. R. Schmidt and J. Schukraft. The Physics of ultrarelativistic heavy ion collisions. *J. Phys.*, G19:1705–1796, 1993.
- [41] Albert M Sirunyan et al. Non-Gaussian elliptic-flow fluctuations in PbPb collisions at  $\sqrt{s_{NN}} = 5.02$  TeV. 2017.
- [42] Georges Aad et al. Measurement of the distributions of event-by-event flow harmonics in lead-lead collisions at  $\sqrt{s_{NN}} = 2.76$  TeV with the ATLAS detector at the LHC. *JHEP*, 11:183, 2013.
- [43] Serguei Chatrchyan et al. Study of high-pT charged particle suppression in PbPb compared to *pp* collisions at  $\sqrt{s_{NN}} = 2.76$  TeV. *Eur. Phys. J.*, C72:1945, 2012.

- [44] Vardan Khachatryan et al. Measurement of inclusive jet production and nuclear modifications in pPb collisions at  $\sqrt{s_{\text{NN}}} = 5.02$  TeV. *Eur. Phys. J.*, C76(7):372, 2016.
- [45] Guang-You Qin and Xin-Nian Wang. Jet quenching in high-energy heavy-ion collisions. *Int. J. Mod. Phys.*, E24(11):1530014, 2015. [,309(2016)].
- [46] E. V. Shuryak. The QCD phase diagram, equation of state, and heavy ion collisions. *Nucl. Phys.*, A702:83–95, 2002.
- [47] An introduction to pythia 8.2. *Computer Physics Communications*, 191(Supplement C):159 – 177, 2015.
- [48] Xin-Nian Wang and Miklos Gyulassy. HIJING: A Monte Carlo model for multiple jet production in p p, p A and A A collisions. *Phys. Rev.*, D44:3501–3516, 1991.
- [49] T. Pierog and K. Werner. EPOS Model and Ultra High Energy Cosmic Rays. *Nucl. Phys. Proc. Suppl.*, 196:102–105, 2009.
- [50] Zhi-Feng Liu. A new explanation to the cold nuclear matter effects in heavy ion collisions. 2014.
- [51] Betty Abelev et al. Centrality determination of Pb-Pb collisions at  $\sqrt{s_{\text{NN}}} = 2.76$  TeV with ALICE. *Phys. Rev.*, C88(4):044909, 2013.
- [52] Michael L. Miller, Klaus Reygers, Stephen J. Sanders, and Peter Steinberg. Glauber modeling in high energy nuclear collisions. *Ann. Rev. Nucl. Part. Sci.*, 57:205–243, 2007.
- [53] Rudolph Rogly, Giuliano Giacalone, and Jean-Yves Ollitrault. Geometric scaling in symmetric nucleus-nucleus collisions. In *27th International*

*Conference on Ultrarelativistic Nucleus-Nucleus Collisions (Quark Matter 2018) Venice, Italy, May 14-19, 2018, 2018.*

- [54] Roger D. Woods and David S. Saxon. Diffuse Surface Optical Model for Nucleon-Nuclei Scattering. *Phys. Rev.*, 95:577–578, 1954.
- [55] G. L. Bayatian et al. CMS Physics : Technical Design Report Volume 1: Detector Performance and Software. 2006.
- [56] G. L. Bayatian et al. CMS technical design report, volume II: Physics performance. *J. Phys.*, G34(6):995–1579, 2007.
- [57] Serguei Chatrchyan et al. Charged particle transverse momentum spectra in  $pp$  collisions at  $\sqrt{s} = 0.9$  and 7 TeV. *JHEP*, 08:086, 2011.
- [58] Torbjörn Sjöstrand, Stephen Mrenna, and Peter Skands. Pythia 6.4 physics and manual. *Journal of High Energy Physics*, 2006(05):026, 2006.
- [59] Torbjörn Sjöstrand, Stefan Ask, Jesper R. Christiansen, Richard Corke, Nishita Desai, Philip Ilten, Stephen Mrenna, Stefan Prestel, Christine O. Rasmussen, and Peter Z. Skands. An Introduction to PYTHIA 8.2. *Comput. Phys. Commun.*, 191:159–177, 2015.
- [60] R. Corke and T. Sjöstrand. Improved Parton Showers at Large Transverse Momenta. *Eur. Phys. J.*, C69:1–18, 2010.
- [61] Richard Corke and Torbjörn Sjöstrand. Multiparton Interactions with an  $x$ -dependent Proton Size. *JHEP*, 05:009, 2011.
- [62] Richard Corke and Torbjörn Sjöstrand. Interleaved Parton Showers and Tuning Prospects. *JHEP*, 03:032, 2011.

- [63] Hung-Liang Lai, Marco Guzzi, Joey Huston, Zhao Li, Pavel M. Nadolsky, Jon Pumplin, and C. P. Yuan. New parton distributions for collider physics. *Phys. Rev.*, D82:074024, 2010.
- [64] R. S. Thorne, A. D. Martin, W. J. Stirling, and G. Watt. Status of MRST/MSTW PDF sets. In *Proceedings, 17th International Workshop on Deep-Inelastic Scattering and Related Subjects (DIS 2009): Madrid, Spain, April 26-30, 2009*, page 22, 2009.
- [65] H. L. Lai, J. Huston, S. Kuhlmann, J. Morfin, Fredrick I. Olness, J. F. Owens, J. Pumplin, and W. K. Tung. Global QCD analysis of parton structure of the nucleon: CTEQ5 parton distributions. *Eur. Phys. J.*, C12:375–392, 2000.
- [66] M. Gluck, E. Reya, and A. Vogt. Dynamical parton distributions of the proton and small x physics. *Z. Phys.*, C67:433–448, 1995.
- [67] Fragmentation functions in  $e^+e^-$ , ep and pp collisions. <http://pdg.lbl.gov/2016/reviews/rpp2016-rev-frag-functions.pdf>.
- [68] Sidney D. Drell and Tung-Mow Yan. Massive lepton-pair production in hadron-hadron collisions at high energies. *Phys. Rev. Lett.*, 25:316–320, Aug 1970.
- [69] Sidney D. Drell and Tung-Mow Yan. Massive lepton-pair production in hadron-hadron collisions at high energies. *Phys. Rev. Lett.*, 25:902–902, Sep 1970.
- [70] The ratio of the nucleon structure functions  $f_2^n$  for iron and deuterium. *Physics Letters B*, 123(3):275 – 278, 1983.

- [71] Andy Buckley, James Ferrando, Stephen Lloyd, Karl Nordström, Ben Page, Martin Rfenacht, Marek Schnherr, and Graeme Watt. LHAPDF6: parton density access in the LHC precision era. *Eur. Phys. J.*, C75:132, 2015.
- [72] V. N. Gribov and L. N. Lipatov. Deep inelastic e p scattering in perturbation theory. *Sov. J. Nucl. Phys.*, 15:438–450, 1972. [*Yad. Fiz.*15,781(1972)].
- [73] Yuri L. Dokshitzer. Calculation of the Structure Functions for Deep Inelastic Scattering and e+ e- Annihilation by Perturbation Theory in Quantum Chromodynamics. *Sov. Phys. JETP*, 46:641–653, 1977. [*Zh. Eksp. Teor. Fiz.*73,1216(1977)].
- [74] Guido Altarelli and G. Parisi. Asymptotic Freedom in Parton Language. *Nucl. Phys.*, B126:298–318, 1977.
- [75] Xin-Nian Wang and Miklos Gyulassy. hijing. *Phys. Rev. D*, 44:3501–3516, Dec 1991.
- [76] Tie-Jiun Hou et al. Reconstruction of Monte Carlo replicas from Hessian parton distributions. *JHEP*, 03:099, 2017.
- [77] <http://www.claymath.org/sites/default/files/yangmills.pdf>.
- [78] Andy Buckley, Jonathan Butterworth, Leif Lonnblad, David Grellscheid, Hendrik Hoeth, James Monk, Holger Schulz, and Frank Siegert. Rivet user manual. *Comput. Phys. Commun.*, 184:2803–2819, 2013.
- [79] P. Abreu et al. Tuning and test of fragmentation models based on identified particles and precision event shape data. *Z. Phys.*, C73:11–60, 1996.